To the Graduate Council:

I am submitting herewith a dissertation written by Martin Krassimirov Djongolov entitled "Superdeformation and High Spin Spectroscopy Studies on ^{174}Hf." I have examined the final electronic copy of this dissertation for form and content and recommend that it be accepted in partial fulfillment of the requirements for the degree of Doctor of Philosophy, with a major in Physics.

Leo L. Riedinger

Major Professor

We have read this dissertation
and recommend its acceptance:

Lawrence W. Townsend

Carrol R. Bingham

Witold Nazarewicz

Accepted for the Council:

Anne Mayhew

Vice Chancellor
and Dean of Graduate Studies

(Original signatures are on file with official student records.)

Superdeformation and High-Spin Spectroscopy Studies on ^{174}Hf

A Dissertation
Presented for the
Doctor of Philosophy Degree
The University of Tennessee, Knoxville

Martin Krassimirov Djongolov
May 2006

Acknowledgments

No project can be considered accomplished without sharing it with the others. Sometimes people and events intersect in the right point, such that it can truly inspire someone's creativity. And it did, in the surrounding of the right ones.

Foremost, I would like to thank my academic adviser, Professor Lee Riedinger, for his determination and patience when guiding me through the subtleties of the field and for his support for my varying interests, both in science and art (his piano still sounds great, despite I tried to destroy it several times). He showed to me the real meaning of working hard but also to see the delight after it is done well. I also thank him for permitting me to explore freely, not only the nuclear spectroscopy field, but also other different scientific areas that contributed with their subject to my personal perception of the world. This greatly benefited my accomplishment as a scientist.

I also am obliged to Dr. Daryl Hartley, for all of the times of informal talks on physics as well as for showing me a unique perspective when dealing with everyday's cumbersome tasks. His moral support and comments in the final stages of preparation of this work are deeply appreciated. Daryl was always ready for discussion of my work as well as of any other question, ranging from the nucleus to philosophy. He made the well known distance between teacher and pupil look obsolete.

I thank Dr. Dimiter Balabanski for starting my acquaintance with Prof. Riedinger some years ago and for showing me that there is a science out there far more complex than I have imagined. A gratitude also goes to Dr. Miroslav Danchev, for all of the intriguing discussions on physics, world, history, and "high tech" issues. Many thanks to Irina Zartova, for raising her hand for me.

I thank the kind people at the International House at the University of Tennessee, Knoxville, for letting me play on their piano for 60 minutes, same pieces over and over, almost every day during the last three years.

I thank my colleagues of armor - the other graduate students who I shared the after hours with. Oscar, Perla, Juan Pablo, we had wonderful times together. Times to share the different perspectives from our lives, to argue in the subtle scholar manner, and to simply laugh. Yes, you were my closest support here. I thank Vladomus, who, despite being on the other globe's edge, sometimes was cheering for my advancing more enthusiastically than I did.

I hug my mother, father and sister. My parents never stood in my way deciding what I want to do when I "grow up". Rather, they always provided the healthy atmosphere for me to learn, ponder, and at the end, grow up. I am grateful to my mother who was always there to hear a new joke or a cry, no matter what. Mom, thank you also for introducing me

to music, the benefits of which I learned to appreciate much later, only here. Little sister, I wish you future accomplishments at least as big as I am boasting with now.

Finally, I wish I was able to thank my special someone. Despite the long wait and try, she still has not showed up. The long days and nights always seemed incomplete. A new project is underway and it is me to find Her.

Abstract

High-spin states of the nucleus ^{174}Hf were populated using the heavy-ion reactions at the Atlas accelerator facility at the Argonne National Laboratory and the 88" cyclotron facility at the Lawrence Berkeley National Laboratory. The de-exciting γ rays are detected with the GAMMASPHERE spectrometer. In this nucleus, eight superdeformed bands are observed for the first time. Studies on these bands as well as eight bands with normal deformation are performed. The hypothesis for presence of a triaxial shape at high deformation in ^{174}Hf is tested via lifetime measurements of the states of the superdeformed structures. The deduced quadrupole moments of four of the these bands are compared with the Ultimate Cranker calculations and an additional search for transitions that depopulate these structures is carried out. Discussion on the possibility that these bands manifest triaxiality in ^{174}Hf is presented. The study of the bands with normal deformation employed an extensive systematics of crossing frequencies, alignments, and Routhians. CSM and TRS calculations are performed and compared with these observables. Quasiparticle configurations for all of the bands with normal deformation are proposed, and $B(M1)/B(E2)$ and $B(E1)/B(E2)$ transition strength ratios are analyzed.

Contents

1 Introduction **1**

2 Theoretical Concepts **4**

2.1 General Considerations 4

2.2 The Liquid Drop Model 5

2.3 Nuclear Shapes 6

2.4 The Shell Model 8

2.5 The Cranked Shell Model 16

2.6 The $B(M1)/B(E2)$ ratio 24

2.7 Shell Corrections 26

2.8 Superdeformation 27

2.8.1 Wobbling 31

3 Experimental Techniques **36**

3.1 Populating High-Spin States 36

3.2 Reaction Selection 40

3.3 Detection of γ Rays 41

3.4 Gammasphere 42

3.5 Data Analysis 45

3.6 Analysis Programs and Databases 47

3.6.1 The Doppler Shift Attenuation Method 49

4 Superdeformation Studies **56**

4.1 Experimental Details and Results 56

4.2 Lifetime Measurements 65

4.3 Discussion 71

5 Study of Normal Deformed Bands **76**
5.1 The Level Scheme of ^{174}Hf 87
5.2 Discussion 97
5.2.1 The ground-state, β-, and octupole vibrational bands 97
5.2.2 The two-quasiparticle bands 105

6 Conclusions **124**

Bibliography **130**

Vita **139**

List of Tables

2.1 Convention for quasiparticle orbitals notation. The subscript denotes the ordering of the orbitals ascending with energy. 24

2.2 Calculated g_K factors for orbitals that are near the Fermi level in ^{174}Hf. Next to the Nilsson orbitals are given the corresponding quasiparticle orbital labels. 25

3.1 Characteristics of GAMMASPHERE. 44

4.1 Summary of DSAM analysis for SD bands in ^{174}Hf. 67

5.1 Relative intensities and energies of transitions in ^{174}Hf. 77

5.2 Calculated initial alignments and alignment gains at the first $\hbar\omega_c$ for orbitals near the Fermi surface for ^{174}Hf. The values are taken from CSM calculations at $\hbar\omega = 0.21\,\mathrm{MeV}$ for $\beta_2 = 0.287$, $\beta_4 = -0.017$, $\gamma = -0.2°$. Labels A,B,... uniquely denote both parity and signature of the orbitals, and the type of crossing. 102

5.3 $B(E1; I \rightarrow I-1)/B(E2; I \rightarrow I-2)$ values for levels in Band 3, level 7^- in Band 5, level 8^- in Band 6, and the octupole band in ^{172}Yb [Wal80]. Eqn. 2.56 was used to calculate the values for ^{172}Yb from data in [Wal80]. The units used for the ratio is $10^{-10}\,\mathrm{fm}^{-2}$. 103

5.4 Crossing frequencies and experimental and calculated alignment gains of low-K rotational bands in ^{174}Hf. The proposed changes in configuration are shown for each crossing. The label "ub" denotes a smooth alignment gain in the vicinity of the crossing, i.e., "upbend". The $\hbar\omega_{calc}$ and Δi_{calc} values are deduced from the CSM plot in Figs. 2.5 and 2.6. 106

5.5 Experimental alignments of the two-quasiparticle bands in ^{174}Hf at $\hbar\omega = 0.2\,\mathrm{MeV}$, compared with the sum of single-particle orbital values obtained from adjacent odd-A nuclei ^{173,175}Hf [Fab91, Cul04, Grp94] ,^{175}Ta [Wen96], and ^{173}Lu [Ven03, Fir96]. The signature splitting of the orbitals is also given. Harris parameters of $\mathcal{I}_0 = 36\,\hbar^2\,\mathrm{MeV}^{-1}$ and $\mathcal{I}_1 = 54\,\hbar^4\,\mathrm{MeV}^{-3}$ were used for all nuclei. Labels A, B,... uniquely denote both parity and signature of the orbitals. 108

List of Figures

2.1 Axially-symmetric nuclear shapes in the (β_2, γ) plane. For explanation see the text. 9

2.2 Nuclear chart denoting calculated stable quadrupole deformation [Mol95]. It can be noted that it is minimal in regions close to the magic numbers. The position of nucleus of interest, ^{174}Hf is shown. Note that it resides in a region with relatively high deformation. The difference between the deformation parameters ϵ_2 and β_2 is clarified in text. 11

2.3 Nilsson diagram for neutrons, $82 \leq N \leq 126$ ($\epsilon_4 = \epsilon_2^2/6$). The solid and dashed lines correspond, respectively, to positive and negative parity. Reproduced from [Fir96]. 13

2.4 Nilsson diagram for protons, $50 \leq Z \leq 82$ ($\epsilon_4 = \epsilon_2^2/6$). Reproduced from [Fir96]. 14

2.5 Quasiparticle Routhians for neutrons for ^{174}Hf. The deformation parameters $\beta_2 = 0.291$, $\beta_4 = -0.016$, $\gamma = -0.4^\circ$ are chosen, corresponding to a shape at a rotational frequency $\hbar\omega = 0.253\,\mathrm{MeV}$. The first neutron crossing is identified at 0.3 MeV. 22

2.6 Quasiparticle Routhians for protons for ^{174}Hf. The deformation parameters $\beta_2 = 0.291$, $\beta_4 = -0.016$, $\gamma = -0.4^\circ$ are chosen, corresponding to a shape at a rotational frequency $\hbar\omega = 0.253\,\mathrm{MeV}$. The first proton crossing is identified at $\sim 0.50\,\mathrm{MeV}$. 23

2.7 A sample Total Routhian Surface, calculated for ^{174}Hf for the ground state configuration (0 quasiparticles). Panel a) shows the energy surface at $\hbar\omega = 0\,\mathrm{MeV}$. The corresponding equilibrium deformation parameters are $\beta_2 = 0.273$, $\beta_4 = -0.022$, and $\gamma = 0.4^\circ$. Panel b) is calculated at $\hbar\omega = 0.455\,\mathrm{MeV}$, which yields deformation parameters $\beta_2 = 0.226$, $\beta_4 = -0.043$, and $\gamma = -4.5^\circ$. 28

2.8 The single particle levels calculated by using a simple harmonic oscillator potential for the case of axial symmetry. Note the change of shell gaps as a function of deformation. See [Nil95], p.116. 29
2.9 A γ-ray spectrum measured for the superdeformed band in ^{152}Dy and its spin assignments. Reproduced from [Twi86]. 30
2.10 The axial and triaxial shapes differ in the ways the total angular momentum I can be oriented in space. a) In an axial nucleus, $(a = b) \neq c$, an orientation along an axis perpendicular to the symmetry axis is favorable. b) In the case of a triaxial nucleus, $(a \neq b \neq c)$, all axes can have a different projection of the total angular momentum. 32
2.11 Scheme of the coupling of the angular momenta j of the particle and the core R in the case of a) Cranking regime and b) the wobbling mode. The total angular momentum is $I = R + j$. The subscripts denote the favored and unfavored states. Reproduced from [Ode01]. 34

3.1 An illustration of the fusion-evaporation process and its time scale. Taken from [Lai00]. 38
3.2 The de-excitation path of the nucleus in fusion-evaporation reaction. Reproduced from [Lai00]. 39
3.3 The energy dependence of the relative strength of the processes that occur in Ge crystal. 42
3.4 A typical construction of a Compton-suppressed detector array. The BGO shield is shown as well as the crystal of the Ge detectors. The veto signal in the case of an escaped γ ray provides a significant improvement of the peak-to-total ratio. 43
3.5 View of the GAMMASPHERE with the hemispheres open. In its center, additional auxiliary devices can be used. 44
3.6 The Doppler shift effect for a single γ-ray transition as a function of its lifetime and velocity of the recoil that is being slowed down in a medium (stopper). In case of long lifetime τ, there is only a stopped component present in the peak. For shorter lifetimes, the fraction of the γ rays that are emitted in flight becomes dominant. Reproduced from [Lai00]. 51

4.1 SD bands 1-4 in ^{174}Hf. The spectra were generated with all possible in-band triple-gate combinations within the hypercube. Transitions in the ground-state band are denoted by filled circles. The peaks marked with star symbol in panel d) denote $\Delta I = 1$ transitions in a rotational band built on the $K^{\pi} = 14^{+}$ isomer. Panel d) was chosen as one showing the peaks in the most visible way, though they are present in all SD band spectra for ^{174}Hf. 58

4.2 SD bands 5-8 in ^{174}Hf and the newly discovered SD band in ^{173}Hf [Har05]. The spectra were generated with all possible in-band triple-gate combinations within the hypercube. To the right of the dashed line the scale has been reduced by a factor of two. 59

4.3 Partial level scheme of ^{174}Hf showing the band structures that lie above the $K = 14^{+}$ isomer and the ground-state band. The $\Delta I = 1$ transitions in the rotational band built on the 14^{+} level as well as transitions from the ground-state band are identified in the spectra of all of the SD bands. The level scheme for the structures above the isomer is reproduced from [Har05a]. 60

4.4 The newly discovered superdeformed bands in ^{174}Hf from the GSFMA90 and GSFMA117 experiments. The excitation energy scale is normalized to zero, as no linking transitions to normal deformed structures were found. The top of the bands can be used as a convenient reference for their relative excitation. Assignments of spins and parities of the bands are tentative. The spin range estimation for the bands is based on recent work on similar structures in ^{175}Hf [Cul04]. 61

4.5 The second moment of inertia of the ground-state band and rotational band SD 1 in ^{174}Hf. At low rotational frequency, a typical value is around $50\,\hbar^2$/MeV for a normal deformed band, while the band SD1 starts with values about $100\,\hbar^2$/MeV. All other SD bands have similar values of their moments of inertia (see also Fig. 4.6). 63

4.6 The dynamic moments of inertia for the eight SD bands in ^{174}Hf and one in ^{173}Hf. The bands in ^{174}Hf were split into possible "families" based on their similarity of the moments of inertia. 64

4.7 Illustration of the iterative gating procedure. Both spectra are taken at a fixed angle of the GAMMASHPERE, different from 90°. Spectrum a) has been produced by using the unshifted energies 820 keV and 867 keV from SD1 in ^{174}Hf. The energies are background only, as they do not return discrete lines. Spectrum b) shows the best enhancement of the transitions in the band when the gating energies are allowed to vary with angle. The open circles denote transitions from the ground-state band. The filled circles denote transitions that belong to SD1. 66
4.8 The fully summed spectrum of SD1 in ^{174}Hf. The displayed spectra are at a) 50° and b) 130°. The peaks are marked with their unshifted energies. . . 68
4.9 $F(\tau)$ curves for the most intense SD bands in ^{174}Hf. The uncertainties of the quadrupole moments are taken at $\chi^2_{min} + 1$. 69
4.10 Potential energy surface for ^{174}Hf for the lowest (π, α) = (+,0) configuration at spin $I = 50\,\hbar$. The spacing between contours is 200 keV. 72

5.1 Partial level scheme of ^{174}Hf. Bands 1, 2, and 3 denote the ground-state band, the β-vibrational band, and a rotational band based on octupole vibration [Wal83], respectively. 88
5.2 Spectra of Bands 1 and 2 and 3 obtained from GSFMA117 experiment. Spectrum a) (Band 1) is obtained by summing of triple gates, using 810 keV in all of them as a clean reference. Spectrum b) (Band 2) is obtained by single triple gating on 806 keV, 677 keV, and 862 keV. Spectrum c) (Band 3) is obtained by single double gating on 739 keV and 949 keV, using triple gating to obtain the highest spin states. Spectrum d) (Band 3) is obtained by summing triple gates within the band above 515 keV. 89
5.3 Plot of the energy of the levels as a function of spin for Band 1, Band 2, and the (-,1) partner of Band 3, subtracted by the rigid rotor value for ^{174}Hf. Band 2 becomes yrast at spin $24\,\hbar$ while Band 3 becomes lowest in energy at spin $35\,\hbar$. The constant that corresponds to a spherical rigid rotor with mass 174, $A_0 = 0.00617$ MeV, was used. 90
5.4 Plot of the energy of the levels as a function of spin for the zero signatures of all rotational bands. Same constant $A_0 = 0.00617$ MeV was used. 91
5.5 Band 4, Band 5, and Band 8 in ^{174}Hf. Shown is only a partial level scheme of the ground-state band, up to the highest level that is populated by these three bands. 92

5.6 Spectra of Band 4 and Band 5 in ^{174}Hf obtained from the GSFMA117 experiment. Spectrum a) (Band 4) is produced by single triple gating on 508 keV, 563 keV and 632 keV. Spectrum b) is produced by triple gating on 538 keV, 638 keV and 685 keV. Spectrum c) (Band 5) is produced by gating on 513 keV and 593 keV, and the spectrum in panel d) is obtained by gating on 528 keV and 592 keV. 93
5.7 Band 6 and Band 7 in ^{174}Hf. 95
5.8 GSFMA117 data showing spectra of Band 6 and Band 7 in ^{174}Hf. The spectra a) and b) are produced by adding many gates throughout Band 6. Both signature partners are visible. Spectra c) and d) show Band 7. 96
5.9 Alignments for the low lying two-quasiparticle bands in ^{174}Hf. The used Harris parameters are $\Im_0 = 31.4\ \hbar^2\,\mathrm{MeV}^{-1}$ and $\Im_1 = 52.5\ \hbar^4\,\mathrm{MeV}^{-3}$ for all bands to represent the two-quasiparticle core after the AB crossing in Band 1. The open squares denote the band partners that have signature $\alpha = 0$. The filled squares correspond to $\alpha = 1$. 98
5.10 Routhians for the low lying two-quasiparticle bands in ^{174}Hf. The same Harris parameters $\Im_0 = 31.4\ \hbar^2\,\mathrm{MeV}^{-1}$ and $\Im_1 = 52.5\ \hbar^4\,\mathrm{MeV}^{-3}$ are used. The open squares denote the band partners that has signature $\alpha = 0$. The filled squares correspond to $\alpha = 1$. 99
5.11 Alignment plot of ground-state bands in ^{170}Hf [Lis81], ^{172}Hf [Cul98], ^{174}Hf, and the β band in ^{174}Hf. The same Harris parameters of $\Im_0 = 31.4\hbar^2\,\mathrm{MeV}^{-1}$ and $\Im_1 = 52.5\ \hbar^4\,\mathrm{MeV}^{-3}$ were used. A reduction of the interaction strength of the first proton crossing with increase of neutron number is visible at $\hbar\omega \sim 0.5\,\mathrm{MeV}$. 100
5.12 Alignment plot of (π,α)=(-,1) Band 3 in ^{174}Hf compared with alignments of the favored ($\alpha = +1/2$) signature of the $\nu 7/2[633]$ band in ^{171,173,175}Hf ([Cul00, Fab91, Cul04]). Harris parameters of $\Im_0 = 31.4\ \hbar^2\,\mathrm{MeV}^{-1}$ and $\Im_1 = 52.5\ \hbar^4\,\mathrm{MeV}^{-3}$ were used. 104
5.13 Alignment plot of both signature partners of Band 4 compared to alignment of both signatures of the $\nu 5/2[512]$ band in ^{175}Hf [Grp94]. 107
5.14 Alignment plot of both signatures of Band 5 in ^{174}Hf compared to alignment of $\nu 7/2[633]$ bands in ^{171,173,175}Hf ([Cul00, Fab91, Cul04]). 110
5.15 Alignment plot of both signatures of Band 7 and Band 5 in ^{174}Hf. The usual Harris parameters were used. 111

5.16 Alignment plot of the favorite signature of Band 6 compared to alignment of $\pi 1/2[541]$ in ^{173}Lu [Ven03], ^{175}Ta [Wen96], ^{169}Lu [Oga93], ^{171}Lu [Bar98], and ^{167}Lu [HYu90]. 114
5.17 $B(M1)/B(E2)$ ratios deduced from the observed branching ratios for the two-quasiparticle bands along with the theoretical estimation based on the rotational model. Error bars are also from error propagation in the used formula. 115
5.18 The $|g_K - g_R|$ value for the two-quasiparticle bands in ^{174}Hf along with theoretical calculations. The fits are based on the same configurations as in Fig. 5.17. The main contribution to the width of the error bars is the error propagation within the used formulas, starting from the initial uncertainties in the energies. 116
5.19 Illustration of the effect of the residual interaction on the crossing frequency. 118
5.20 TRS calculations for ^{174}Hf for a) af and b) bf configurations at $\hbar\omega = 0.347$ MeV. The corresponding deformation parameters are $\beta_2 = 0.298$, $\beta_4 = -0.018$, $\gamma = 1.3°$ for af, and $\beta_2 = 0.257$, $\beta_4 = -0.030$, $\gamma = 1.3°$, for bf, respectively. 120
5.21 CSM calculations for the af configuration, using the deformation parameters $\beta_2 = 0.298$, $\beta_4 = -0.018$, $\gamma = 1.3°$. 121
5.22 CSM calculation using adjusted deformation parameters $\beta_2 = 0.35$, $\beta_4 = 0.03$, $\gamma = 0°$. 122
5.23 Partial summed spectra of the $\alpha = 0$ signature partner in Band 6, obtained from the BLUE database by gating on all transitions between 555 keV and 809 keV. Panel a) denotes summed spectrum at backward angles 121.7° and 129.9°. Panel b) presents summed spectra at 79.9°, 90°, and 100.0°. Panel c) shows summed spectra at forward angles 50.1° and 58.3°. The lineshape change due to the Doppler broadening is clearly visible above the 628-keV transition. 123

Chapter 1

Introduction

From a physics point of view, all phenomena in nature can be explained in principle within the framework of only three fundamental interactions among its established constituents, leptons and quarks. These interactions are the gravitational, the electroweak, and the strong force. Each possesses its own characteristics in terms of symmetries and coupling strengths, governing different spatial and time scales, and contributing to the enormous number of phenomena observed today with modern scientific tools.

While generally well understood from a qualitative point of view, the quantitative side of the fundamental interactions is always put to the test by the advance of physics. The constant search for weaker and more subtle effects marks the natural frontier of its progress and provides a better understanding of the fine behavior of the interactions under extreme conditions such as high energy and particle density or high particle number. As an illustrative example of the latter, one can point to the study of solid state physics - a macroscopic conglomerate of electrons and atomic nuclei bound by the electromagnetic interaction. Although this interaction is the best studied of the three, the presence of a vast number of degrees of freedom changes the properties of the interaction completely. This requires a fairly different treatment than the pure electromagnetic interaction. The same situation is observed in all domains of fundamental interactions, showing that the physical nature of the interaction itself has not yet reached the limit of its potential for producing new phenomena.

Nuclear physics introduces a unique playground for the study of the strong interaction. The atomic nucleus as a quantum system summons a large number of shapes and motion modes, each emerging from collective and/or individual interactions among the nucleons. Such interactions make the nucleus a source of rich experimental information. Today multi-detector γ-ray arrays combined with coincidence and tagging methods have proven to be

wonderful experimental tools in extracting such data. Information obtained from α, β, and more exotic particle decay modes (like multi-proton emission) reveal not only the bulk properties of the nucleus (like its mass and shape) but also the subtle internal structure of nucleons in the nuclear potential.

Along with the experimental studies, the theoretical treatment of the nucleus has reached a high level as well. The rapidly developing computational hardware has allowed nuclear models to become highly sophisticated in describing details of the interaction. With a size of $\sim 10^{-15}$ m, the nucleus defines a spatial scale that has intermediate size compared to the scales where the strong interaction can be treated perturbatively within quantum chromodynamics. That non-perturbative component of the strong interaction, the nuclear interaction, exhibits a high complexity and can be deemed as a separate interaction, distinctive by its characteristics. This reflects on the specifics of the nuclear models and makes their development challenging.

This dissertation consists of two major studies, presenting the data from three experiments carried out at the GAMMASPHERE detector array. The first part is dedicated to studies of superdeformation, built on rotational bands we found in ^{174}Hf, thus extending the known region of superdeformation. An intriguing possibility of this new region of superdeformation is that it could be based on triaxial core shapes, based on predictions by the Ultimate Cranker (UC) calculations. Following this line, quadrupole moments of four of the eight superdeformed bands have been determined and compared to those in neighboring Lu nuclei, where triaxial superdeformed bands have been reported. The Doppler Shift Attenuation Method (DSAM) was used extensively during the analysis stage of the work. A novel nuclear database called BLUE is described along with a recently developed background subtraction method, which facilitated a quick processing of the data. The final result could not prove the existence of triaxial shapes in ^{174}Hf, but yet revealed that the internal configurations on which the superdeformed bands are built are very different in nature from the neighboring Lu isotopes. This raises the question of whether the triaxiality exists in a broad mass region. However, many intriguing questions remain concerning the bands which may fuel future studies.

The second part examines the properties of high-spin states in ^{174}Hf originating from fast nuclear rotation and normal deformation. New rotational bands are assigned and the known bands have been extended to higher spin, shedding light on the basic evolution of the nucleon orbitals under the influence of significant Coriolis forces. The changes of the moments of inertia and quasiparticle alignments at high spin reveal more clearly the processes involved in this nucleus as it approaches the rigid rotor limit. The complete level scheme of the low lying two-quasiparticle bands is presented. It is clear that ^{174}Hf is an

exceptional source for the study of various shapes and dynamic modes.

For nuclear systems, spin notation is in units of $\hbar$ and energy is in appropriate derivatives of electron-volts. For technical convenience, all formulas that involve experimental observables are expressed in units that emphasize the quantity of interest and minimize the influence of less important numerical constants (e.g. moments of inertia have dimensions of $\hbar^2/\mathrm{keV}$ or $\hbar^2/\mathrm{MeV}$ instead of $\mathrm{kg\,m^2}$).

Chapter 2

Theoretical Concepts

Nuclear theory plays an important role in interpreting experimental observations as well as providing directions for future observations. Simple as they are, it is astonishing that the first nuclear models developed were able to describe a vast majority of observed nuclear properties. Today the presence of sophisticated microscopic treatments and *ab initio* calculations only shows the maturity of the field. However, a unified model of the nuclear interaction that covers the entire nuclear chart is still lacking. Each model is applicable only to a certain mass region, using appropriate approximations. The main challenge is the fact that the nucleus is a highly correlated quantum system. A theoretical description aiming to cover all such correlations still remains as a task for the future.

In this chapter some basic theoretical ideas will be considered and the Cranked Shell Model will be emphasized as it is particularly suitable for high-spin studies.

2.1 General Considerations

In the nucleus there are two distinguishable motion modes - the individual and the collective motion of the nucleons. However, it has to be pointed out that such a division is highly idealized. Collective motion is a coherent state with correlated contributions from the individual nucleons. A state that is based on single-particle motion is realized when an unpaired ("valence") nucleon is decoupled from the core of paired nucleons whose coherent motion cannot be easily disturbed. In the ideal case a realistic description of the interaction among the nucleons is realized by taking into account all A-body interactions. At present, due to immense mathematical difficulties, only the two-body interactions (and recently three-body) are used. Even in this case, an exhaustive inclusion of those forces is done only for very light nuclei.

Heavier systems are best described by effective interactions that emerge from an "aver-

aged" potential. Although this method (Hartree-Fock or HF) includes correlations between the nucleons via averaging, it has the disadvantage that there are some correlations that the mean field neglects, but which are still important for explaining observations. However, such an approach is convenient, as it introduces the nucleons as free particles moving in a mean field, which makes it easy to handle the total wave function. In addition, it can be used as a base description, on top of which other frameworks can be incorporated. Such extended models in principle give a more adequate description of the microscopic correlations. A central strategy beyond the mean field is the concept of quasiparticles. The main advantage is that the model space naturally contains both occupied and empty single particle states, reflecting the quantum-mechanical nature of the nucleonic system. Yet the quasiparticles are treated as independent and moving in an average potential. In the limit of high angular momentum, the nucleus is best described in the terms of the Cranked Shell Model (CSM). Its main idea is that the nuclear potential is defined in coordinates connected with the nucleus (internal coordinates), which is rotating with a constant angular velocity ω. In this semi-classical regime, the Coriolis force is comparable to the pairing strength, which affects the individual motion of the nucleons, and thus rearranges the internal structure of the nucleus. In this work the Cranked Shell Model is employed as a tool of choice for interpretation of the experimental data. In the following chapters models and ideas that form the core of CSM will be discussed.

2.2 The Liquid Drop Model

The Liquid Drop Model (LDM) is one of the first models developed for describing the bulk properties of the nucleus such as its mass and fission ability. The physics phenomena incorporated in this model are universal for all nuclei, which made LDM the basis for the majority of collective nuclear models. The experimental facts that led to its development are (1) the saturation property of the nuclear force, and (2) that nuclear matter is incompressible and the presence of a well-defined surface. The latter facts allow the nucleus to be presented classically as a drop of continuous media.

The nuclear density is found to follow the approximate relation [Wds54]

$$\rho(r) = \rho_0 \left[1 + e^{\frac{r-R}{a}}\right]^{-1}, \tag{2.1}$$

with $\rho_0 \sim 0.17$ nucleons fm^{-3}. The incompressibility explains well the experimentally observed dependence of the radius parameter as a function of the mass number

$$R(A) = r_0 A^{1/3}, \tag{2.2}$$

where r_0 has value of 1.1×10^{-15} m. Often the root-mean-square value is used, derived from Eqn. 2.1, which slightly modifies the value of r_0 to 1.2 fm.

The analogy with ordinary liquids is close; however, the fact that the nucleons obey Fermi statistics leads to some differences. For a nucleus in its ground state, all the single-particle orbitals are occupied, which forbids scattering of the nucleons that are below the Fermi surface. This effectively introduces a large average distance between nucleons, which is estimated to be about 2 fm. This is commensurate with the diameter of the nucleus, which is typically around 6.6 fm (for mass 150). Considering the high number of nucleons in this example, it becomes clear that the scattering of nucleons is highly suppressed. This is contrary to an ordinary liquid, where scattering of the molecules from each other is a predominant effect.

In the LDM approximation it is possible to give a quantitative explanation of important characteristics of the nucleus, e.g., its binding energy. Bethe and Weizsäker give the expression [Bet36]

$$B(Z,N) = a_V A + a_S A^{2/3} + a_C \frac{Z^2}{A^{1/3}} + a_I \frac{(N-Z)^2}{A} - \delta(A) \tag{2.3}$$

with the parameters $a_V = 15.68$, $a_S = 1856$, $a_C = 0.717$, $a_I = 28.1$ MeV. They correspond to particular strengths of the different effects that the formula includes. The first term relates to *volume* - it accounts for the binding energy inside the nucleus to which all the nucleons contribute. The second term is proportional to R^2, accounting for the presence of a *surface*. The third term is the Coulomb repulsive interaction among the nucleons. The fourth term is the so-called *symmetry* term, describing the energy difference between protons and neutrons. Indeed, if a neutron decays to a proton, this would change the binding energy because the proton has to occupy levels above the Fermi level. The last term governs the *pairing* energy. It has values of $\pm 34 \times A^{-3/4}$ for even-even and odd-odd nuclei, respectively, and it is zero for odd-even nuclei. We see that although LDM is a first approximation to the properties of the nucleus, it includes quantities that have microscopic origin (like pairing). Indeed, although Eqn. 2.3 describes well the binding energy on average, there are experimental oscillations observed, caused by shell effects as well as clustering of groups of nucleons inside the nucleus (for light nuclei). Other applications of the liquid drop model include description of fusion and fission reactions as well as vibrations.

2.3 Nuclear Shapes

A common feature of the spectrum of nuclear excitations is the presence of rotational bands. For a given spin interval the energy of the levels of the band follows closely the formula for

the energy of a quantum rigid rotor,

$$E_{rot}(I) = \frac{\hbar^2}{2\mathcal{J}} I(I+1) + E_0, \tag{2.4}$$

where E_0 is some reference energy. The expression suggests that the nuclear mass density has a distribution that is not rotationally invariant. Observed from a reference frame connected with the nucleus, the average density would exhibit an anisotropy. Such an anisotropy can be conveniently described with the assignment of a particular geometrical shape of the nuclear density distribution. It has been proven that this concept is very useful in interpretation of experimental data. Many collective modes, both rotational and vibrational, can be interpreted as specific types of motion of the nuclear shape.

The nuclear shape can be parametrized via the magnitude of a radius-vector $R(\theta, \phi) = |\vec{R}|$ pointing out to the surface. In spherical coordinates,

$$R(\theta, \phi) = NR_0 \left[1 + \sum_{\lambda=0}^{\infty} \sum_{\mu=-\lambda}^{\lambda} \alpha_{\lambda\mu} Y_{\lambda\mu}(\theta, \phi) \right], \tag{2.5}$$

where N is a normalization factor that guarantees the incompressibility of the nuclear matter. That is,

$$\int d\Omega \int^{R(\theta,\phi)} r^2 dr = \frac{4\pi}{3} R_0^3,$$

where $R_0 = r_0 A^{1/3}$. The latter relation will depend on the expansion coefficients $\alpha_{\lambda\mu}$. Due to the requirement that R is a real number, we have the condition that

$$\alpha^*_{\lambda\mu} = (-1)^{\mu} \alpha_{\lambda-\mu}.$$

The coefficients $\alpha_{\mu\nu}$ are the deformation parameters, which in particular cases have special notation (see below). In the expansion given by Eqn. 2.5, the multipoles λ are limited from above, with $\lambda < A^{1/3}$, since the possible maxima in the surface are proportional to λ^3.

The deformation parameters are transformed as spherical tensors of rank λ under the group SO(3) for spatial rotations,

$$\alpha_{\lambda\mu} = \sum_{\mu'} D^{\lambda}_{\mu\mu'}(\Omega) \alpha_{\lambda\mu'}, \tag{2.6}$$

here $D^{\lambda}_{\mu\mu'}$ are the Wigner functions [Rin00] and Ω are the Euler angles. The choice of the deformation parameters depends on the properties of interest in the nucleus that needs to be described. A special reference frame can be used in order to reduce the number of parameters. The latter can also be justified with physics considerations. The monopole and

the dipole terms (α_{00} and $\alpha_{1\mu}$) are usually neglected due to the high energy excitation of a breathing mode and the translation of the nucleus as a whole, respectively. The quadrupole terms $\alpha_{2\mu}$ can be reduced by placing the reference frame to coincide with the principal axes of the distribution of the nuclear matter. In this case, the only non-zero parameters become α'_{20} and α'_{22}. They can be written in terms of Hill-Wheeler coordinates β, γ [Hil53],

$$\alpha'_{20} = \beta_2 cos(\gamma), \alpha'_{22} = -\frac{1}{\sqrt{2}}\beta_2 sin(\gamma). \tag{2.7}$$

Those two parameters allow the description of any quadrupole shape. In the case when axial symmetry is present, Eqn. 2.5 has the simpler form:

$$R(\theta, \phi) = N(\beta)R_0 \left[1 + \sum_{\lambda=2}^{\lambda_{max}} \beta_\lambda Y_{\lambda 0}(\theta, \phi)\right] \tag{2.8}$$

where $\beta_\lambda = \alpha_{\lambda 0}$. When $\beta_2 > 0$, we say that the nucleus has a prolate shape, which closely resembles the shape of a sphere that is stretched along its polar axis. If $\beta_2 < 0$, the nucleus has an oblate shape, i.e., the sphere is contracted along the polar axis. The axial symmetry is present only when γ is a multiple of $\pi/3$. In the rest of the cases we say that the nucleus has a triaxial shape. Often it is necessary for one to specify not only the shape but also the axis in the intrinsic reference frame around which the nucleus is rotating. The Lund convention is often used, which is shown in Fig. 2.1. These notations are used further in this work. Both at $\gamma = 0^\circ$ and $\gamma = -120^\circ$ the nucleus has a prolate shape and rotates respectively around an axis that is perpendicular and collinear to its symmetry axis. The former case corresponds to a collective rotation, while in the latter case the spin is generated by single-particle excitations only. Oblate shapes are realized at $\gamma = \pm 60^\circ$. Again, due to the rotational invariance in the case of $\gamma = 60^\circ$ for oblate shape, the spin is generated by single-particle excitations. At $\gamma = -60^\circ$, the oblate shape rotates around an axis that is perpendicular to its symmetry axis. The region between $\gamma = 0^\circ$ and $\gamma = -60^\circ$ corresponds to a triaxial shape of the nucleus, that is, there is no infinitesimal rotational symmetry around any of its principal axes. In this case a new rotational mode can emerge, the so-called wobbling mode, which can be illustrated as a precession of the vector of the total angular momentum around a principal axis. Later in this work we will address this mode in detail in connection with the superdeformation studies.

2.4 The Shell Model

The idea that the nucleons arrange in shells inside the nucleus has been introduced in analogy with the shell structure of the electron cloud in the atom. In the atom, the sin-

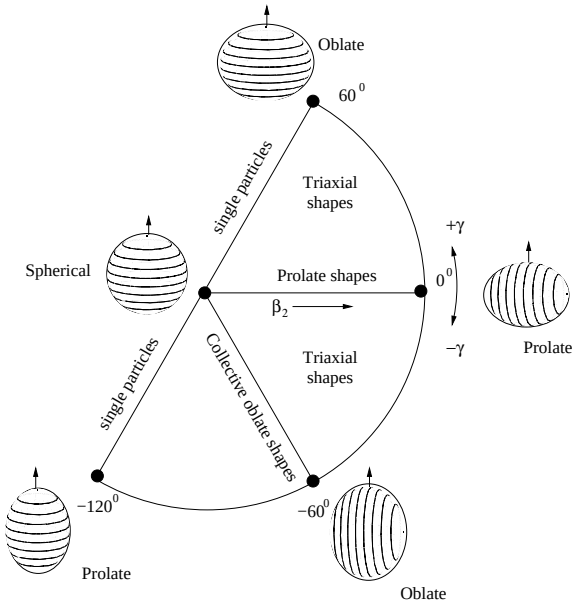


Figure 2.1: Axially-symmetric nuclear shapes in the (β_2, γ) plane. For explanation see the text.

gle electron ionization energy increases sharply when the number of electrons is equal to particular numbers (2, 12, 20,...). Similarly, it has been found that the nucleon separation energies S_p, S_n exhibit sharp peaks when the number of neutrons and/or protons is equal to 8, 20, 28, 50, 82, and 126 (for neutrons). Those numbers are referred to as "magic numbers". Such a close analogy has raised the hypothesis that nuclear structure is similar to that in the atom. Correspondingly, a model that reflects such structure would be suitable for reproducing the nuclear shell properties. However, a direct application of the atomic shell model to the nuclear system is not possible. The main reason is that in the nucleus there is no external central potential. Due to the nature of the strong interaction, each nucleon contributes significantly to the nuclear potential, thus no preferred source point can exist. However, other effects can allow a description of the nucleons as free particles. As fermions, nucleons cannot occupy the same single particle states. This poses a limit on their scattering and thus increases their average distance.

The spherical shell model was the first one to reproduce the magic numbers and the magnetic moments of the nuclei near the magic numbers correctly ("closed shells") [May49, Hax49]. The major step was realizing the importance the spin-orbit coupling. Introducing an $\mathbf{l}.\mathbf{s}$ term in the Hamiltonian effectively reduced the otherwise $2(2l+1)$ degenerate levels. It also allowed orbits with high j to be brought lower in energy, which creates the

experimentally observed energy gaps.

The success of the model was closely related to the fact that the early studies were limited to light nuclei that are likely to be near closed shells (2, 8, 20). However, as more nucleons are added outside a closed shell, their interaction with the rest of the nucleons that complete the shell (called the "core") increases to such extent that it alters the underlying shell structure. For nuclei that are far from the magic numbers, the predictions of the shell model show discrepancies. The measured quadrupole moments of the ground states show a significant deviation from spherical symmetry. It became clear that a more suitable description of an equilibrium shape of a nucleus would be one that is not spherical. Nuclei in regions such as $150 < A < 190$ and $A > 220$ show rotational bands that follow closely the dependence $E \propto I(I+1)$. This leads to the assumption of existence of a stably deformed shape and thus a deformed mean field as a residual component of the nuclear interaction should be considered.

A sample map of a calculated ground state quadrupole deformation is shown on Fig. 2.2. Regions close to the magic numbers, both for neutrons and protons, clearly show a lack of deformation, while farther away there are regions of larger deformation. The approaches for obtaining a deformed mean field are in two major classes:

• Microscopic - The interaction between single nucleons is considered and via fundamental principles (like variation) a part of the interaction is separated to serve as a mean potential.

• Empirical - Phenomenological potentials are chosen that are deemed to follow closely the real potential; their parameters are adjusted in order to reproduce the experimental observations.

The commonly chosen empirical potentials for description of deformed nuclei are Nilsson [Nil69] and Woods-Saxon [Wds54].

The Nilsson potential is split in two parts, one of them is an axial anisotropic harmonic oscillator (apart from the trivial translation term)

$$\frac{\mathbf{p}^2}{2m} + H_{osc} = \frac{\mathbf{p}^2}{2m} + \frac{1}{2}m\left[\omega_\perp(x^2+y^2) + \omega_z z^2\right] \tag{2.9}$$

and another part that includes the spin-orbit coupling and a correction term that accounts for the nucleons close to the surface of the nucleus that experiences a deeper potential well:

$$H' = -2\kappa\hbar\omega_0 \mathbf{l}.\mathbf{s} - \mu\hbar\omega_0\left(\mathbf{l}^2 - \langle\mathbf{l}^2\rangle_N\right), \tag{2.10}$$

where κ and μ are parameters and ω_0 is determined from the requirement of a constant volume of the nucleus:

$$\omega_\perp^2\omega_z = \omega_0^3 = const.$$

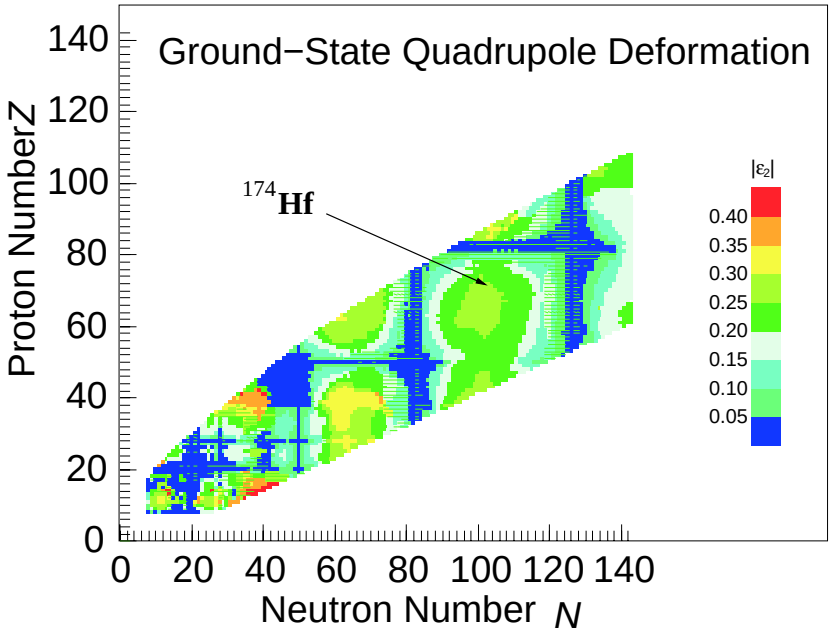


Figure 2.2: Nuclear chart denoting calculated stable quadrupole deformation [Mol95]. It can be noted that it is minimal in regions close to the magic numbers. The position of nucleus of interest, ^{174}Hf is shown. Note that it resides in a region with relatively high deformation. The difference between the deformation parameters ϵ_2 and β_2 is clarified in text.

The Nilsson Hamiltonian can be conveniently written using the so-called "stretched coordinates"

$$\xi = x\left(\frac{m\omega_\perp}{\hbar}\right)^{1/2}, \eta = y\left(\frac{m\omega_\perp}{\hbar}\right)^{1/2}, \zeta = z\left(\frac{m\omega_z}{\hbar}\right)^{1/2}, \rho^2 = \xi^2 + \eta^2 + \zeta^2. \tag{2.11}$$

In principle, the Nilsson Hamiltonian can be written in such form that it resembles deformations of general type, when particularly higher order terms of the nuclear shape are considered (like octupole and hexadecapole deformation). In the case of nuclei with axial quadrupole deformation, one parameter is enough, which in the Nilsson model is called ϵ. The frequencies of the deformed oscillator potential are then written as

$$\omega_\perp^2 = \omega_0^2(\epsilon)\left(1 + \frac{1\epsilon}{3}\right), \omega_z^2 = \omega_0^2(\epsilon)\left(1 - \frac{2\epsilon}{3}\right). \tag{2.12}$$

The parameter ϵ is related to the geometrical deformation parameter β_2 as

$$\epsilon = \frac{3}{2}\sqrt{\frac{5}{4\pi}}\beta \approx 0.95\beta.$$

There is an additional deformation parameter, which is related to deviation from axial symmetry of a deformed nucleus. Such a deviation, denoted by γ, introduces an additional degree of freedom, which can be used as classification of shapes of triaxial form. It will be used in the theoretical discussion related to superdeformation, later in this work

Multipoles of higher order can be taken into account by adding terms to H_{osc} of the type $2\epsilon_\lambda P_\lambda(\cos\theta_t)$, $\cos\theta_t = \zeta/\rho$. Through the use of quadrupole and hexadecapole deformation parameters, the Nilsson Hamiltonian can be written as

$$H_{Nilss} = \frac{1}{2}\hbar\omega_0(\epsilon_2,\epsilon_4)\times$$
$$\times\left(-\Delta_{\epsilon\eta\zeta} + \frac{2}{3}\epsilon_2\frac{1}{2}\left(2\frac{\partial^2}{\partial\zeta^2} - \frac{\partial^2}{\partial\epsilon^2} - \frac{\partial^2}{\partial\eta^2}\right) + \rho^2 - \frac{2}{3}\epsilon_2\rho^2 P_2(\cos\theta_t) + 2\epsilon_4\rho^2 P_4(\cos\theta_t)\right)$$
$$- 2\kappa\hbar\omega_0\mathbf{l_t}.\mathbf{s} - \mu\hbar\omega_0\left(\mathbf{l_t}^2 - \langle\mathbf{l_t}^2\rangle_N\right). \quad (2.13)$$

The solution of the Schrödinger equation for H_{Nilss} can be obtained (most often numerically), where single-particle energy spectra are dependent on the deformation parameters. It can also be shown that the only good quantum numbers are the projection of the total angular momentum on the z axis, Ω, and the parity π. Indeed, only $j_z = l_z + s_z$ commutes with the Hamiltonian, which comes from the assumption of axial symmetry. The parity conservation emerges due to the symmetry with respect to the xy plane. For higher deformations, the projection of the orbital angular momentum $|\Lambda|$, the principal quantum number N, and n_z, a quantum number that comes from quantization along the z axis in cylindrical coordinates also become good quantum numbers. Those quantum numbers are called *asymptotic*.

It is accepted that the orbitals in the Nilsson diagrams be denoted with the asymptotic quantum numbers of the type $\Omega^\pi[Nn_z|\Lambda|]$, which satisfies certain mathematical relations among each other. We have $\Omega = \Lambda \pm 1/2$ and $n_z + \Lambda$ is of the same parity as N. A plot that represents that functional dependence of the single-particle energy on deformation ϵ_2 is called a Nilsson diagram. A simple example for protons and neutrons is shown in Fig 2.3 and Fig 2.4. It can be seen that at $\epsilon_2 = 0$ (that is, when the nucleus is spherical), the magic numbers are reproduced. In the diagrams, both positive and negative values of ϵ_2 are possible, which corresponds, to prolate and oblate axial shapes of the nucleus, respectively.

Since deformation in the Nilsson model partially removes the $2j+1$ degeneracy, each shell splits into doubly degenerate orbitals with $\Omega = j, j-1, j-2, ..., \frac{1}{2}$, giving a total number of $j + \frac{1}{2}$ orbitals.

An important question from an experimental point of view is the exact arrangement of these orbitals, when a particular deformation is assumed. For example, as one can see from

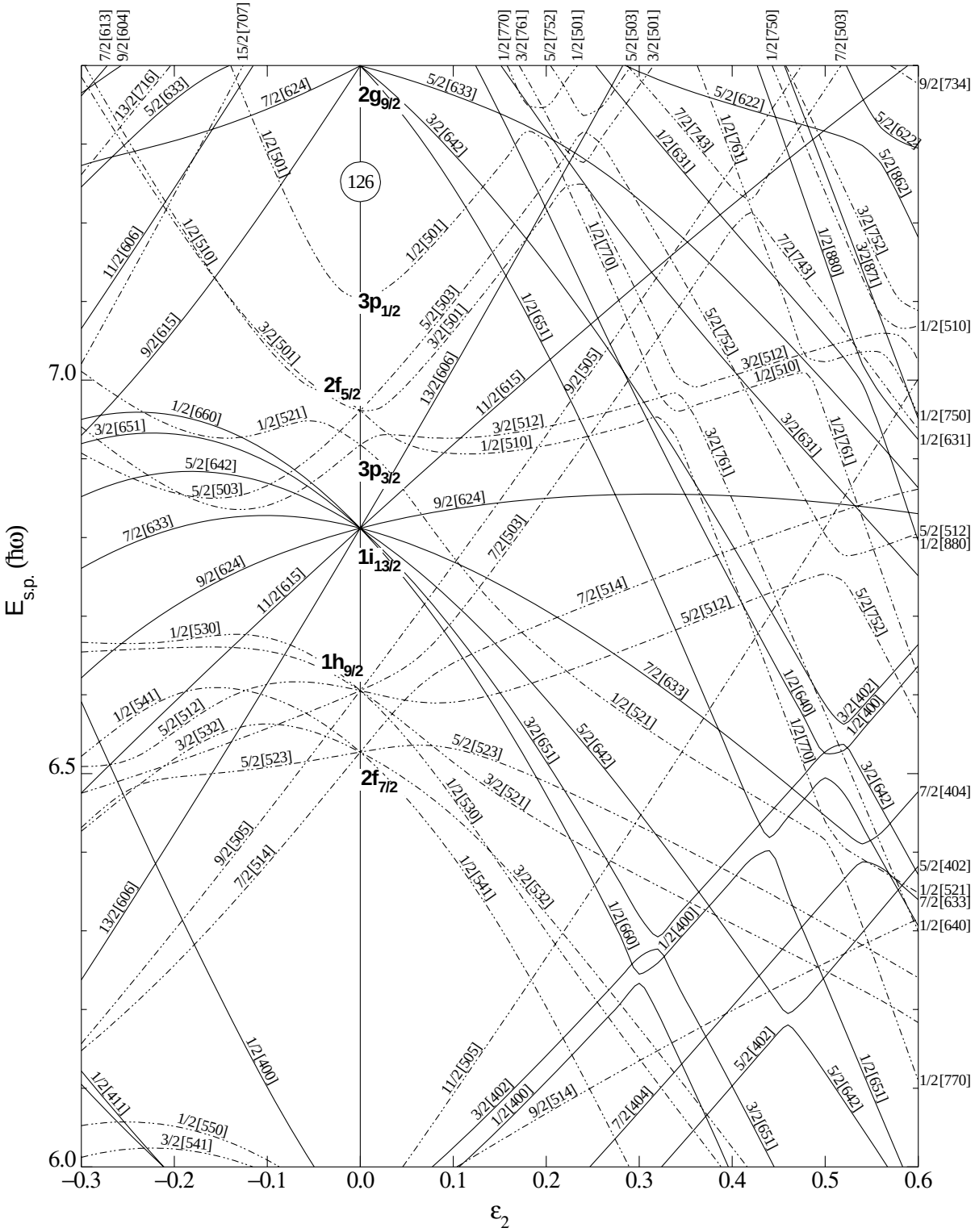


Figure 2.3: Nilsson diagram for neutrons, $82 \leq N \leq 126$ ($\epsilon_4 = \epsilon_2^2/6$). The solid and dashed lines correspond, respectively, to positive and negative parity. Reproduced from [Fir96].

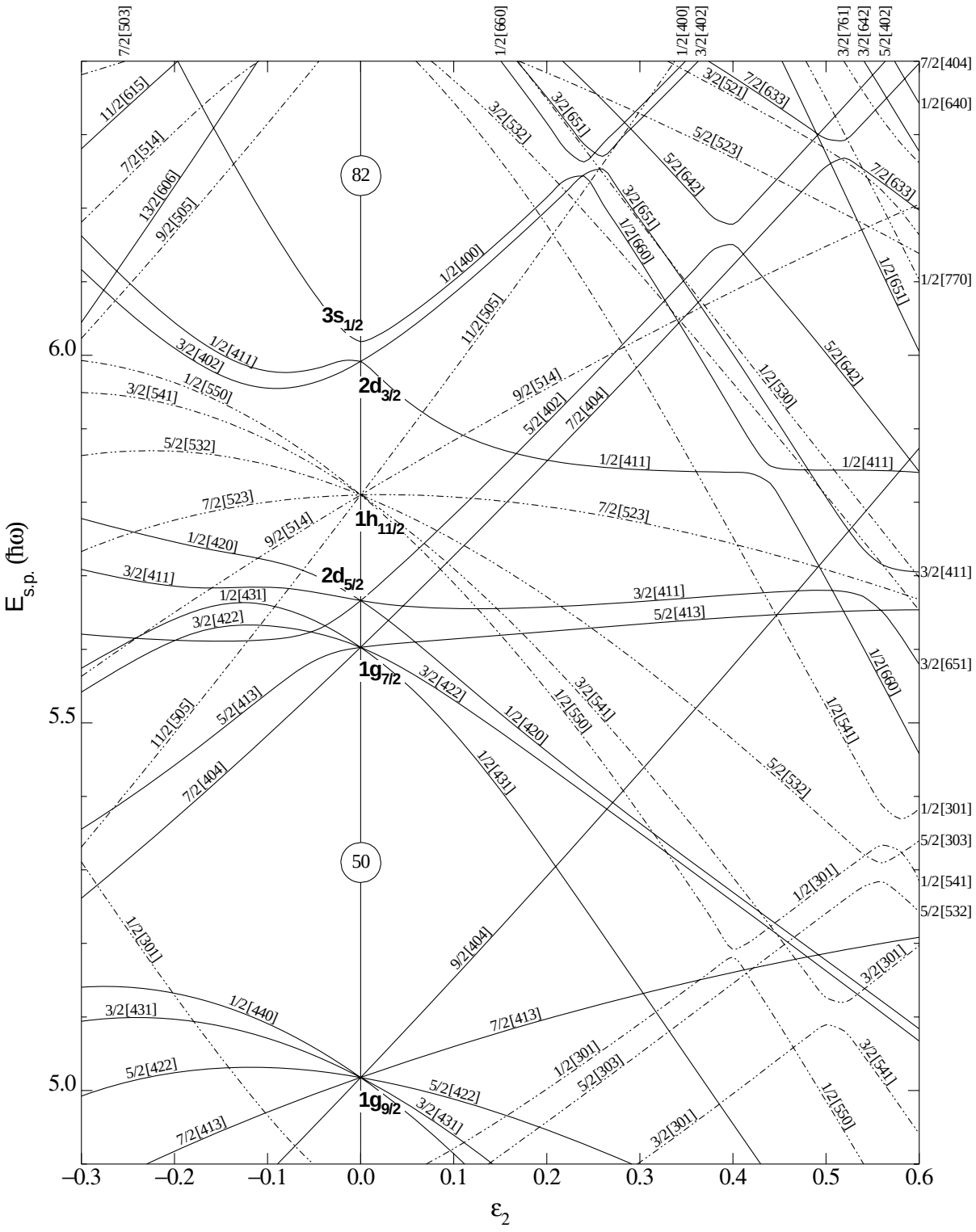


Figure 2.4: Nilsson diagram for protons, $50 \leq Z \leq 82$ ($\epsilon_4 = \epsilon_2^2/6$). Reproduced from [Fir96].

Fig. 2.3, at $\epsilon_2 \geq 0.3$ the 1/2[660] orbital becomes lower in energy than the 5/2[523]. If the 5/2[523] orbital is the last one to be occupied at $\epsilon_2 \sim 0.2$, this is not the case anymore at $\epsilon_2 \geq 0.3$ for an orbital that initially lies higher in energy, but is now closer to the Fermi surface. This has an important consequence for what would be observed experimentally - in our example a single particle state would have spin of 1/2 instead of the expected 5/2. Similar arguments, although not in such simple form, are employed in real situations as well.

The physics reasons for such "intruder" orbitals to emerge can be intuitively explained as follows. Since Ω is the projection of the total angular momentum on the z axis, classically there exists a functional dependence of the orientation of Ω with respect to the z axis for a given absolute value of j. Thus, the lowest possible value of Ω determines a smaller angle between the plane of the classical orbit of the nucleon with the core. In the quantum case, this would correspond to a higher overlap of their wave functions which would lower the energy.

We will briefly describe the other commonly used potential, the Woods-Saxon potential. The model employs an expression for the radial part of the potential as

$$V_{WS} = V_C + V_{SO} + \frac{1}{2}(1+\tau_3)V_{Coul}, \tag{2.14}$$

with central, spin-orbit, and Coulomb terms. For V_C we have the expression

$$V_C(\mathbf{r};\beta) = \frac{V_0}{1+exp(\mathrm{dist}(\mathbf{r};\beta;r_0)/a)}, \tag{2.15}$$

with $R = r_0 A^{1/3}$ and a is a diffuseness parameter. Note that since V_C has a form that closely resembles the nuclear density, no correction term of the form $\mathbf{l}^2 - \langle \mathbf{l}^2 \rangle$ needs to be added. The spin-orbit term has the form

$$V_{SO}(\mathbf{r};\beta) = -\lambda_{so}\frac{\hbar}{2mc}\vec{\bigtriangledown}\left[\frac{V_0}{1+exp(\mathrm{dist}(\mathbf{r};\beta;r_{so})/a_{so}}\right].(\sigma \times \mathbf{p}) \tag{2.16}$$

where σ are the Pauli matrices, p is the momentum. The functions dist() are the distances from point $\mathbf{r}$ to surfaces of general shape, determined from Eqn. 2.5. For the Coulomb term one has

$$V_{Coul}(\mathbf{r}) = \frac{1}{2}\int \frac{\rho(\mathbf{r})}{|\mathbf{r}-\mathbf{r}'|}d\mathbf{r}'. \tag{2.17}$$

The parameters of this potential are adjusted following the experimental data for the single-particle energies.

So far we have considered a Hamiltonian of the nuclear system that is based on a mean field approximation. Since mean field infers pure single-particle energies, it would leave a major part of experimental data unaccounted which suggests a collective mode in the

nucleus. Thus it is necessary that the short-range component of the nuclear interaction be included explicitly in the Hamiltonian. The most important part of that interaction, which brings observable effects, is the pairing between the nucleons. Pairing correlations were first introduced by Bardeen, Cooper, and Shrieffer as a microscopic mechanism of superconductivity (BCS theory). Due to close resemblance with nuclear systems, BCS theory was incorporated into nuclear structure theory [Boh58], as experimental observations supported the presence of pairing. One experimental finding that supported pairing was the well-known fact that all even-even nuclei have ground states with $I^\pi = 0^+$. Another finding was that the lowest non-collective excited states for an even-even nucleus lie at 1-2 MeV higher than the ground state ("energy gap"), as energy is needed to break a pair in order to introduce an internal excitation. Finally, the odd-even mass difference effect refers to larger binding energy of an even-even nucleus compared to the adjacent odd-A nuclei, which also suggested a presence of pairing.

2.5 The Cranked Shell Model

The Nilsson and Woods-Saxon models are suitable for describing the single-particle excitation states. However, this model cannot give information about excitations that are influenced by the rotation of the nuclear potential. In order to address this problem, the Cranked Shell Model (CSM) has been developed. Originally, it was introduced by Inglis [Ing54] for description of magnetic moments of molecules. However, in nuclear physics this model has also been proved to be quite successful [Ben79, Ben79a]. The CSM takes into account the influence of the angular momentum of the core on the individual nucleon motions. The Hamiltonian can be written as [Voi83]

$$H' = H - \omega J_x \tag{2.18}$$

where ω is the angular frequency of rotation and J_x is the angular momentum on an axis perpendicular to the z axis. The Hamiltonian H' effectively moves the reference frame from the laboratory to a body-fixed frame. In the laboratory frame we have

$$i\frac{\partial \Psi_{lab}}{\partial t} = H_{lab}\Psi_{lab}, \tag{2.19}$$

while in the rotating frame, the wave functions is transformed as

$$\Psi_{lab} = \Re\Psi_{int}, \tag{2.20}$$

where $\Re = e^{-iI_x\omega t}$ is the rotation operator about the x axis. The Hamiltonian is transformed as

$$H_{lab} = \Re H_{int}\Re^{-1}. \tag{2.21}$$

Combining Eqn. 2.19, 2.20, and 2.21 one obtains the Hamiltonian in the intrinsic frame:

$$H'_{int} = H_{int} - \omega J_x, \tag{2.22}$$

with the condition for a time independent Shrödinger equation in the intrinsic frame, $H'_{int}\Psi_{int} = E_{int}\Psi_{int}$. The energies of the single particle with respect to the rotating frame is

$$e_i = \langle i|h|i\rangle - \omega\langle i|j_x|i\rangle, \tag{2.23}$$

where h is a single-particle Hamiltonian in the rotating frame and j_x is its projection of the angular momentum. The energy determined by Eqn. 2.23 is called the *Routhian*. As we will mention further, in the analysis of the experimental data, Routhians are important since they carry information about the intrinsic structure. The total Routhian is defined as the sum of Routhians over all nucleons. The contribution of nucleon angular momentum in the rotating frame to the total angular momentum of the nucleus can be easily expressed in terms of the Routhian:

$$i_x = \langle i|j_x|i\rangle = -\frac{de_i}{d\omega}. \tag{2.24}$$

The quantity i_x is referred to as the *aligned angular momentum* or *alignment*. In the regime of very high spin, the total spin of the nucleus is approximately equal to its projection on the x axis ($I \approx I_x$), which infers that the total spin can be expressed as a sum over all alignments.

Only two quantum numbers emerge from the symmetries of H_{int} - the parity and the so-called *signature*. The latter quantum number is related to the symmetry of rotation about the x axis of an angle of π. If $\mathcal{R}_\pi = e^{-i\pi I_x}$, then its square would be

$$\mathcal{R}_\pi{}^2 = (-1)^A, \tag{2.25}$$

with eigenvalues of $\mathcal{R}$

$$r \equiv exp(-i\pi\alpha). \tag{2.26}$$

It is r that was originally called *signature* [BoM98], however, we will adopt α (the signature exponent) for that purpose due to its additivity (Frauendorf). From [BoM98] we get the following relations of the signature and the total spin I:

- for an even number of nucleons:

$$r = +1, \quad (\alpha = 0), \quad I = 0, 2, 4, ... \tag{2.27}$$

$$r = -1, \quad (\alpha = 1), \quad I = 1, 3, 5, ... \tag{2.28}$$

- for an odd number of nucleons:

$$r = +i, \quad (\alpha = -\frac{1}{2}), \quad I = \frac{3}{2}, \frac{7}{2}, \frac{11}{2}, ... \tag{2.29}$$

$$r = -i, \quad (\alpha = +\frac{1}{2}), \quad I = \frac{1}{2}, \frac{5}{2}, \frac{9}{2}, ... \tag{2.30}$$

which can be summarized with the selection rules

$$I = \alpha \bmod 2. \tag{2.31}$$

The Cranked Shell Model is best suited for description of $\delta I = 2$ rotational bands. All possible combinations of parity and signature correspond to a band which may be observed experimentally.

It is essential that the intrinsic structure on which a rotational band is built to be incorporated within the model. In the case when several orbitals are occupied around the Fermi level, they altogether would contribute to the total wave function. From an experimental point of view, the Fermi level can be conveniently defined as the last occupied orbital at a given deformation, provided that the number of particles is conserved. This can be illustrated in Fig. 2.3. If we have a filled $N = 82$ shell, adding an additional neutron would occupy the lowest 1/2[541] orbital which stems from $f_{7/2}$. If more neutrons are added, the residual interaction would start affecting the closed shell and the nucleus would favor a deformed shape. This is referred to as the *shape-driving* effect, which is especially prominent in the case of high-j downslopping orbitals such as $i_{13/2}$ or $j_{15/2}$. As the deformation increases, more orbitals start to mix and at the equilibrium shape the nucleus has its Fermi level shifted to a higher energy but with the requirement that the total number of nucleons be equal to N. For ^{174}Hf, the Fermi level for neutrons determined in this way is positioned in the subshell gap closed by 7/2[633], 1/2[521], 5/2[512], and 7/2[514] orbitals. The existence of such subshell gaps has far-reaching consequences as they can emerge along any degree of freedom. Jumping ahead we will mention that a shell gap along the γ deformation parameter is thought to be responsible for stabilizing a triaxial shape of nuclei. We will discuss the latter in Chapter 2.8 of this work.

To address the particle excitations around the Fermi level, we must introduce a unified way of describing simultaneously the occupied orbitals below ("hole space") and the empty orbitals above ("particle space") the Fermi level. This can be achieved by defining the so called Bogolyubov quasiparticles:

$$\beta_k^+ = U_{lk} c_l^+ + V_{lk} c_l \tag{2.32}$$

where summation on repeating indices is assumed. The operators c_k are vectors that contain annihilation operators below the Fermi level as well as creation operators above it. A CSM Hamiltonian in which the pairing has been taken into account can be written as

$$H_{qp} = H'_{int} - \Delta(\hat{P^+} + \hat{P}) - \lambda\hat{N}, \tag{2.33}$$

where Δ is the strength of the pairing, λ is a Lagrangian parameter of the requirement $\langle\hat{N}\rangle$ being equal to a fixed number of particles and $\hat{P^+}$ the operator creating the Cooper pairs:

$$\hat{P^+} = c_k^+ c_{\bar{k}}^+. \tag{2.34}$$

The equations for the Hartree-Fock-Bogolyubov approach in the cranking regime have the type

$$\begin{pmatrix} e_k^\omega - \lambda & \Delta \\ -\Delta & -(e_k^\omega - \lambda) \end{pmatrix} \begin{pmatrix} U_k \\ V_k \end{pmatrix} = \tilde{e}_k^\omega \begin{pmatrix} U_k \\ V_k \end{pmatrix}. \tag{2.35}$$

Here $\tilde{e}_k^\omega$ are the quasiparticle Routhians.

Since the Cranked Hamiltonian is written in the intrinsic frame, a correct description of the experimental data would require a transformation of the theoretical information to the laboratory frame. A convenient way of direct experimental observation of the crossings and alignments has been proposed by Bengtsson and Frauendorf [Ben79, Ben79a]. The excitation energy in the rotating frame is

$$E' = E_x - \omega I_x, \tag{2.36}$$

where I_x is the projection of the total angular momentum on the x axis. In the semi-classical regime when I is large, $I_x(I)$ can be derived from geometrical arguments as

$$I_x(I) = \sqrt{(I + \frac{1}{2})^2 + K^2} \tag{2.37}$$

where K is the projection of I on the symmetry axis, in the case when the angular momentum of the nucleus as a whole is perpendicular to the symmetry axis. The angular velocity can be conveniently associated to the laboratory excitation energy as

$$\omega(I) = \frac{dE(I)}{dI_x(I)} \tag{2.38}$$

which can be written in terms of finite differences as

$$\omega(I) = \frac{E(I+1) - E(I-1)}{I_x(I+1) + I_x(I-1)}. \tag{2.39}$$

Since the excitation energy E' contains contributions from the collective motion of the nucleus, it is necessary to subtract a reference energy from E' in order to extract e'. The same holds for the alignment:

$$e'(\omega) = E'(\omega) - E_{ref}(\omega), \quad i(\omega) = I_x(\omega) - I_{ref}(\omega). \tag{2.40}$$

The reference quantities can be modeled by treating of the term $-\omega I_x$ as a perturbation and including higher order terms into the expansion of E' [Har65]. For practical purposes, the following expression for the moment of inertia is used:

$$\mathcal{I} = \mathcal{I}_0 + \omega^2 \mathcal{I}_1, \tag{2.41}$$

where $\mathcal{I}_0$ and $\mathcal{I}_1$ are the so-called Harris parameters, which can be adjusted for each nucleus. Correspondingly, for the reference angular momentum one obtains

$$I_{ref}(\omega) = \omega\mathcal{I} = \omega\mathcal{I}_0 + \omega^3\mathcal{I}_1. \tag{2.42}$$

The reference energy is derived by integrating Eqn. 2.42 with respect to the rotational frequency,

$$E_{ref}(\omega) = -\int I_{ref}(\omega)d\omega = -\frac{1}{2}\omega^2\mathcal{I}_0 - \frac{1}{4}\omega^4\mathcal{I}_1 + \frac{1}{8\mathcal{I}_0}. \tag{2.43}$$

Note that the latter is necessary in order to account for the change of the moment of inertia, according to Eqn. 2.41. This naturally introduces two types of moment of inertia, namely *dynamic* and *kinematic*, defined as

$$\mathcal{I}^{(1)} = I_x \left(\frac{dE}{dI_x}\right)^{-1} = \frac{I_x}{\omega} \quad \hbar^2/\mathrm{MeV}^{-1} \tag{2.44}$$

$$\mathcal{I}^{(2)} = \left(\frac{d^2E}{dI_x^2}\right)^{-1} = \frac{dI_x}{d\omega} \quad \hbar^2/\mathrm{MeV}^{-1}. \tag{2.45}$$

The kinematic moment of inertia $\mathcal{I}^{(1)}$ addresses the static properties of the nucleus like deformation and pairing, while the dynamical moment of inertia reflects the response of the nucleus to a force. The quantity $\mathcal{I}^{(2)}$ is thus more sensitive to internal changes of the nucleus. Experimentally, $\mathcal{I}^{(1)}$ and $\mathcal{I}^{(2)}$ can be calculated as

$$\mathcal{I}^{(1)} = \frac{2I - 1}{E_\gamma(I \to I-2)} \quad \hbar^2/\mathrm{MeV}^{-1} \tag{2.46}$$

$$\mathcal{I}^{(2)} = \frac{4}{E_\gamma(I+2 \to I) - E_\gamma(I \to I-2)} \quad \hbar^2/\mathrm{MeV}^{-1}. \tag{2.47}$$

It can be seen from Fig. 2.5 that at the crossing frequencies the alignment should experience a change as higher quasiparticle Routhian orbitals become lower in energy. At that point, the paired nucleons are aligned along the rotational axis of the nucleus. This would introduce a change of the internal structure which can be regarded as the crossing of bands with different moments of inertia. These moments are influenced predominantly by the additional moment of inertia the broken pair carries. This effect can be significant as the size of the pair is of order of ~ 50 fm. Experimentally, an abrupt jump of the alignment would be observed. The latter can be understood in terms of angular momentum conservation. If $\omega_g \mathcal{J}_g$ is the angular momentum before the crossing, and $\omega_s \mathcal{J}_s + i_s$ is the angular momentum after the pair break, then

$$\omega_s \mathcal{J}_g = \omega_s \mathcal{J}_s + i_s \approx \omega_c \mathcal{J}_s + i_s. \tag{2.48}$$

It is clear that the rotational frequency after the crossing frequency ω_c can be lower, which is a commonly observed phenomena called *backbending*. However, it has to be pointed out that Eqn. 2.48 should be used as qualitative guidance only. In the case when the interaction of the crossing bands is large, the crossing would be observed as a gradual increase of the alignment. The latter is referred to as an *upbend*. The nature of the upbend is not unique and other mechanisms of its interpretation can be applied, such as change of the deformation, rather than breaking a pair. We will encounter an example of such an effect later on.

Plots of the quasiparticle Routhians are implemented as function of the rotational frequency. An example of such a plot is shown in Fig. 2.5. The deformation parameters are taken from Total Routhian Surface ("TRS") calculations, which will be introduced in Section 2.7. The actual calculations for crossing frequencies and alignment gains are also deduced from Fig. 2.5 and Fig. 2.6, both for neutrons and protons, respectively.

As seen from the figure, the evolution of the quasiparticle Routhians with rotational frequency is quite complicated. However, rich information can be extracted related to orbital occupation and crossings. The rules for reading such diagrams is described briefly as follows.

The vacuum state of the nucleus corresponds to all of the levels with negative energy being occupied and all with positive energy being empty. As the rotational frequency increases, the orbitals above the Fermi level (corresponding to $\widetilde{e}_k^{\omega} - \lambda = 0$) become lower in energy, and cross with orbitals that are occupied. In the case of the ground state, such an encounter would happen at $\hbar\omega = 0.3\,\mathrm{MeV}$ (Fig. 2.5), where an interaction between $\pm$A and $\pm$B levels occur. This is referred to as an AB *crossing*. After the crossing, the nucleon pair is broken and the single quasineutrons align their angular momenta along the rotational axis of the nucleus. Experimentally, a gain in the alignments of the rotational band would

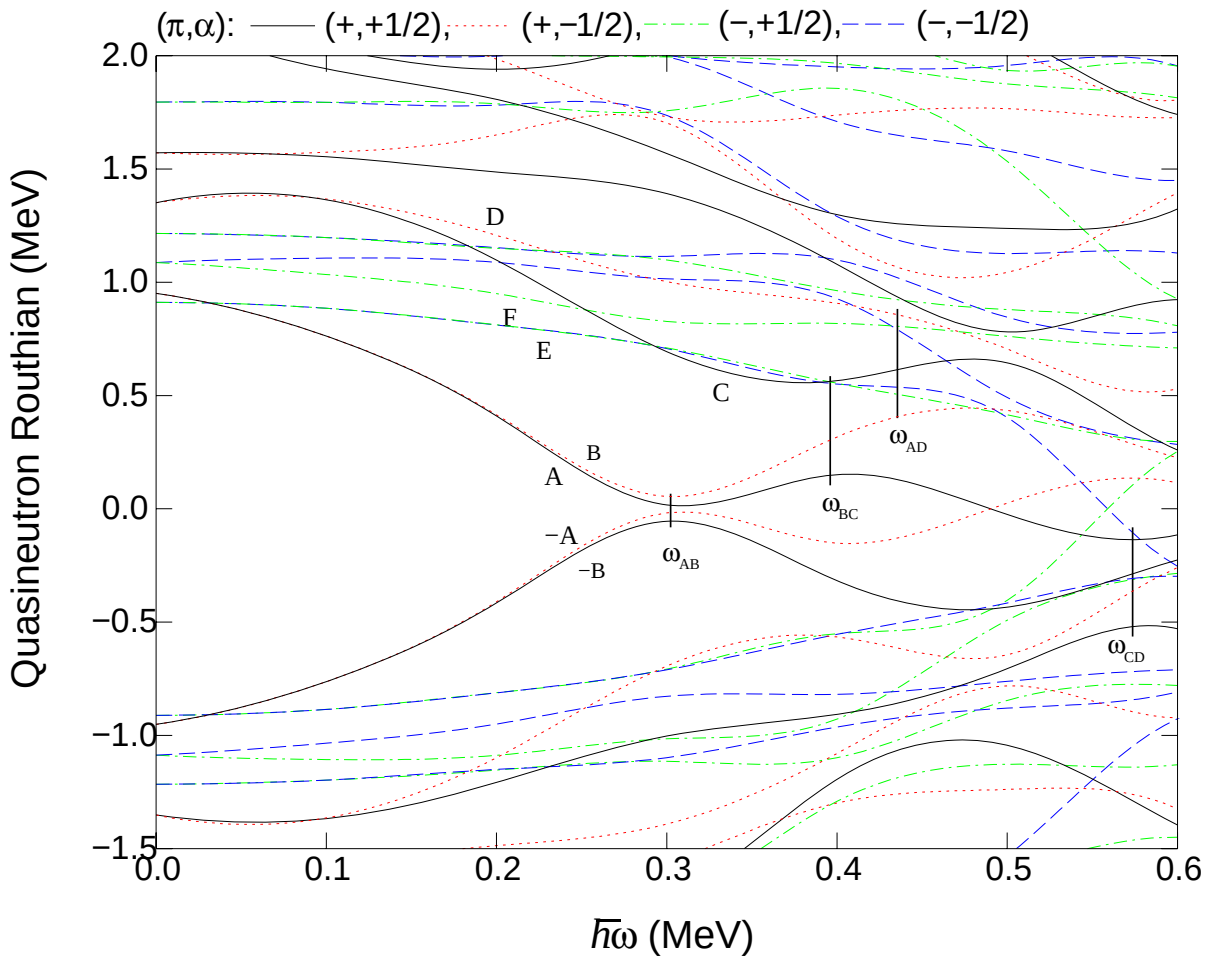


Figure 2.5: Quasiparticle Routhians for neutrons for ^{174}Hf. The deformation parameters $\beta_2 = 0.291$, $\beta_4 = -0.016$, $\gamma = -0.4°$ are chosen, corresponding to a shape at a rotational frequency $\hbar\omega = 0.253\,\mathrm{MeV}$. The first neutron crossing is identified at 0.3 MeV.

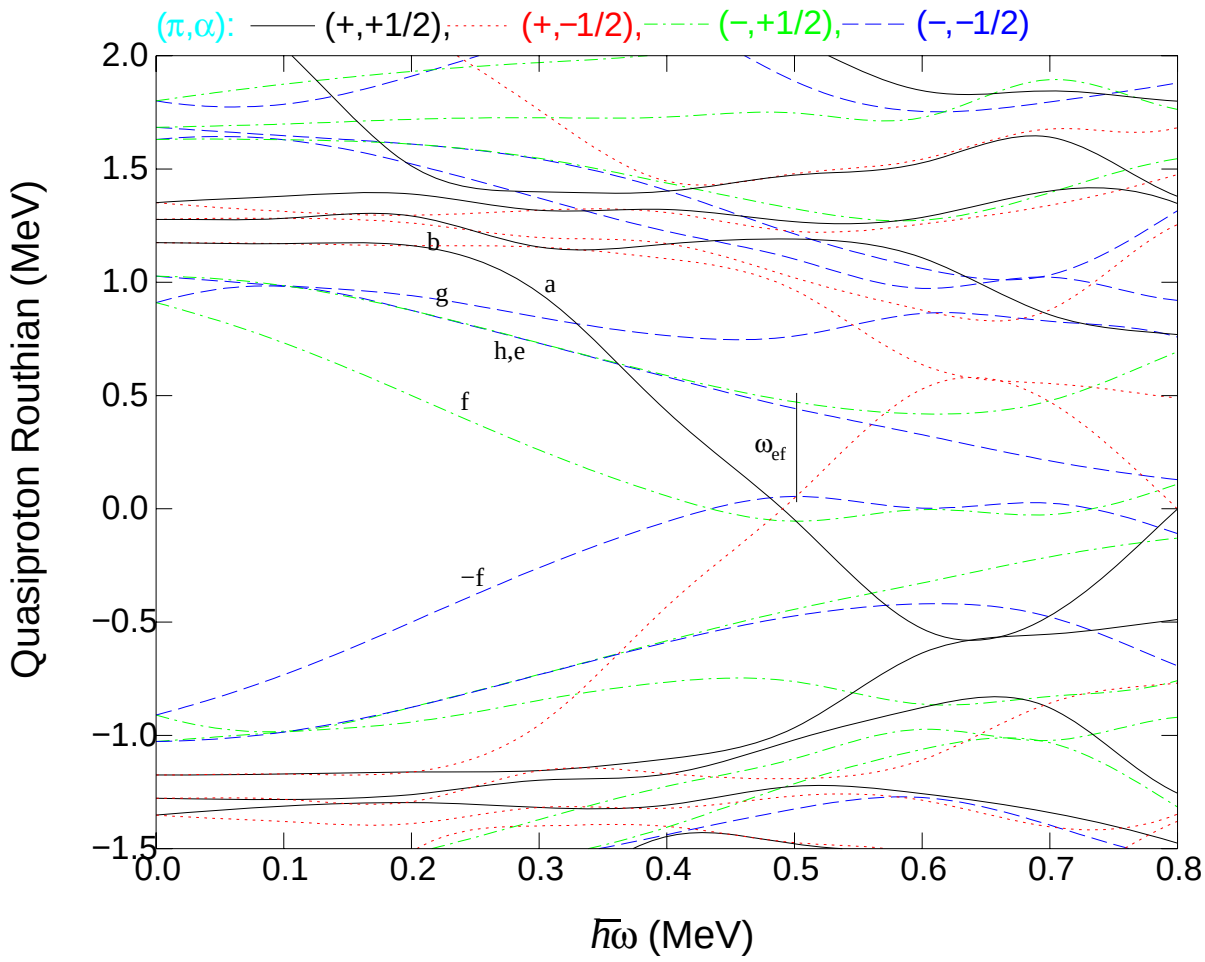


Figure 2.6: Quasiparticle Routhians for protons for ^{174}Hf. The deformation parameters $\beta_2 = 0.291$, $\beta_4 = -0.016$, $\gamma = -0.4°$ are chosen, corresponding to a shape at a rotational frequency $\hbar\omega = 0.253\,\mathrm{MeV}$. The first proton crossing is identified at $\sim 0.50\,\mathrm{MeV}$.

Table 2.1: Convention for quasiparticle orbitals notation. The subscript denotes the ordering of the orbitals ascending with energy.

Orbital	Neutrons	Protons	Orbital	Neutrons	Protons
$(+,+\frac{1}{2})_1$	A	a	$(+,+\frac{1}{2})_3$	I	i
$(+,-\frac{1}{2})_1$	B	b	$(+,-\frac{1}{2})_3$	J	j
$(+,+\frac{1}{2})_2$	C	c	$(+,+\frac{1}{2})_4$	K	k
$(+,-\frac{1}{2})_2$	D	d	$(+,-\frac{1}{2})_4$	L	l
$(-,-\frac{1}{2})_1$	E	e	$(-,-\frac{1}{2})_3$	M	m
$(-,+\frac{1}{2})_1$	F	f	$(-,+\frac{1}{2})_3$	N	n
$(-,-\frac{1}{2})_2$	G	g	$(-,-\frac{1}{2})_4$	O	o
$(-,+\frac{1}{2})_2$	H	h	$(-,+\frac{1}{2})_4$	P	p

be observed.

Note that if the lowest orbitals with positive energy are occupied, there will be no crossing due to the Pauli exclusion principle. In this case we refer to it as a *blocked* crossing. However, other crossings (like BC or AD) are possible at higher rotational frequency. In the case that an orbital higher in energy is occupied, crossings that occur at low frequency will be observed. The quasiparticle Routhian plots (or simply "Routhians") can predict the exact amount of alignment gain by simply adding the corresponding single-particle alignment according to Eqn. 2.24, which is used in determination of the possible initial quasiparticle configuration.

In high-spin spectroscopy the arrangement is accepted such that the quasiparticle Routhians are labeled with letters A, B, C, ... for neutrons and a, b, c,... for protons. Table 2.1 summarizes the notation.

2.6 The $B(M1)/B(E2)$ ratio

As an additional test to determine the configuration of observed two-quasiparticle bands, the $B(M1)/B(E2)$ ratio as well as the $g_K - g_R$ values were measured. Both quantities are sensitive to the quasiparticle configuration. The gyromagnetic ratios of the collective motion and single quasiparticles, g_R and g_K, reflect closely the intrinsic configuration of the nucleus. The $B(E2)$ transition strength is given by the rotational model [BoM98] as

$$B(E2, I_i \rightarrow I_f) = \frac{5}{16\pi} e^2 Q_0^2 | < I_i 2K0 | I_f K > |^2 \quad (eb)^2, \tag{2.49}$$

Table 2.2: Calculated g_K factors for orbitals that are near the Fermi level in ^{174}Hf. Next to the Nilsson orbitals are given the corresponding quasiparticle orbital labels.

Orbital	g_K
ν 7/2[633] (A,B)	-0.29
ν 5/2[512] (E,F)	-0.41
ν 1/2[521] (H,G)	1.35
π 1/2[541] (f,e)	0.92
π 7/2[404] (a,b)	0.61
π 5/2[402] (c,d)	1.57

where Q_0 is the intrinsic quadrupole moment,

$$Q_0 = \frac{3}{\sqrt{5\pi}} R_0^2 Z\beta(1+0.16\beta), \quad R_0 = r_0 A^{1/3}. \tag{2.50}$$

The $M1$ transition strength between the two signatures can be deduced employing the geometrical model [Don87] [Fra81],

$$B(M1, I_i \to I_f) = \frac{3}{8\pi I^2}\{\sqrt{I^2-K^2}[(1-\frac{\Delta e'}{\omega})(g_K - g_R)K_1 + \sum_l (g_{K_l} - g_R)K_l] - \\ - K\sum_m (g_{K_m} - g_R) i_m\}^2 \quad \mu_N^2, \tag{2.51}$$

where $K = \sum_l K_l$. The sums run over all quasiparticles that couple to form the band and $\Delta e'$ is the signature splitting. The values i_l are their initial alignments. A fixed value of $g_R = 0.7\frac{Z}{A}$ was used and values depending on the orbitals' wave functions were calculated for g_K. The calculated values are shown on Table 2.2.

The theoretical values for the $B(M1)/B(E2)$ ratio can be compared experimentally with the formula [BoM98]

$$\frac{B(M1, I \to I-1)}{B(E2, I \to I-2)} = 0.693 \frac{E_\gamma^5(I \to I-2)}{E_\gamma^3(I \to I-1)} \times \frac{1}{\lambda(1+\delta^2)} \quad \left(\frac{\mu_N}{eb}\right)^2, \tag{2.52}$$

where E_γ is the γ-ray energy in MeV, and λ is the branching ratio,

$$\lambda = \frac{I_\gamma(I \to I-2)}{I_\gamma(I \to I-1)}. \tag{2.53}$$

The quadrupole-dipole mixing ratio δ can also be deduced from the data using the relation

$$\frac{\delta^2}{1+\delta^2} = \lambda \left(\frac{\langle IK20|I-1K\rangle}{\langle IK20|I-2K\rangle}\right)^2 \frac{E_\gamma^5(I \to I-1)}{E_\gamma^5(I \to I-2)}, \tag{2.54}$$

where the energy E_γ is in MeV.

Once the magnitude for δ is determined, it can be used to determine $g_K - g_R$ from the experimental data using the equation

$$\frac{g_K - g_R}{Q_0} = 0.933 \frac{E_\gamma(I \to I-1)}{\delta \times \sqrt{I^2 - 1}}. \tag{2.55}$$

In addition, the $B(E1)/B(E2)$ ratio is also used further in this work, defined as

$$\frac{B(E1, I \to I-1)}{B(E2, I \to I-2)} = 0.77 \frac{E_\gamma^5(I \to I-2)}{E_\gamma^3(I \to I-1)} \times \frac{1}{\lambda} \quad \left(10^{-6}\,\mathrm{fm}^{-2}\right), \tag{2.56}$$

where λ is the branching ratio, and E_γ is in MeV.

2.7 Shell Corrections

The Liquid Drop Model describes well the bulk properties of the nuclei, which formally have a continuous behavior. On the other hand, the observed oscillations in the binding energy clearly show the presence of shell effects, which cannot fit in the framework of a liquid drop. Both effects are essential for an adequate description of nuclei and it is important that they be incorporated into an united picture. Such a procedure was introduced by Strutinski [Str67, Str68]. The method is based on an averaging of the oscillation part of the total rotational energy through the substitution of the discrete level density from CSM with a smooth distribution. The total energy is written in a form in which the different types of energies are separated explicitly,

$$E_{\mathrm{tot}}(\beta, I) = E_{\mathrm{LDM}}(\beta, I) + E_{\mathrm{osc}}(\beta, I) + E_{\mathrm{pair}}(\beta, I), \quad \beta = (\beta_2, \beta_4, \gamma), \tag{2.57}$$

where E_{LDM} is the rotational energy in LDM at spin zero, E_{osc} is the oscillation part. The energy E_{pair} accounts for the pairing, and it can be written separately if it is not considered to be a part of E_{osc}. Now E_{osc} is written as

$$E_{\mathrm{osc}}(\beta, I) = E_\omega - \tilde{E_\omega}, \tag{2.58}$$

where E_ω is the total Routhian of the system and $\tilde{E_\omega}$ its mean part. With the introduction of the level density $\rho(e^\omega)$, for which some smooth distribution can be used, the mean Routhian can be expressed as

$$E_\omega(\beta, I) = \int_{-\infty}^{\lambda} \rho(e^\omega) e^\omega de^\omega, \tag{2.59}$$

where the Fermi level λ is determined from the requirement for particle number conservation. The notation e^ω emphasizes the dependence of the single-quasiparticle Routhian e on the

rotational frequency ω. The rotational frequency dependence of the spin is calculated in a similar manner as Eqn. 2.48 with the use of a spin density function. This function is the average of the $\langle j_x \rangle$ along the Routhian orbitals,

$$\rho_I(e^\omega) = \sum_\nu \langle j_x \rangle \rho(e^\omega), \tag{2.60}$$

and then for the spin we obtain

$$I_\omega = \int_{-\infty}^{\lambda} \rho_I(e^\omega) e^\omega de^\omega. \tag{2.61}$$

Then, the obtained full energy is a function of spin and deformation, which allows the tracking of the evolution of the equilibrium shape of the nucleus with spin.

This method is used for calculating the equilibrium minima for different quasiparticle configurations. In this work we used a code that performs Total Routhian Surface calculations, developed by Nazarewicz *et al.* [Naz85], and Wyss *et al.* [Wys88]. Sample output calculations are shown in Fig. 2.7. The change in the energy surface with frequency can be noticed in panel b), namely the development of a "valley" (denoted by the black ellipses), which is a precursor of a sudden change in the equilibrium shape. Physically, the latter is related to a crossing, which indeed can be identified when a detailed examination of the change of spin with frequency is performed. Since such surfaces can be calculated for any seniority, the crossings for higher quasiparticle number excitations can be estimated as well. However, it has to be kept in mind that the frequency values do not vary continuously in the code. This poses limitations on the "resolution" of the plot and thus it affects the estimated value of the crossing. Other limitations come from the estimated value of pairing, which is completely model dependent [Wys88].

In the current work, the TRS plots have been used as a guidance for the estimation of the deformation parameters that are used in CSM calculations. For the needs of the high-spin analysis, plots of all possible two-quasiparticle configurations were produced and compared with data. The pairing gap in CSM calculations was chosen to be approximately equal to the expected static pairing ($\sim$ 1 MeV) for the nucleus of interest, ^{174}Hf, derived from the odd-even mass difference.

2.8 Superdeformation

The shape of the nucleus is an important bulk characteristic. As we will see in the later chapters, the placement of the single-particle orbitals with respect to the Fermi surface depends very much on the evolution of its shape as rotational frequency increases. This

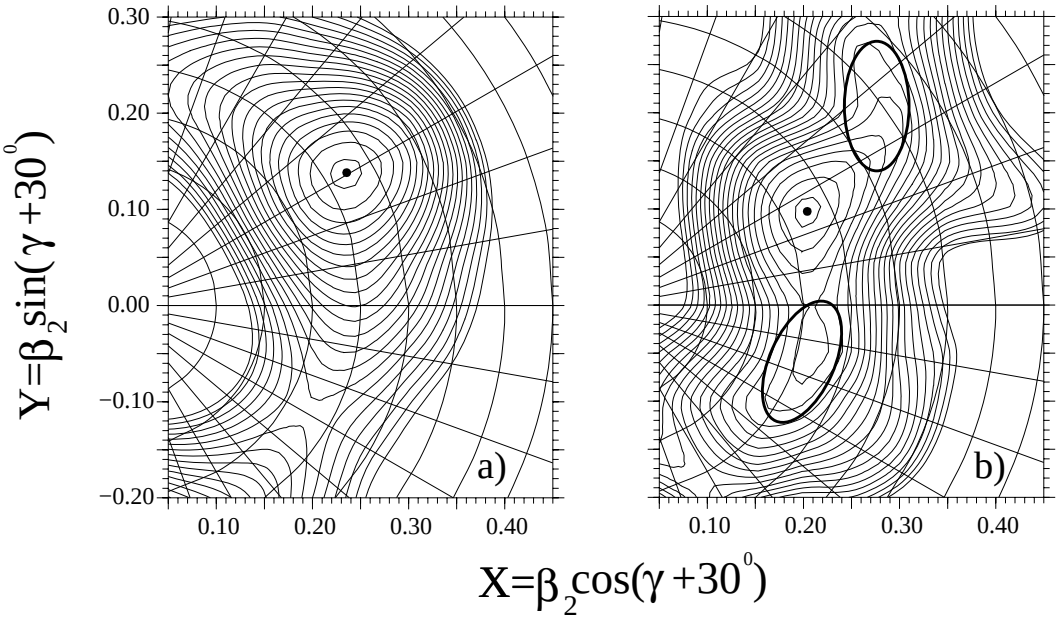


Figure 2.7: A sample Total Routhian Surface, calculated for ^{174}Hf for the ground state configuration (0 quasiparticles). Panel a) shows the energy surface at $\hbar\omega = 0\,\mathrm{MeV}$. The corresponding equilibrium deformation parameters are $\beta_2 = 0.273$, $\beta_4 = -0.022$, and $\gamma = 0.4°$. Panel b) is calculated at $\hbar\omega = 0.455\,\mathrm{MeV}$, which yields deformation parameters $\beta_2 = 0.226$, $\beta_4 = -0.043$, and $\gamma = -4.5°$.

process is self consistent. The Coriolis and centrifugal forces simultaneously reduce the pairing and change deformation by centrifugal stretching, which allows a change in the quasiparticle occupation for orbitals that are higher in energy - smearing out the Fermi surface. In addition, it becomes possible for orbitals from higher shells to cross the Fermi surface, which in turn affects the favored lowest energy of the nucleus at that rotational frequency. As a result, the arrangement of orbitals at high spin could create "subshell gaps"- energy gaps that separate groups of levels at non-zero deformation. It has to be pointed out that such gaps are not static (for example, an ordering of levels derived from the Nilsson Hamiltonian), rather, they are dynamic, i.e., they evolve with rotational frequency. Such gaps play a central role in stabilizing the bulk shape of the nucleus at high spin [Nee76].

A picture of the single-particle orbitals derived from a pure harmonic oscillator as a function of deformation is shown in Fig. 2.8. For comparison, recall also orbitals from Fig. 2.3 and Fig. 2.4, which are derived from a Hamiltonian that includes additional spin-orbit terms. The presence of shell gaps is shown in a clear way. Ratios between the big and the small axes of the deformed rotor are displayed as well. It should be noted the change

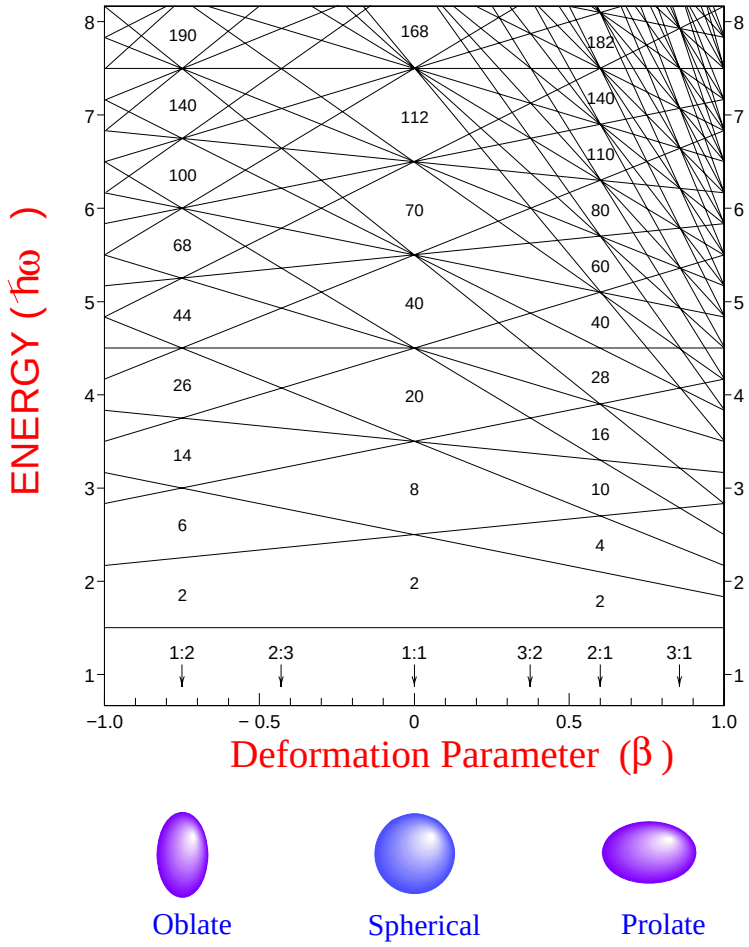


Figure 2.8: The single particle levels calculated by using a simple harmonic oscillator potential for the case of axial symmetry. Note the change of shell gaps as a function of deformation. See [Nil95], p.116.

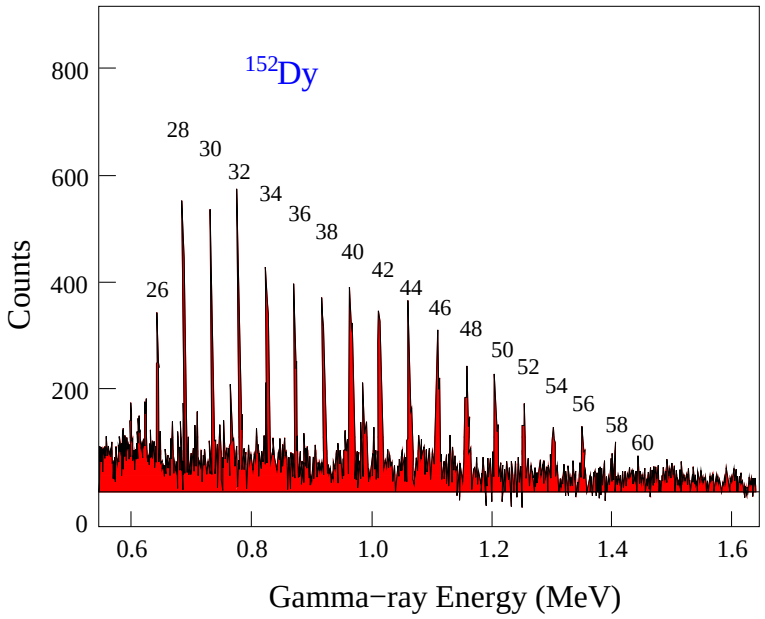


Figure 2.9: A γ-ray spectrum measured for the superdeformed band in ^{152}Dy and its spin assignments. Reproduced from [Twi86].

of the shell gaps with this ratio. A typical ratio for superdeformed shape is 2:1. Same a trend is observed in more realistic calculations as well. Early predictions of superdeformed shapes based on potential-energy surfaces have been done in [Nee75, Nee76, Ben75]. The first experimental discovery of a rotational band that is built on a superdeformed shape in ^{152}Dy is attributed to Twin *et al.* [Twi86]. Since then, many superdeformed bands have been identified in mass regions $A \sim 30$, 60, 135, 150, and 190 [Fir97]. A typical spectrum of a superdeformed band is shown in Fig. 2.9. It can be noted the regularity of the energy differences between the γ-ray transitions in the spectrum measured for this band, which are much smaller than the spacing between transitions in normal deformed bands. Such a characteristic is common for all superdeformed bands and indicates a large second moment of inertia, since it is inversely proportional to the energy spacing (see Eqn. 2.44). However, the moment of inertia alone cannot firmly manifest a high deformation, since variations in both pairing and quasiparticle alignment can play a role as well. A decisive determination of the scale of deformation must be done in a more direct way, namely, by determining the transition probabilities between the states of the band through measuring lifetimes of the nuclear levels. In this work, studies concentrate on deformation of the newly found superdeformed bands in ^{174}Hf [Djo03], presented in Chapter 4.

2.8.1 Wobbling

The central work in this dissertation is dedicated to a study of a particular phenomenon related to superdeformation. As of the moment of writing, there is a considerable experimental effort in searching for superdeformed bands in the mass $A \sim 170$ region. It was initially induced by a novel mode of motion that has been proposed to emerge in the regime of rotating superdeformed shapes.

An extensive experimental and theoretical study of ^{165}Lu [ScP95] noted the similarity of strongly deformed bands both in ^{165}Lu and ^{163}Lu, built on the $\pi i_{13/2}$ orbital. Theoretical calculations performed by the Ultimate Cranker code ([ScP95] and references within) revealed the presence of minima at high deformation in the total energy surface which did not possess an axial symmetry. Rather, minima that correspond to triaxial shapes (i.e., the ellipsoid has different moments of inertia along all of its principal axes) were observed. These minima proved to develop for all combinations of parity and signature for both nuclei. A suggestion was made that these triaxial shapes are a common feature for the mass region, and that the new band discovered in ^{165}Lu could be classified as triaxial as well.

A triaxial shape is associated with a characteristic mode of motion called "wobbling". It was discussed first by Bohr and Mottelson [BoM98]. The concept is illustrated in Fig. 2.10. In the case of axial symmetry, the orientation of the total angular momentum in the rigid-body reference frame is along the axis that has the largest moment of inertia. In the triaxial case, the total angular momentum might not lie into any of the principal planes of the ellipsoid. Thus, the angular momentum can point in any direction in space. In addition, the angular momentum can precess around its fixed direction. Similar precession is observed in the case of classical asymmetric rotor placed in a gravitational field. Such precession in the quantum case is addressed as wobbling.

For small deviation from the axis of the total angular momentum, wobbling is very much like harmonic oscillation. The corresponding wobbling quanta will be associated with an additional degree of freedom of precession around the symmetry axis which can be imposed on the motion of a classical symmetric top. The Hamiltonian of a triaxial top can be written as [BoM98]

$$H = \frac{1}{2}\left(\frac{J_1^2}{\mathcal{J}_1} + \frac{J_2^2}{\mathcal{J}_2} + \frac{J_3^2}{\mathcal{J}_3}\right), \tag{2.62}$$

where $\mathcal{J}_i$ are the corresponding moments of inertia about the principal axes. The angular momenta J_i satisfy the usual commutation relations $[J_i, J_j] = iJ_k$, and their squared sum adds to the total angular momentum,

$$J_1^2 + J_2^2 + J_3^2 = J^2 \;\; (= I(I+1))\,. \tag{2.63}$$

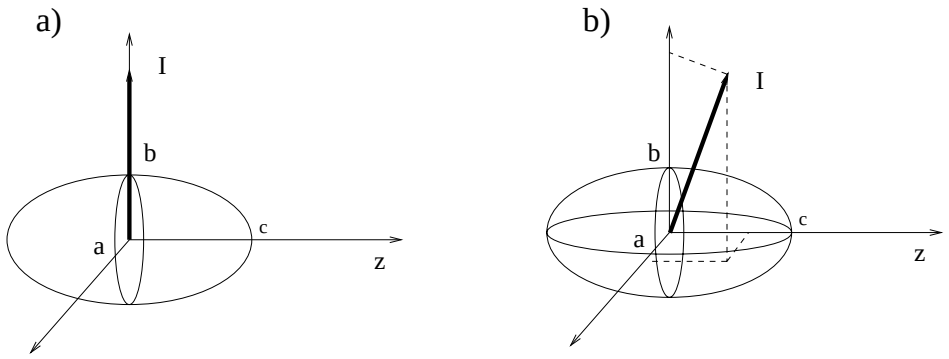


Figure 2.10: The axial and triaxial shapes differ in the ways the total angular momentum I can be oriented in space. a) In an axial nucleus, $(a = b) \neq c$, an orientation along an axis perpendicular to the symmetry axis is favorable. b) In the case of a triaxial nucleus, $(a \neq b \neq c)$, all axes can have a different projection of the total angular momentum.

By the use of Eqn. 2.63, the Hamiltonian can be written as

$$H = \frac{1}{2}\left(\frac{J^2}{\mathcal{J}_1} + J_2^2\left(\frac{1}{\mathcal{J}_2} - \frac{1}{\mathcal{J}_1}\right) + J_3^2\left(\frac{1}{\mathcal{J}_3} - \frac{1}{\mathcal{J}_1}\right)\right). \tag{2.64}$$

The Hamiltonian can be transformed into an expression closely resembling a harmonic oscillator added to a rigid rotor. In order to do that, it is sufficient to assume that the dominant angular momentum (for example, J_1) reaches its classical limit, which for superdeformed rotational bands is a very good approximation:

$$[J_2, J_3] = iJ_1 \approx iI. \tag{2.65}$$

This commutation relation closely resembles the one of the linear harmonic oscillator $[x, p] = i$, with the formal substitution of $J_2 = x$ and $J_3 = pI$. One now can write an equation identity between the Hamiltonians of a harmonic oscillator and the perturbative part of Eqn. 2.64 :

$$\frac{1}{2}x^2\left(\frac{1}{\mathcal{J}_2} - \frac{1}{\mathcal{J}_1}\right) + \frac{1}{2}(pI)^2\left(\frac{1}{\mathcal{J}_3} - \frac{1}{\mathcal{J}_1}\right) \equiv \frac{1}{2}kx^2 + \frac{1}{2M}p^2, \tag{2.66}$$

where we have used the formal expression for J_2 and J_3. Now the wobbling frequency can be easily deduced from

$$\Omega_w = \sqrt{\frac{k}{M}} = \frac{I}{\mathcal{J}_1}\sqrt{\frac{(\mathcal{J}_1 - \mathcal{J}_2)(\mathcal{J}_1 - \mathcal{J}_3)}{\mathcal{J}_2\mathcal{J}_3}}. \tag{2.67}$$

It should be noted that Ω_w is non-zero only if the moments of inertia are different, i.e., in case the geometrical shape of the rotor is not axial. The total energy spectra of the triaxial

top takes the form

$$E_{I,n_w} = \frac{I(I+1)}{2\mathcal{J}_1} + \hbar\Omega_w(I)\left(n_w + \frac{1}{2}\right). \tag{2.68}$$

This quantization is expressed in terms of wobbling quanta n_w. Experimentally, a triaxially deformed nucleus would exhibit a family of rotational bands, each corresponding to a different wobbling quantum number. Of great importance is also that their moments of inertia and alignments will not change since no intrinsic rearrangements of the structure of the nucleus has taken place.

Neergård *et al.* [Nee76] pointed out that the wobbling frequency could be calculated more accurately, if the precise energy of an internal configuration is known. In this case, a more accurate estimation of the direction of the total angular momentum deviation from the principal axes can be done. The question about stability of such configurations was also posed.

Calculations based on the particle-rotor model [Ham02, Ham03] give the expected experimental characteristics of the linking transitions between the bands that correspond to different wobbling quanta. Illustration of the behavior of the two rotational regimes is given in Fig. 2.11. The intrinsic configuration is represented by the angular momentum j. In the cranking regime (i.e., when the total angular momentum still coincides with one of the principal axes of the nucleus), contribution to the total angular momentum comes from both j and R. A rearrangement of the internal configuration takes place (the alignment of j), as well as increasing of the angular momentum R of the core. In the wobbling mode, only the core contributes to the deviation of the total angular momentum from the rotational axis, leaving the intrinsic configuration unchanged. In addition, the model predicts a domination of a $E2$ character of the $\Delta n_w = 1$, $I \to I-1$ transition over the $M1$.

The two experimental features, a) similar moments of inertia and alignment for wobbling partners, and b) enhanced $E2$ character of a $\Delta I = 1$ linking transitions between them, serve as decisive observational characteristics for identifying the wobbling motion.

To date, the particle-rotor model has been able to describe the rotational bands in the odd-A Lu isotopes. A family of three bands was observed in ^{163}Lu [Jen02, Jen02a]. It was suggested that all three are based on the same $\pi i_{13/2}$ configuration. Since this orbital is an intruder in this mass region, it introduces a higher deformation in comparison with other structures observed in this nucleus. The bands have been labeled *triaxial strongly deformed* ("TSD"). In addition, linking transitions were observed from the two excited sequences to the yrast ($n_w = 0$) TSD band in ^{163}Lu. Analysis of the linking transitions from the yrare ($n_w = 1$) TSD band revealed that the $\Delta I = 1$ transitions have a dominant $E2$ component, consistent with the wobbling predicted by the particle-rotor model [Ode01]. These experimental findings constitute the best evidence to date for the rotation of a triaxial

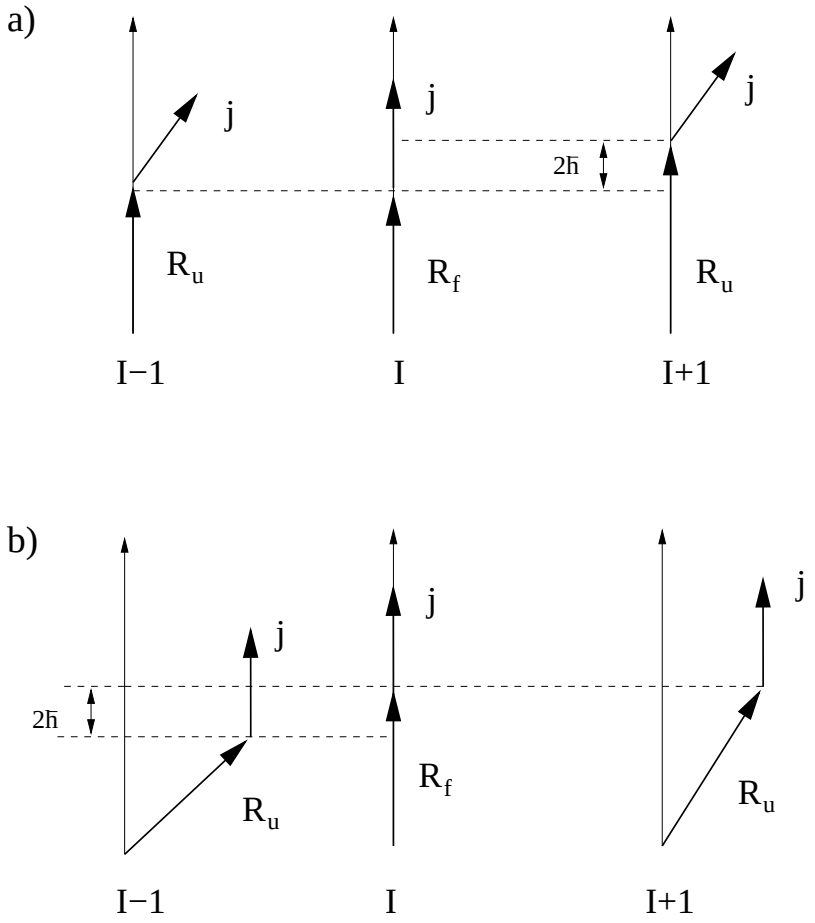


Figure 2.11: Scheme of the coupling of the angular momenta j of the particle and the core R in the case of a) Cranking regime and b) the wobbling mode. The total angular momentum is $I = R + j$. The subscripts denote the favored and unfavored states. Reproduced from [Ode01].

nucleus. An elegant experiment to observe the trend of change of the quadrupole moment of the two lowest superdeformed bands in ^{163}Lu is reported in [Gor04]. The gradual change is interpreted as the increasing of triaxiality with spin, which is also predicted by the particle-rotor model. Such a shape evolution accompanies the triaxial shape, and it proves helpful for its identification. Bands that are interpreted as wobbling excitations have been also presented in ^{161}Lu [Bri05], ^{165}Lu [Sch03], and ^{167}Lu [Amr03].

The Ultimate Cranker ("UC") code provides an alternative theoretical description of the shape of the nucleus at high spin. In essence it is similar to the TRS calculations, though employing the spin as a canonical variable rather than rotational frequency. Apart from the particle-rotor model, UC is oriented towards following the evolution of multi-quasiparticle configurations. Such a task is not trivial and though the UC code performs well in the Lu case, it apparently meets some discrepancies when applied to heavier nuclei (further discussion is in Section 4.3). Previous Ultimate Cranker calculations [Ben89, Ben90] correctly predicted a TSD minimum in the total energy surface ("TES") of the Lu nuclei. They also suggest deep TSD minima for the neighboring ^{164,166}Hf nuclei, however no TSD bands were observed [Jen00]. Recent investigations of the problem has been done by Bengtsson and Ryde [Ben04]. Following the rich experimental material, it is evident that the role of the orbital placement and the actual size of the energy gaps at TSD shapes and their extension with nucleon number has proven to be crucial in obtaining qualitative predictions.

Candidate TSD bands in the Hf region have been first reported in ^{168}Hf [Amr01]. The second Hf nucleus found to exhibit strongly deformed shapes was ^{174}Hf, which is studied in this work. Further reports on TSD candidates are on ^{170}Hf [Neu02], ^{171}Hf [WMa05], ^{172}Hf [WMa05], and ^{175}Hf [Cul04]. A more detailed study that involves measurement of the deformation of some of the SD bands found in ^{174}Hf, as well as discussion on the possibility that they are based on triaxial shapes, are presented in Chapter 4.

Chapter 3

Experimental Techniques

3.1 Populating High-Spin States

There is a broad variety of experimental methods for the excitation of nuclear levels. One technique is to populate low lying levels of a daughter nucleus after the radioactive decay of the parent nucleus. This is often the manner in which new nuclei are observed. Coulomb excitation for probing transition matrix elements of low energy states is another method that is now widely used with the rapid development in radioactive beams. In this reaction the energy of the beam is below the Coulomb barrier and thus the excitation is realized through the electromagnetic interaction. However, it does not provide enough energy for excitation of high-spin states.

In order for one to achieve population of high-spin states, reactions that provide large angular momentum are required. Reactions using heavy-ion collisions along with consequent neutron evaporation from the compound nucleus have proven to be the most effective. The energy of the beam is chosen so that it produces a maximum cross-section for the channel of interest. The projectile nuclei bombard a target of another nucleus and they undergo complete fusion forming a compound nucleus. An estimate of the maximum angular momentum involved in the collision, assuming that the nuclei are charged spheres, can be written as

$$l_{max} = r_{min} \left\{ \frac{2\mu}{\hbar^2} \left[E_{c.m.} - V(r_{min}) \right] \right\}^{1/2}, \tag{3.1}$$

where $E_{c.m.}$ is the energy in the center of mass, μ is the reduced mass, and r_{min} is the distance between the two ions at which the classical turning point of the Coulomb potential V occurs at a given $E_{c.m.}$. The potential has the classical form

$$V(r) = \frac{Z_1 Z_2 e^2}{r}. \tag{3.2}$$

A more sophisticated approach is to include additional attraction from the nuclear force, as a gradient of the nuclear potential on the surface of the spheres. This nuclear force would then compete with both the Coulomb and centrifugal forces.

Reactions of such type can achieve population of states with spin up to $60-80\,\hbar$. Beyond this limit, fission dominates, which creates a broad range of nuclei, such that their γ rays are difficult to assign to individual isotopes.

A schematic description of the fusion-evaporation process is shown in Fig. 3.1. A large amount of the reaction energy is distributed among all nucleons. This is referred to as a "hot nucleus". At this stage, the nuclear wave function does not form a coherent state; rather a significant contribution from "thermal", uncorrelated motion of the single nucleons takes place. The thermal motion opens channels for particle emission, depending on the single-particle separation energy at that temperature. Most often these are neutrons and protons (heavier particles might also be emitted but with much less probability), which are emitted isotropically. This process is essential for removing a large amount of energy ($\sim 1-2\,\mathrm{MeV}$ plus the separation energy) while carrying away a very small portion of angular momentum (approximately $1\,\hbar$). The latter mechanism forces the nucleus to form a coherent state carrying a large angular momentum.

The emission of particles carries important experimental information. The accurate assignment of discrete transitions to a particular nuclide depends on its proper identification. Charged-particle emission, for example, is essentially a rapid drift of the nuclide along the nuclear chart. The detection of the charged particle and tagging it with the γ rays in coincidence is a crucial procedure helping to observe transitions from very weak channels. In experiments using inverse kinematics (i.e., the target nucleus is lighter than the projectile) and Coulomb excitation reactions, the target nucleus can be used as a clean trigger for the reaction. In the case of very low statistics, this technique is the tool of choice for the today's facilities working with radioactive beams.

In high-statistics experiments, such as ones using a fusion-evaporation reaction, the multiplicity of the emitted γ rays is high enough to provide clean identification of the nucleus. Multiplicity is defined as the total number of quanta being radiated per single reaction before the nucleus of interest reaches its ground-state. Providing a maximum spin population of $60-80\,\hbar$ and assuming that the majority of the transitions have a quadrupole character (see below), it can be estimated that about $30-40\,\gamma$ rays are being emitted per reaction. Ideally, those γ rays would constitute the maximum possible information collected from a single nucleus. In practice, observing all transitions from a single reaction

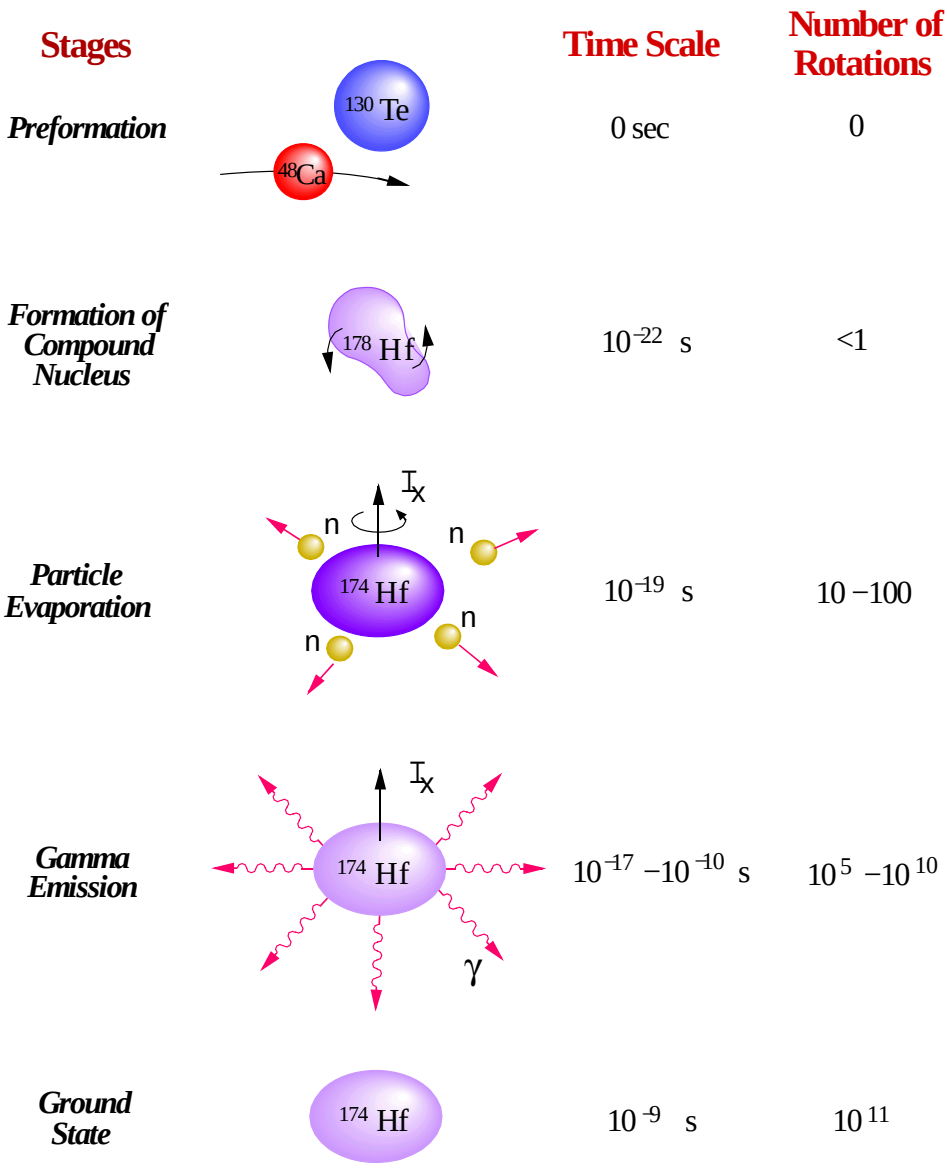


Figure 3.1: An illustration of the fusion-evaporation process and its time scale. Taken from [Lai00].

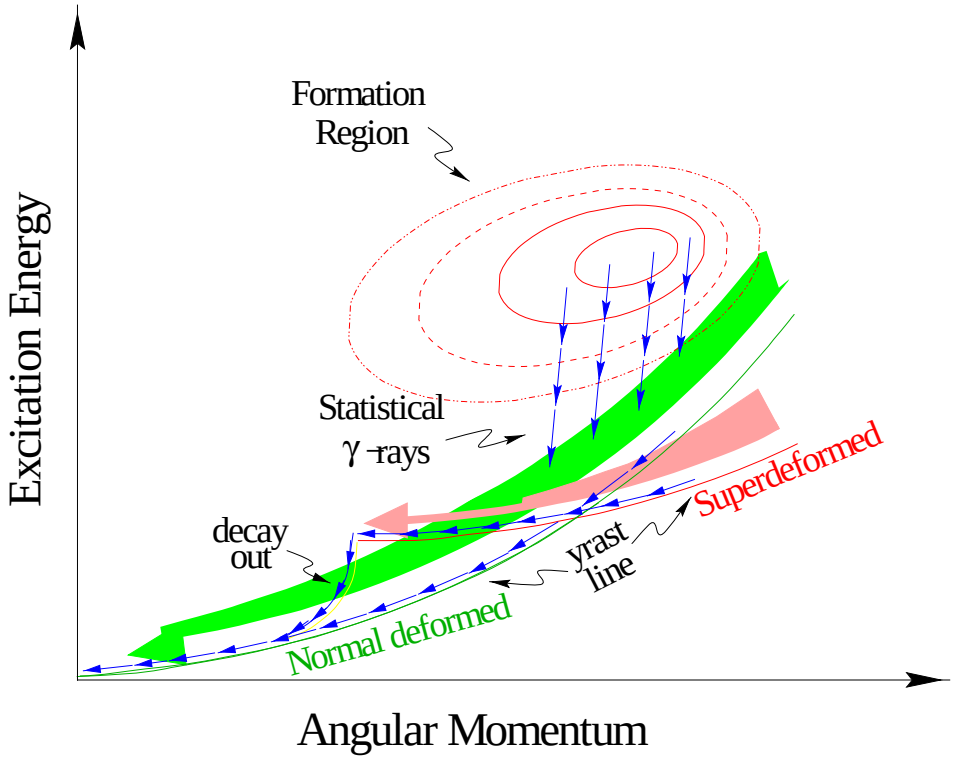


Figure 3.2: The de-excitation path of the nucleus in fusion-evaporation reaction. Reproduced from [Lai00].

is improbable, due to the limited spatial coverage provided by the detectors. We will discuss those issues in detail in Section 3.3.

States populated after the last particle is emitted mark the "entry region." The emission of particles occurs quickly (10^{-19} s) and when the channels of particle emission are closed, further de-excitation of the nucleus is possible only through radiation. The excitation energy, however, at the entry region is still high and the density of states available is enormous. Due to the extremely large overlap of the wave functions of the different states, the radiation emitted by transitions between those states has a statistical nature, i.e., it exhibits an energy distribution. The multipolarity of the radiation is predominantly of $E1$ type and thus it also does not remove a large amount of angular momentum. Once the nucleus is within ~ 3 MeV of the yrast line (that is, the lowest energy the nucleus possesses at a given spin), the density of states decreases significantly. This is the region where discrete structures of the nucleus can be observed (Fig. 3.2). The γ rays have predominantly stretched quadrupole character. The radiation is emitted by transitions between many collective rotational states. In principle, following a sequence of such transitions, one could

identify the underlying configuration and shape of the nucleus (see Chapter 2.3). In practice, the high concentration of bands makes this task impossible. This is the reason such transitions are also considered as part of the statistical radiation, referred as the "quasi-continuum". Such radiation is observed experimentally as an unresolved "$E2$-bump" in the region of $500 - 1500\,\mathrm{keV}$. After the quasi-continuum, the nucleus is cold enough to have discrete transitions ("prompt γ rays"). The observed rotational bands can be traced along the yrast line down to the ground state and it becomes possible for the mutual correlations of the collected γ rays to be studied. This is the primary experimental observation. Discussion of the analysis of γ rays will be presented in Sections 3.3 and 3.5.

3.2 Reaction Selection

The choice of a reaction most suitable for producing the nucleus of interest is related to numerous variables that affect the output of the experiment.

First, a proper choice of target and projectile nuclei has to be made for the compound nucleus to reach the nuclide of interest via particle evaporation. The choice has to take into account the beams that the experimental facility can provide. The available beam energy and intensity have to be sufficient for a detectable yield in order to reach the observation goal of the experiment. The cross sections for producing a compound nucleus are very sensitive to the energy, thus posing a further restriction on the beam energy selection.

The target itself has to satisfy multiple requirements. Its thickness (measured in $\mathrm{mg/cm^2}$ or $\mu\mathrm{g/cm^2}$) is the main characteristic that can be varied for different purposes. In practice it is important to take into account the advantages and disadvantages for both thick and thin targets.

For a thin target ($\sim 0.5\,\mathrm{mg/cm^2}$), the yield might be decreased due to the lower number of target nuclei that the beam projectiles encounter. The thin layer of material does not slow the compound nuclei ("recoils"), which introduces a significant Doppler shift in the energy of the prompt γ rays. Although the latter effect is common, it is not a major concern due to the fact that the velocity of the recoil can be well estimated from momentum conservation arguments (see Section 3.6.1, Eqn. 3.6) and thus one can correct the energy of the emitted γ rays.

The target has to be highly pure ($\sim 95\%$) with the isotope of interest, otherwise many other unwanted nuclei would be produced. A thin layer of covering material ("flashing") can be added for preventing the target from oxidation (usually gold). Its choice must be conformable to the beam energy so that the Coulomb barrier of the layer is higher than the energy of the projectile. In case the projectile interacts with the flashing, the number

of excited levels is low and therefore they do not contribute significantly to the overall spectrum.

In this work one of the experiments was performed using a backed target. The target consists of three layers - flashing, target layer and backing. The backing has thickness of order of tenths mg/cm^2. This in general provides an effective stopping of the recoils which is desirable in some cases. We will discuss more on this topic in Section 3.6.1.

3.3 Detection of γ Rays

In high-spin nuclear spectroscopy the primary carrier of experimental information is the set of γ rays emitted after the quasi-continuum stage of producing the nucleus. Depending on the goals of the experiment (high-spin studies, lifetime measurements, calorimetry, etc.), the radiation can be examined with a large variety of experimental setups.

The high-purity germanium (HpGe) detector is an established tool for studying nuclear phenomena. It is a semi-conductor with small energy gap ($\sim 0.7\,$eV) that allows the γ ray to easily create electron-hole pairs in the volume of the crystal, on average 2.9 eV per pair. The energy of the γ ray is directly proportional to the number of charge carriers collected from the active volume of the detector. The small value of the energy gap assures a high energy resolution, with full width at half maximum (FWHM) for HpGe of about 2.2 keV at 1.33 MeV.

There are three possible interactions of the γ rays with the detector crystal: the photoelectric effect, Compton scattering, and pair production (Fig. 3.3). In case of the photoelectric effect, which is dominant below 150 keV, the entire energy of the γ quantum is absorbed in the crystal. The produced charge entirely represents the energy of the quantum and thus belongs to the photo peak of the corresponding transition that is being measured.

Compton scattering is dominant in the energy interval $150\,\text{keV} - 5000\,\text{keV}$, which unfortunately is the region where most of the interesting nuclear phenomena are observed. When Compton scattered, the γ ray deposits only part of its energy in the crystal. After the first scattering, the resultant γ ray can still be absorbed within the same crystal, which will produce the correct γ-ray energy. In the worst case, the γ ray might leave the crystal. This will produce a continuous function of the energy distribution (Compton background), which is not desirable. Special techniques to suppress this background are developed and are in common use today (see Sections 3.4 and 3.5).

The production of an electron-positron pair is possible if the energy of the γ ray is above the threshold for creating two electron masses (1022 keV) and it becomes dominant above 5 MeV. In case those particles escape from the crystal, the registered energy would be the

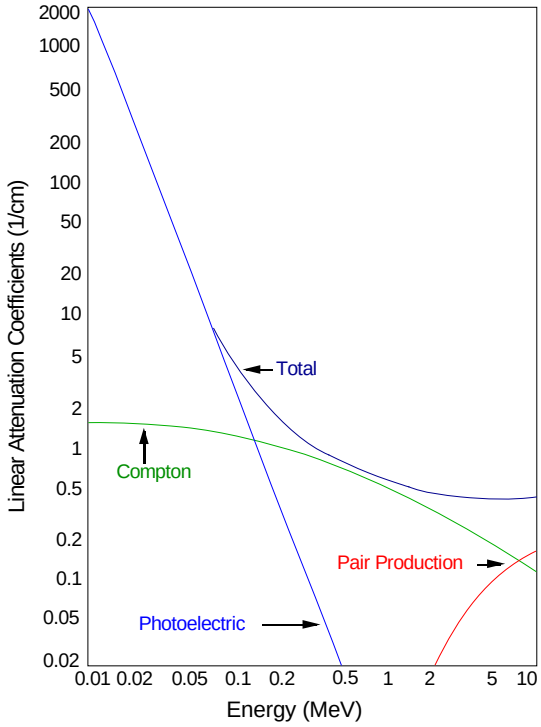


Figure 3.3: The energy dependence of the relative strength of the processes that occur in Ge crystal.

difference of the γ ray energy and the energy of the escaped particle. This also adds to the background.

3.4 Gammasphere

The results in this dissertation were initially obtained from experiments performed at the GAMMASPHERE array [Lee90], currently located at the Argonne National Laboratory [w3GS]. GAMMASPHERE is a device from the family of the Large Array Escape Suppressed Spectrometers (ESS). The ESS array is a multi-detector device which provides today's best relative intensity threshold down to 10^{-5} of the total reaction cross section. The detectors have large volume HpGe crystals for high energy resolution and efficiency. Fig. 3.4 shows a typical construction of the spectrometer. The detectors are surrounded with bismuth germanate ($Bi_4Ge_3O_{12}$, abbreviated as BGO) scintillators. The BGO detectors fully occupy the space between the Ge detectors, which increases the total efficiency of the array with respect to scattered γ rays (see Fig. 3.4), mentioned in the previous Section. The BGO detector provides a *veto* signal when the scattered γ ray has deposited energy in both BGO and



Figure 3.4: A typical construction of a Compton-suppressed detector array. The BGO shield is shown as well as the crystal of the Ge detectors. The veto signal in the case of an escaped γ ray provides a significant improvement of the peak-to-total ratio.

Ge detectors. This provides a high suppression of detection signals coming from escaped γ rays mentioned in the previous Section. This significantly improves the peak-to-total ratio (P/T), which is defined as the ratio of the area of the photo peak to the total area of the spectrum for a single γ ray detected by the spectrometer. If no veto signal has been received within a certain time window (typically $1\,\mu$s), the γ rays registered by the Ge detectors form an "event", which is then stored on media for an offline analysis.

The GAMMASPHERE is currently the most advanced ESS device. Some of its characteristics are given in Table 3.1. The peak-to-total ratio is about 60 %. The germanium crystals provide 46 % coverage of 4π solid angle. The mechanical system is composed of two hemispheres as a supporting body of the detectors (Fig. 3.5). The hemispheres can move apart transversely to the beam line to provide access to the target chamber as well as rotate about their axis for detector handling.

Recently, a new generation of detector arrays based on γ-ray tracking is being developed, such as GRETA [Del99] in the US and AGATA [Lie01] in Europe. The novel concept

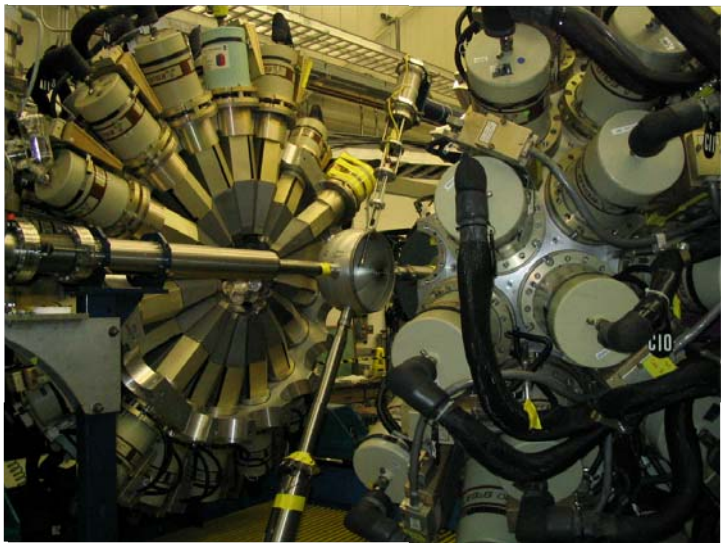


Figure 3.5: View of the GAMMASPHERE with the hemispheres open. In its center, additional auxiliary devices can be used.

Table 3.1: Characteristics of GAMMASPHERE.

Number of detectors	110 40 unsegmented 70 segmented
Ge detector size	7.1 cm (D) $\times$ 8 cm (L)
Target to Ge distance	25.25 cm
Total Ge solid angle	46% of π
Total peak efficiency (1.33 MeV)	9.9%
P/T (1.33 MeV)	0.6
Energy resolution	2.5 keV (FWHM)

employed in those devices is to track the scattered γ rays in highly segmented germanium crystals. Since the probability for escaping is much smaller (it decreases rapidly after each scattering due to geometrical factors), the entire information for the incoming γ ray is "preserved" in the crystal. The technical and scientific challenge is to restore this information from the shape of the signals that the different segments return, as well as to deal with multiple coincidences and reconstruction of the true trajectories of the γ rays. The projected resolving power of those devices is expected to be at least three orders of magnitude better than that of the GAMMASPHERE. Currently very active research in the field is underway [w3GR, w3AG].

3.5 Data Analysis

We will briefly discuss the methods of analyzing data obtained from nuclear structure experiments. The interface of GAMMASPHERE allows for the recording of information in stream format returned from the the firing detectors. The main piece of recorded data is the *event*, mentioned in the previous Section, which forms the basic logical structure that carries information about the emitted γ rays. The event consists of a given number (*fold*) of records of individual γ rays, storing information about energy, as well as auxiliary information such as detector identification, time, and specific information if the detector was segmented.

For the purpose of the analysis, an event can be considered as a set of numbers, which most often are taken to be the energies of the γ rays. Such a multiple naturally defines a point in a multi-dimensional space. This provides a convenient way of representing the coincidence relationships between the γ rays. Common correlation structures that are used today are matrices, cubes and cubes with four axes (*hyper cubes*). The axes represent the energy ranges of the γ rays and their cells are incremented by one count each time there is an event of the corresponding fold (2, 3, and 4 for matrices, cubes, and hypercubes, respectively).

In the modern multidetector arrays a typical range of registered folds is from 1 to 9. In order to increment a correlation structure the fold must be higher or equal to the number of axes. For example, an event of fold 2 cannot be stored into a cube. In the case when the fold f is greater than 3 (cubes for example), it is necessary that the event is decomposed (*unfolded*) into $\binom{f}{3}$ events of fold 3. The latter is true for all dimensions of correlation structures. Such unfolding should be done only once, since a second unfolding would introduce artificial correlations which would produce "spikes" [Bea95] in the spectra that can be misleading.

As mentioned in Section 3.1, the γ rays that belong to the same event would probably emerge from the same cascade of a rotational band. It is possible, however, that not all of the detected γ rays would be in true relationship or not all of them are fully absorbed into the volume of the detectors. These transitions belong to the background, which can have a complex nature.

The background consists of γ rays (both from the continuum and discrete transitions) coming from various sources, such as residual nuclei in the target, as well as γ rays coming from the natural radiation background. Considering that in a single reaction multiple γ rays are emitted, the exact distribution of the background is impossible to be derived. In a given event there is always a probability γ rays from the background are present.

However, there are methods that estimate this background and subtract it from the coincident γ-ray spectra. The traditional way is to gate on areas that lie close to the peak of interest, providing there are no peaks present there. The returned gated spectrum is considered to represent the background, which in turn is subtracted from the spectrum produced by gating on the peak itself. However, with the gradually increasing resolving power of the modern arrays, such areas often are not available. Todays methods exploit the availability of larger correlation structures as they can estimate the smooth component under the peaks. Originally, such estimation for matrices was proposed by Palmetta and Waddington [Pal85]. The method relies on the fact that in high-statistics experiments the Compton background is dominant with respect to the natural radiation background. It was noted that the shape of the background is proportional to the smooth component in the total projection of the matrix, which can be conveniently estimated by simply drawing a continuous line under the peaks with the restriction that the line to be close to the spectrum within the statistical uncertainty. The sum of spectra slices, corresponding to the regions when the smooth line is close to the total projection, is used as a universal background estimation for the matrix.

Extension of this method to higher dimension structures is performed by Radford [Rad95a]. Efforts toward automatic estimation of the levels of the background were done by Crowell *et al.* [Crw95]. The latter method employs a statistical χ^2 test for the estimation of the level of background in dimensions higher than two (mostly cubes). Its main advantage is that it removes the subjective element in estimating the background.

Both methods are applicable in the case when the axes of the structures are equivalent (*symmetric*). However, an inconvenience emerges when the goal is to perform angular correlations when the axis denotes energies at a *given* angle. It becomes necessary for multiple matrices or cubes to be generated for each angle, which might become cumbersome.

Recent development of a method for background subtraction in the case of angular de-

pendence of the energies was done by Starosta *et al.* [Sta03]. That method, along with a special structure for storing events called the BLUE database (see Section 3.6), were utilized in the analysis of the data from the second experiment on superdeformed bands in ^{174}Hf. A specific feature of the events stored in a BLUE database is that they can be extracted on an event-by-event basis, thus allowing one dimensional spectra to be produced. The background subtraction method is based on the elegant observation that a spectrum obtained from gating on two energies contains in its background several classes of γ rays: each of them could come from either the real peak or from the background. This can be expressed using a normalized relation

$$pp + bp + pb + bb = 1,$$

where p and b denote peak and background fraction event numbers. They can also be deemed as probabilities for the γ rays to originate from peak or background. The method produces spectra that remove all of the terms in this equation except the pp. Spectra produced by gating on double and single γ rays are used. In these, peak and background counts coming from the other γ rays of interest are contained. Their background-to-total ratio can be deduced automatically. An assumption that the peak and background are not correlated is also used. The method is free from the requirement of having static cubes and is perfectly suited for use with the Doppler Shift Attenuation Method and angular correlation analysis.

3.6 Analysis Programs and Databases

The analysis of the bands in ^{174}Hf at high spin was performed using the program package RADWARE [Rad95]. The high statistics data were sorted into a hypercube which enabled a thorough investigation of the coincidence dependence of the γ rays. The RADWARE package provides a convenient way of taking gates, producing spectra, and displaying level schemes as well as fitting intensities. Level schemes could be easily checked against hypotheses for placement of γ rays, thus very efficiently building the most reliable level scheme.

As mentioned in the previous Section, a database called BLUE [Cro01] was used, which helped in determining the angle dependence of the energies of the γ rays. Matrices and cubes store counts for each event, but additional information (detection angle) is lost in this method. However, this information is necessary when determining lifetime of a state and angular correlation. Static structures also have the disadvantage that they use a large amount of disk space that contains very few counts. For a large energy range, the wasteful use of disk space becomes unacceptable.

To overcome these problems, the BLUE database was designed in a way that stores the

events in their native format along with their auxiliary information. For each native fold, the computer code creates separate files in which only the events of the corresponding fold are stored one by one. The advantage of this database is that the events are stored not in the order they arrive from the tape, but rather they are associated with a logical search structure, namely a binary tree. Thus events close in energy lie physically close in the computer file. This is very important since when taking a gate only a small portion of the file is searched for matching events. For comparison, the entire dataset must be sorted every time when a static cube or matrix needs to be created. The BLUE database is created only once, which later enables the extraction of events for building cubes if necessary.

Because of the preservation of the auxiliary information, a BLUE database proved to be an essential tool. For the needs of our analysis, not only is the γ-ray energy recorded, but also the angle with respect to the beam for each γ ray is kept in the database. Gates employing both variables were used in extracting the spectra of interest.

Since the BLUE database stores events without unfolding them, it was necessary to find a way of taking gates on an event by event basis. Note that such gating is different in implementation than the procedure of examining cubes due to the fact that the number of gating conditions (energy, angle, time, etc.) can be larger, and the gating has to be done at once for a given event. Such a routine was developed for the analysis of the data in this work. The routine takes special care of repetitions of energies from the gates of interest, because of the finite width of the gate. We find it useful to show in detail how it can be programmed. The routine, implemented in C programming language for the case of gating on two energies is presented below for maximum fold of 9.

```
(1) marked[0]=0;marked[1]=0;
    for(i=0;i<9;i++)
    {
     GammaHit0[i]=0;GammaHit1[i]=0;
    }
(2) for (i = 0; i <= (mult-1) ; i++)
      {
       if (gateScheme[id[i]-1][ener[i]][0]==1)
        {
          GammaHit0[marked[0]]=i;
          marked[0]++;
        }
       if (gateScheme[id[i]-1][ener[i]][1]==1)
        {
```

```
          GammaHit1[marked[1]]=i;
          marked[1]++;
        }
      }

(3) for(Gcounter[0]=0; Gcounter[0]<marked[0]; Gcounter[0]++)
    {
     for(Gcounter[1]=0; Gcounter[1]<marked[1]; Gcounter[1]++)
      {
       for(n=0; n < mult; n++)
        {
         if((n!=GammaHit0[Gcounter[0]]) && (n!=GammaHit1[Gcounter[1]]))
          {
           histogram[id[n]-1][ener[n]]++;
          }
        }
      }
    }
```

Part (1) initializes the arrays. In (2) the variables marked are counters for how many energies of the two gates are present in the event of fold *mult*. The variables GammaHit[] store the number of the γ rays from the event, that have satisfied the energy-angle gating condition gateScheme[*angle*][*energy*]. In (3) the variables Gcounter[] run through the marked γ rays from both gates, always two at a time, leaving the others (including energies that might also belong to the gate) available for incrementing the spectrum array histogram[*angle*][*energy*]. This ensures that spectra resulting from all possible combinations of a given energy gate are taken into account. This is necessary, since there is no way to choose which γ ray in the gate has actually come from the rotational band. The routine also avoids any unfolding of the event, thus guarantees a spikeless spectrum. The final result is a collection of spectra of energies at all available angles. They can consequently be used for examining Doppler shifts and angular dependence intensities.

3.6.1 The Doppler Shift Attenuation Method

In this Section we will discuss in detail the techniques and the physics behind lifetime measurements of the excited levels as they undergo an electromagnetic decay. Lifetimes provide essential information as they are directly related to the transition probabilities. Together with the energy levels, transition probabilities are a desirable output from any

nuclear model, as a correct reproduction of lifetimes would imply a good insight on the character of the wave function of the state of interest.

The theoretical understanding of transition probabilities involves a coupling of the electromagnetic field with the currents that are associated with the nucleons, both in single-particle and collective modes. A full treatment of the nuclear system would require an addition of the electromagnetic potential $\vec{A}$ to the nuclear Hamiltonian. In a simple picture, the wave function of the nuclear system would be influenced by $\vec{A}$ which in turn would affect the electromagnetic field as well. It is clear that a rigorous treatment of such a system would be possible only in limited cases when approximations allow an explicit calculation of the matrix elements of the electromagnetic operators and the internal nuclear states.

In the high-spin regime the nucleus can be regarded in a semi-classical way as spin projection on the x axis, and I_x becomes a good quantum number. The corresponding Clebsch-Gordan coefficients for $E2$ transition probabilities (see Eqn. 3.14) become constant at high-spin which is an additional convenience. In our work, we have investigated the transition probabilities of $E2$ transitions only, in connection with transitions in superdeformed bands. The model that has been used is a quantum rigid rotor coupled with quadrupole electromagnetic radiation.

We will continue with the discussion of the experimental details on measuring lifetimes, closely following Alexander and Forster [Ale78]. Nuclear lifetimes induced by any nuclear process have a very broad range, from 10^{-23} s to billions of years. Naturally, the measurement methods also can be quite different. In the specific case of electromagnetic transitions, the lifetimes range from femtoseconds (for very fast transitions within superdeformed bands) to days (for isomers). In this work we have investigated the lifetimes of superdeformed bands.

Two suitable experimental methods for probing short lifetimes of electromagnetic transitions are the *plunger* method and the Doppler Shift Attenuation Method ("DSAM"). They both are based on the angular dependence of the energy of the γ rays on the velocity of the emitting nucleus. Those so-called *recoil-distance* methods can have many implementation modifications and we will emphasize the principles involved (Fig. 3.6).

The plunger method uses the detection of the γ rays as they are emitted by the nucleus in free flight at a given distance from the target. The nucleus is consequently brought to rest in a thick stopper (*plunger*). In case of a longer lifetime, emitting radiation after it has stopped is possible. The produced spectra have the characteristic double peaks corresponding to the moving and the stopped component (See Fig 3.6). The number of decaying nuclei for the time of flight t_F is

$$I_s = \int_0^{t_F} -\frac{dN}{dt} dt = N_0(1 - e^{-\lambda t_F}), \tag{3.3}$$

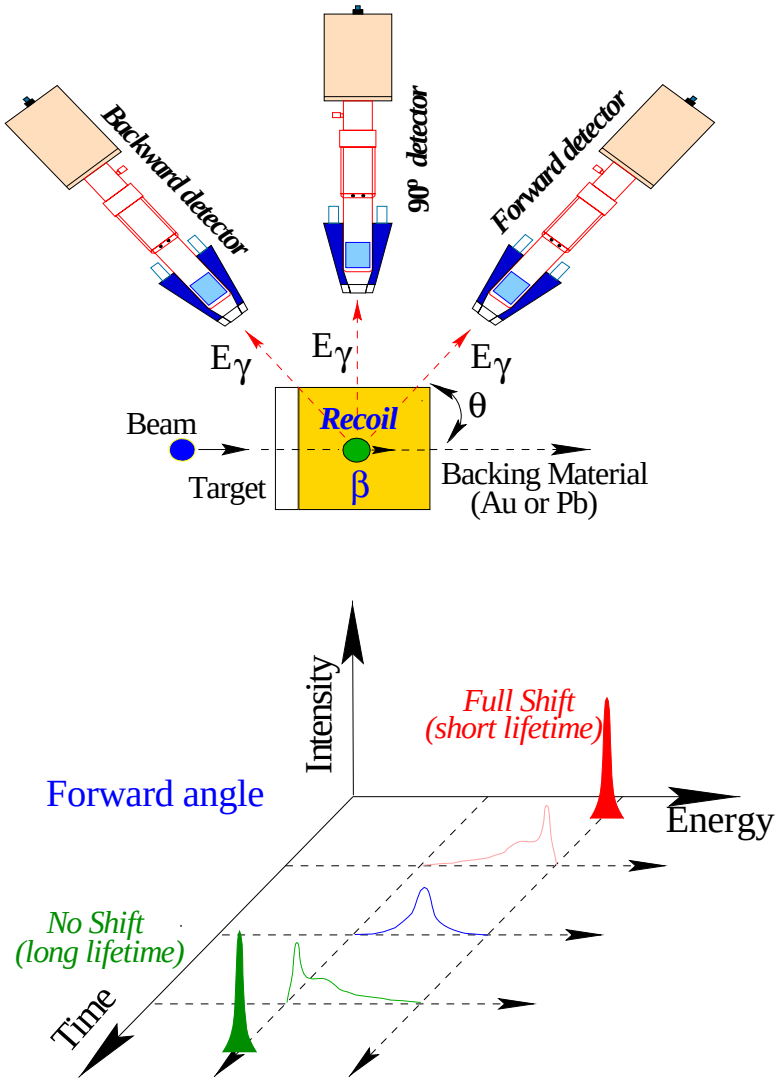


Figure 3.6: The Doppler shift effect for a single γ-ray transition as a function of its lifetime and velocity of the recoil that is being slowed down in a medium (stopper). In case of long lifetime τ, there is only a stopped component present in the peak. For shorter lifetimes, the fraction of the γ rays that are emitted in flight becomes dominant. Reproduced from [Lai00].

and those decaying in the plunger

$$I_0 = N_0 e^{-\lambda t_F}. \tag{3.4}$$

If the plunger is at distance D from the target, the fraction of the nuclei surviving as a function of D is

$$\frac{I_0}{I_0 + I_s} = e^{-\lambda t_F}, \tag{3.5}$$

where $t_F = D/v$. Eqn. 3.4 gives directly the lifetime $\tau = \lambda^{-1}$ when plotted as a function of D.

The plunger method is convenient to work with as it provides a direct information about the lifetime τ. However, there are certain limitations on its use in the case of lifetimes comparable with the stopping time in the plunger. Effects that must be taken into consideration are the energy and direction spread of the recoils. This is related to the target as its thickness choice governs the mutually exclusive production yield and spatial spread. There are also numerous energy levels that are both above and below the level of interest. In this case a complicated balance of the intensities of the different levels has to be performed (generally based on the so-called Bateman equations). An additional difficulty comes from the natural angular distribution of the radiation. The latter effect can be controlled to some extent by placing detectors at angles at which the intensities of given radiation multipolarity ($E1$ or $E2$) are minimal.

The Doppler Shift Attenuation method is used for measuring lifetimes shorter than the sensitivity of the plunger method. These time ranges are of the same order of magnitude as the stopping time of the nuclei in the plunger. The idea of the method is to reduce the free flight distance to zero, forcing the nuclei to enter the stopper immediately after they have been produced. Then the Doppler shift would be directly related to the decreasing character of the velocity of the ion in the stopper. The parameters that govern such a process are the so-called *stopping powers*. They represent the energy loss of the ion at a unit distance. The stopping powers have two distinct components, namely nuclear and electronic. The nuclear stopping mechanism is the dominant one at low energies ($\beta = v/c < 0.5\%$). For the intermediate velocity range $\beta \sim 0.5 - 2\%$ the contribution from nuclear and electronic stopping powers is comparable, and for $\beta > 2\%$ the stopping power is dominated by the electronic stopping. For both low- and middle-range velocities the stopping powers cannot be measured accurately due to the increased difficulties gathering the experimental data. It is a common practice for these velocity regimes to be modeled theoretically. As an example one can point to the theory developed by Lindhard *et al.* [Lin63] and later refined by Blaugrund [Bla66]. The electronic stopping is assumed to have long-range collisions, small energy transfers, and small angle deflections. The nuclear stopping, on the contrary,

has a large energy transfer and angle scattering. Ironically, stopping powers are crucial to determining the stopping of the ion in DSAM, and yet they cannot be calculated in a rigorous way. Modeling of stopping powers is a specific area of study with applications to many fields, including ones outside physics. In this work we have adopted the results from the program SRIM 2003 [w3SR] by Ziegler [Zie85] for modeling of stopping of heavy ions.

In a reaction with heavy ions, the initial velocity of the compound nucleus can be determined from simple kinematics,

$$\beta_0 = \frac{1}{A_{\text{beam}} + A_{\text{target}}} \left(\frac{2 A_{\text{beam}} E_{\text{mid-target}}}{931.5} \right)^{1/2}, \tag{3.6}$$

where $E_{\text{mid-target}}$ is in MeV. The energy is defined at the middle target since it is not possible to obtain control over the position of formation of the compound nucleus. From that point of view, β_0 is a *defined* quantity. The energy loss of the beam is taken into consideration as the beam ions travel to the center of the target with thickness L before they undergo a reaction,

$$E_{\text{mid-target}} = E_{\text{beam}} - E_{\text{loss}} = E_{\text{beam}} - \left(\frac{dE}{dx} \right)_{\text{tot}} \times \frac{L}{2}, \tag{3.7}$$

where dE/dx is the energy loss (stopping power) of the beam ion before it reaches the middle of the target. The stopping power is a sum of both the electronic and nuclear stopping powers.

The process of slowing down the recoils affects the observed shape of the emitted line. Depending on the lifetime of each particular level, the energy of the emitted γ ray will depend not only on the angle at which it is observed, but also on the moment of time it is observed. That is, there exists a velocity distribution of the recoils, $P(v, t)$. This was estimated using the code SRIM 2003 [Zie85]. The code returned the electronic and nuclear stopping powers which were used in the code FITFTAU [Moo97] to estimate the transition quadrupole moment.

Since each level has an averaged moment in time at which the level de-excites, there will be a peak in the distribution of the γ-ray line. This peak coincides with the centroid of the peak, in the case of very fast transitions. Thus the average velocity of the recoil at which a level undergoes a transition carries information about its lifetime. Experimentally, the value of

$$F(\tau) = \frac{\bar{\beta}}{\beta_0} = \frac{E(\theta) - E_0}{E_0 \beta_0 \cos(\theta)}, \tag{3.8}$$

is observed, where θ is the angle with respect to the beam axis, $E(\theta)$ is the position of the centroid of the peak at that angle, E_0 is the unshifted energy (which can be observed at 90°). The $F(\tau)$ value is naturally connected to the lifetime τ of each level through a

convolution with the velocity and sidefeeding distribution. The latter can be tackled only by modeling via the observed differences in intensity for each of the transitions in the band. For each level, a cascade of side transitions will feed into it, satisfying

$$\frac{dN_k(t)}{dt} = \lambda_{k-1}N_{k-1}(t) - \lambda_k N_k(t), \quad k = 1, 2...n \tag{3.9}$$

where $N_k(t)$ is the population of the k$^{\text{th}}$ sidefeeding level. The solution of Eqn. 3.9 gives the Bateman equations

$$N_k(t) = N_0 \prod_{i=1}^{n-1} \lambda_i \sum_{j=1}^{n} \frac{e^{-\lambda_j t}}{\prod_{l\neq j}^{n}(\lambda_l - \lambda_j)}, \quad k = 1, 2...n, \tag{3.10}$$

which is the solution for each of the levels that contribute to the sidefeeding. Then the $F(\tau)$ value can be written as

$$F(\tau)_p = \frac{1}{N_0\beta_0}\int_0^\infty N_p(t)\beta(t), \tag{3.11}$$

where $N_p(t)$ is the population of the p$^{\text{th}}$ level in the cascade of interest, for which an expression of the type Eqn. 3.10 also holds.

The lifetimes are described by a model formula [Rin00], assuming a pure $E2$ character of the transitions,

$$\tau = \frac{\lambda}{1.22 * 10^9 E_\gamma^5 B(E2)} \text{ s}, \tag{3.12}$$

where E_γ is in MeV and λ is the branching ratio

$$\lambda = \frac{I(E2)}{\sum I_i(1+\alpha_i)}, \tag{3.13}$$

where the sum runs over all of the intensities (corrected for internal conversion) that depopulate the level. The transition probability $B(E2)$ is given by [BoM98]

$$B(E2) = \frac{5}{16\pi}e^2 Q_t^2 \langle I020|I-20\rangle^2, \tag{3.14}$$

$$\langle I020|I-20\rangle^2 = \frac{3I(I-1)}{2(4I^2-1)}. \tag{3.15}$$

The formula that involves experimental quantities thus becomes

$$\tau = \frac{0.822\lambda}{E_\gamma^5 Q_t^2 \langle I020|I-20\rangle^2} \text{ ps}, \tag{3.16}$$

with E_γ measured in MeV and Q_t in electrobarns (1 eb = 100 $e \times$ fm^2).

The code FITFTAU uses Eqn. 3.16 to determine the quadrupole moments of rotational bands. Technically, the target is considered as consisting of multiple layers, in each one of

which the stopping powers are taken as constant (but varying from layer to layer). The velocity profile along the length of the entire target is then estimated. The code uses a range in which the quadrupole moment can vary, and the corresponding $F(\tau)$ curve is calculated, based on the proposed lifetimes and intensity changes in the transitions of interest. The final result is taken to be the curve that minimizes the χ^2 of differences between calculated and experimental values for $F(\tau)$.

In this work, the quadrupole moments of superdeformed bands in ^{174}Hf have been determined. They provided a useful information needed for later discussion on the nature of these bands. More details will be presented in Section 4.2.

Chapter 4

Superdeformation Studies

4.1 Experimental Details and Results

Data from three experiments were used in this work. In the first experiment, GSFMA90, high-spin states in ^{174}Hf were produced with the ^{130}Te(^{48}Ca,4n) reaction at beam energies of 194 MeV and 200 MeV. The target consisted of $\sim 0.5\,\mathrm{mg/cm^2}$ of enriched ^{130}Te covered with a thin ($\sim 0.2\,\mathrm{mg/cm^2}$) Au flashing, and the ^{48}Ca beam was provided by the ATLAS facility at Argonne National Laboratory (ANL). Decay γ radiation was detected with the GAMMASPHERE array, which contained 100 Compton-suppressed Ge detectors. A total of $\sim 5.5 \times 10^8$ three or higher fold coincidence events were recorded in approximately *one day of beam time*. It should be noted that the primary objective of this experiment was to observe rotational levels built on the high-K isomers in ^{174,175}Hf. As these sequences, connected with high-K isomers, may be low in multiplicity, a relatively low trigger condition of only three or more Ge detectors in coincidence was used. Thus, this experiment was not optimized for a search of superdeformed bands as higher multiplicity triggers and longer beam times are normally required. The data were also used to study the high-spin states in normal deformed bands, presented in chapter 5. The beam wobbling device at ANL was utilized so that a higher beam intensity (~ 1.7 pnA) could be deposited on the Te target, which has a relatively low melting point. The transitions were Doppler corrected and then sorted into a coincidence cube. Subsequent analysis of this cube was accomplished using the RADWARE package.

The second experiment, GS2K047, was dedicated to measuring the lifetimes and to confirming the large deformation of rotational bands discovered in the first experiment [Djo03]. The same reaction ^{130}Te(^{48}Ca,4n) was used at a beam energy of 200 MeV and beam current of 2 pnA. A self-supporting target was used consisting of a $50\,\mu\mathrm{g/cm^2}$ Au flashing in front of $850\,\mu\mathrm{g/cm^2}$ enriched ^{130}Te evaporated on a $25.6\,\mathrm{mg/cm^2}$ Au backing. The ^{48}Ca beam

was provided by the 88-inch Cyclotron at the Lawrence Berkeley National Laboratory. In total, 102 Compton suppressed detectors of GAMMASPHERE were used. A requirement of at least five prompt coincident γ rays defined an event written to tape. A total of 3.5×10^9 events were collected, and the information was stored into a BLUE database [Cro01].

The third experiment, GSFMA117, was dedicated to searching for linking transitions between superdeformed bands. The reaction ^{130}Te(^{48}Ca,4n) was used but at a beam energy of 205 MeV. The beam was delivered by the ATLAS facility at the Argonne National Laboratory. Four targets, with $\sim 500\,\mu$g/cm^2 of Au in front of the Te and $\sim 80\,\mu$g/cm^2 Au on the back, were mounted onto a rotating target wheel. The pulses of the accelerator beam were synchronized with the rotational frequency of the wheel. The thicknesses of the ^{130}Te ranged from 400 to 600 μg/cm^2. The rotating wheel was used to allow a higher intensity beam to be deployed on target. The maximum sustained beam current was 2.5 pnA. One hundred Ge detectors were used and $\sim 2.6 \times 10^9$ events were collected with at least four γ rays detected in prompt coincidence. Lead attenuators that absorb low energy γ rays and x rays were used in front of each Ge detector. The data were also analyzed using the RADWARE program package. The amount of data was large enough to build a 4-dimensional coincidence cube, which provided a higher level of sensitivity to weak structures.

Data from the GSFMA90 and GSFMA117 experiments revealed eight new rotational bands [Djo03, Har05]. Spectra of the bands are shown in Fig. 4.1 and Fig. 4.2. All of them contain at least ten transitions that span a spin region of 20 $\hbar$. The coincidence relationship with the ground-state band in ^{174}Hf is evident, which assigns the bands uniquely to this nucleus. Fig. 4.3 shows the ground state band of ^{174}Hf up to the highest level (spin 24 $\hbar$) that is observed to be fed by any of the new bands. The marked peaks between the 206 keV and the 311 keV transitions in panel d) (Fig. 4.1) are identified to have energy values close to the $\Delta I = 1$ transitions in the rotational band built on top of the $K = 14^+$ isomer studied recently in ^{174}Hf [Grp94, Har05a]. It can be noted that these transitions are present in the spectra of all the bands. Further investigation showed that these transitions do not originate from a background and thus they can be deemed as genuine [Har05a]. This provides an important insight into the possible nature of the bands which we will discuss further in this chapter.

Two of the bands exhibit cross-linking transitions between each other (bands SD3 and SD6), which results from an accidental degeneracy of their levels (Fig. 4.4). From the same figure a convenient estimate for the relative excitation can be drawn as well. Since the bands have been populated under the same experimental conditions, the decrease in number of observed levels is an illustrative measure for an increase in excitation energy. The spin assignments for all of the bands have been estimated from the assumption that the lowest

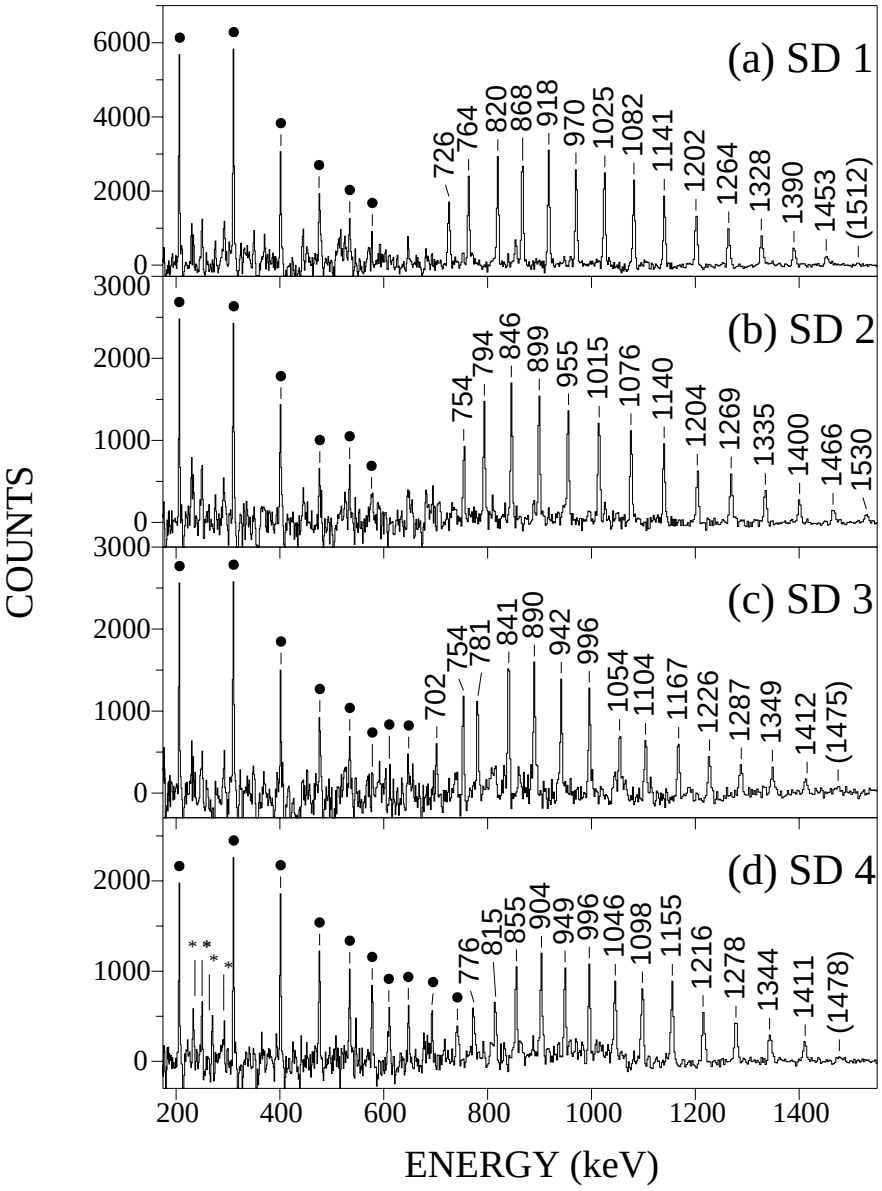


Figure 4.1: SD bands 1-4 in ^{174}Hf. The spectra were generated with all possible in-band triple-gate combinations within the hypercube. Transitions in the ground-state band are denoted by filled circles. The peaks marked with star symbol in panel d) denote $\Delta I = 1$ transitions in a rotational band built on the $K^{\pi} = 14^{+}$ isomer. Panel d) was chosen as one showing the peaks in the most visible way, though they are present in all SD band spectra for ^{174}Hf.

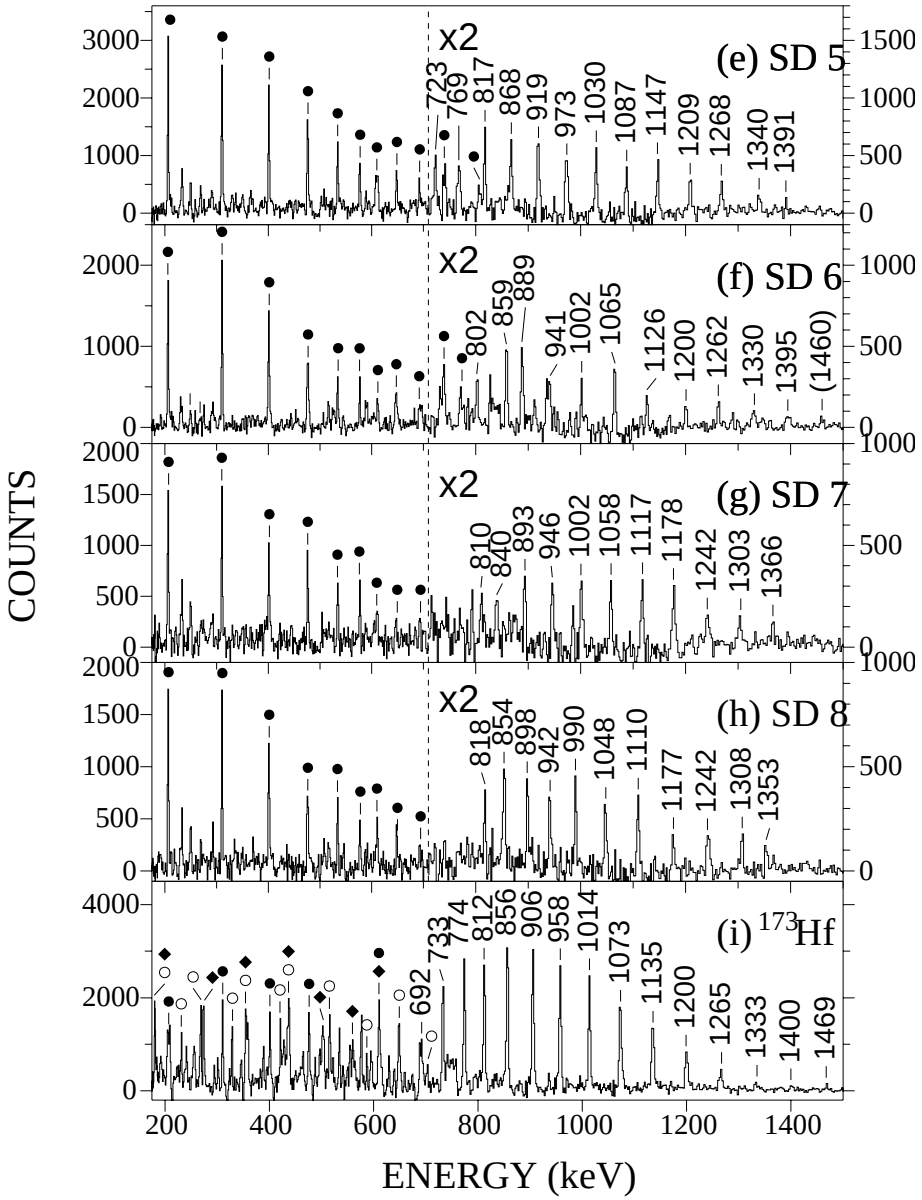


Figure 4.2: SD bands 5-8 in ^{174}Hf and the newly discovered SD band in ^{173}Hf [Har05]. The spectra were generated with all possible in-band triple-gate combinations within the hypercube. To the right of the dashed line the scale has been reduced by a factor of two.

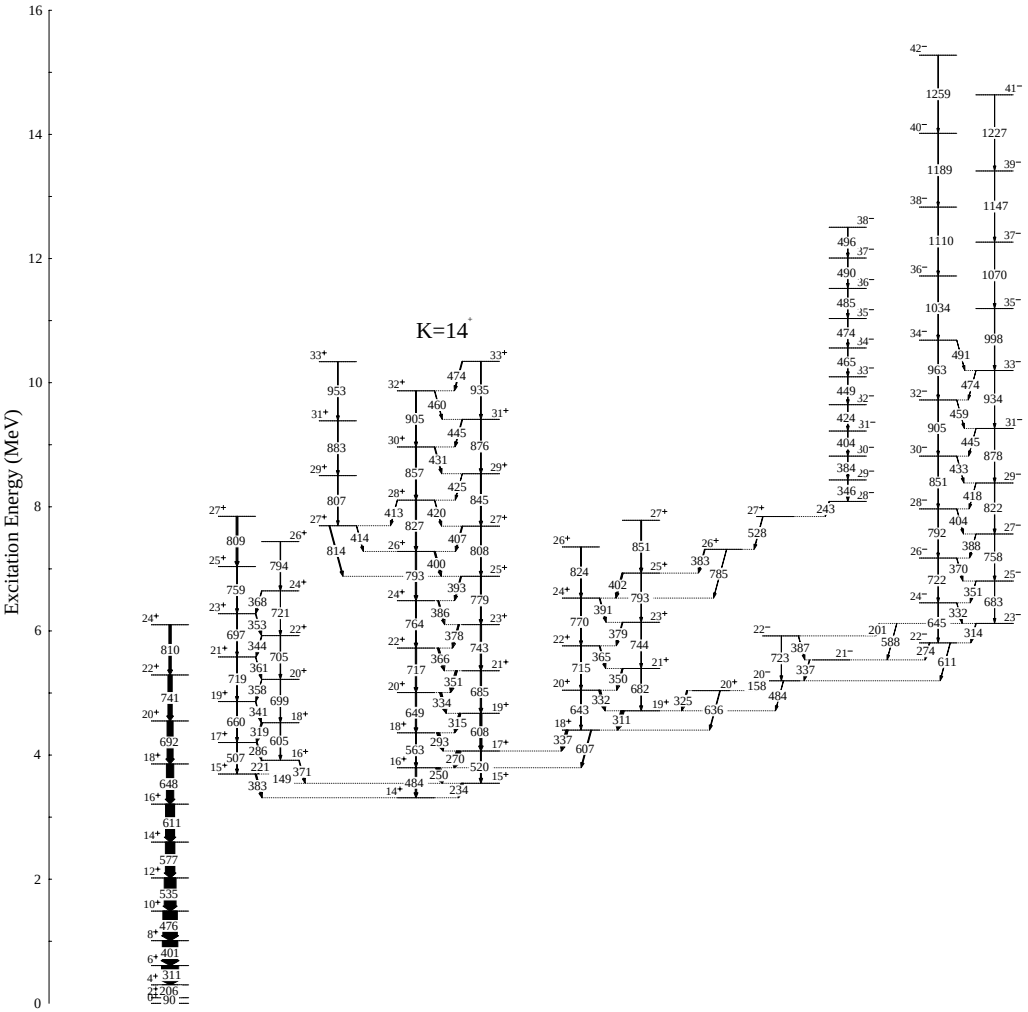


Figure 4.3: Partial level scheme of ^{174}Hf showing the band structures that lie above the $K = 14^+$ isomer and the ground-state band. The $\Delta I = 1$ transitions in the rotational band built on the 14^+ level as well as transitions from the ground-state band are identified in the spectra of all of the SD bands. The level scheme for the structures above the isomer is reproduced from [Har05a].

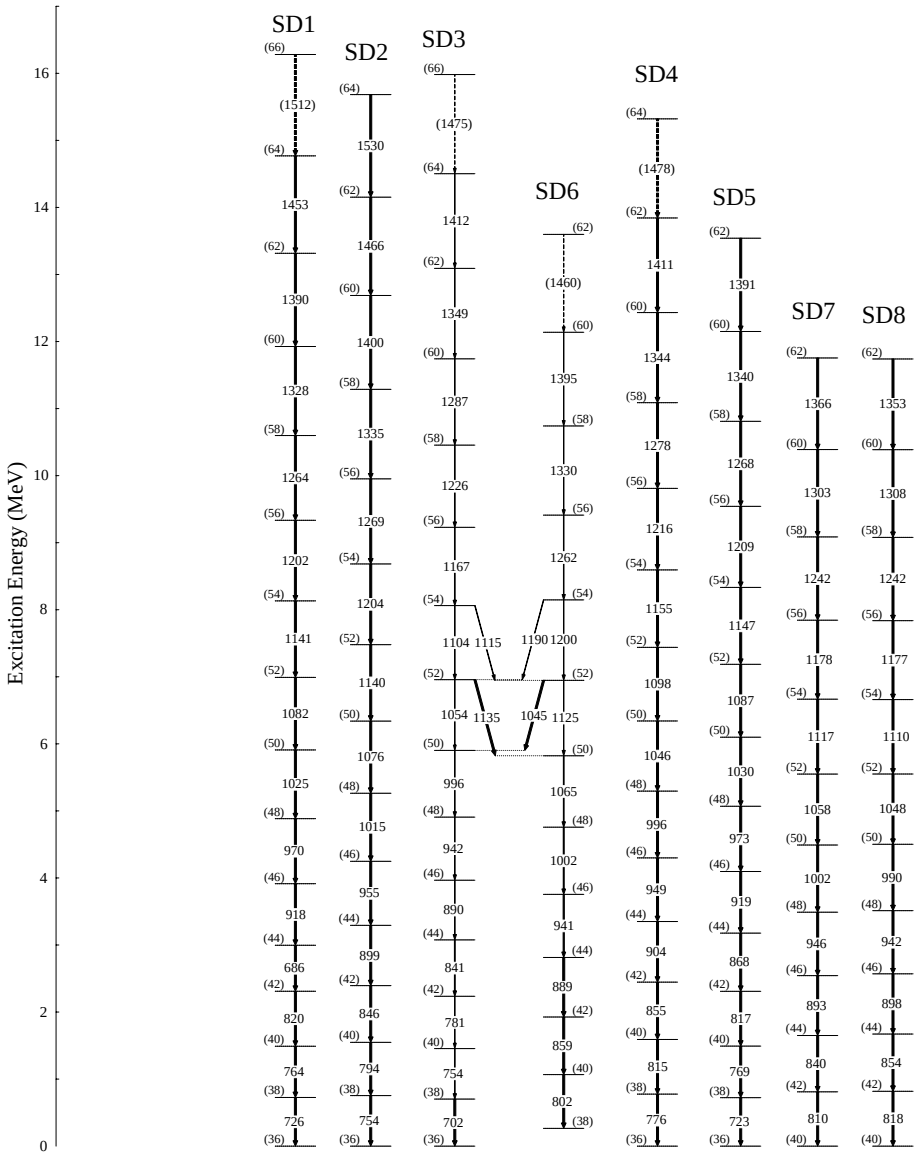


Figure 4.4: The newly discovered superdeformed bands in ^{174}Hf from the GSFMA90 and GSFMA117 experiments. The excitation energy scale is normalized to zero, as no linking transitions to normal deformed structures were found. The top of the bands can be used as a convenient reference for their relative excitation. Assignments of spins and parities of the bands are tentative. The spin range estimation for the bands is based on recent work on similar structures in ^{175}Hf [Cul04].

level in SD1 in ^{174}Hf is equally high in excitation energy with the decay out level of the SD band in ^{175}Hf [Cul04].

The multipolarity of the in-band transitions of the superdeformed bands was estimated by the use of the angular correlation method, which is described in Chapter 5 and used to study normal deformed structures. Although a direct measurement of the change of intensity of the transitions was not possible, an indirect approach to distinguishing the multipolarity of the transitions was utilized. It was based on the observation that a gate placed on a transition of any multipolarity would return coincidence spectra in which transitions of different multipolarity would have different intensities. On the contrary, transitions of the same multipolarity would exhibit similar intensities. Such an analysis was performed only after the final $F(\tau)$ values were deduced. By the use of these values, gates placed on in-band transitions in the superdeformed bands revealed coincidence spectra that had peaks from both the superdeformed bands and the ground-state band. It was found that the ratio of intensities of these peaks at different angles had similar values. Since the transitions of the ground-state band in ^{174}Hf are known to be of $E2$ type, the similar ratio supported the assignment of an $E2$ multipolarity of the in-band transitions in the superdeformed bands in ^{174}Hf.

The bands also exhibit large second moment of inertia (typical values are shown in the plot in Fig. 4.5 and also Fig. 4.6). The second moment of inertia in Fig. 4.5 illustrates the differences between the normal deformed and superdeformed structures. At a low rotational frequency, the $\mathcal{J}^{(2)}$ for the ground-state band has a value of $50\hbar^2$/MeV. Its increase around $\hbar\omega = 0.3$ MeV corresponds to the disturbance caused by an alignment of high-j particles. As a contrast, the $\mathcal{J}^{(2)}$ value for the superdeformed band starts from a high value of $100\hbar^2$/MeV and evolves rather smoothly with rotational frequency. This higher value likely corresponds to a higher deformation of the rotating core, and it does not exhibit changes due to a crossings. However, in order to experimentally verify the large deformation, another experiment was performed and described below.

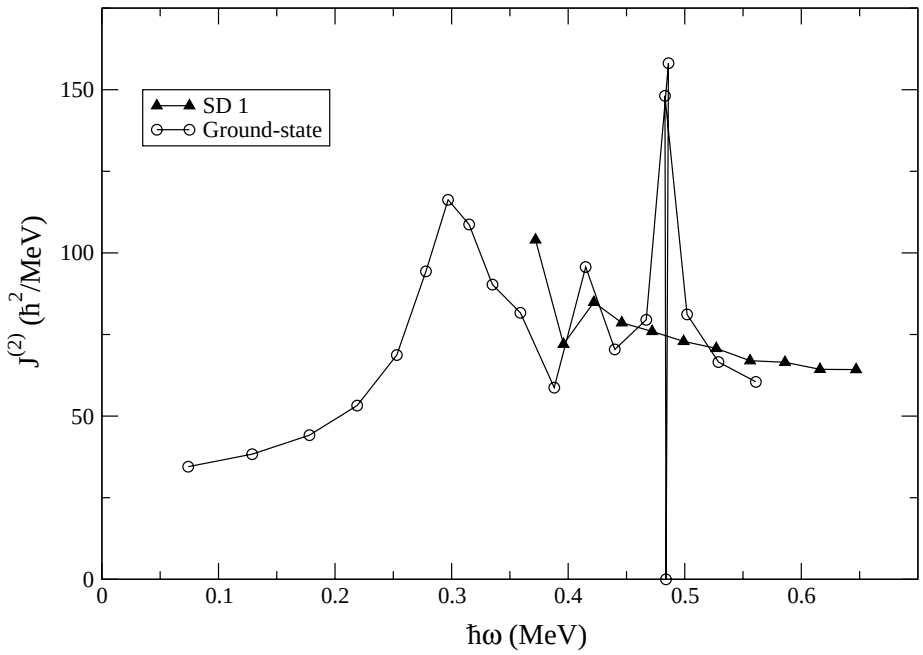


Figure 4.5: The second moment of inertia of the ground-state band and rotational band SD 1 in ^{174}Hf. At low rotational frequency, a typical value is around $50\,\hbar^2$/MeV for a normal deformed band, while the band SD1 starts with values about $100\,\hbar^2$/MeV. All other SD bands have similar values of their moments of inertia (see also Fig. 4.6).

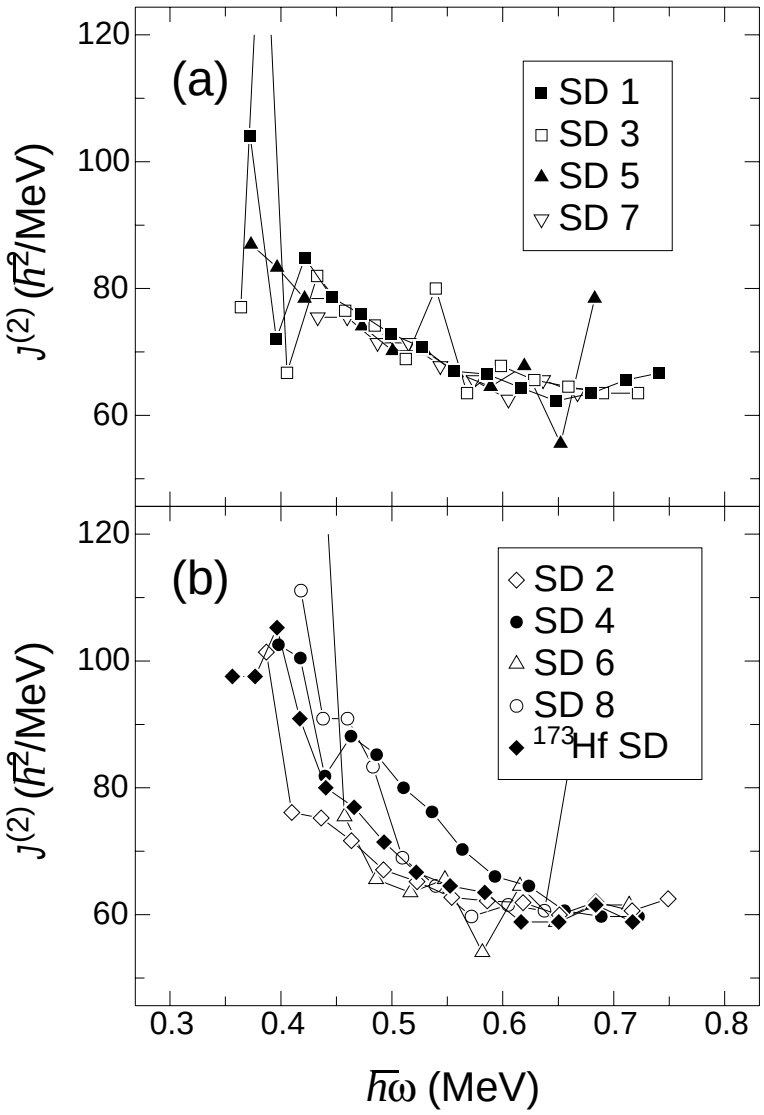


Figure 4.6: The dynamic moments of inertia for the eight SD bands in ^{174}Hf and one in ^{173}Hf. The bands in ^{174}Hf were split into possible "families" based on their similarity of the moments of inertia.

4.2 Lifetime Measurements

A higher second moment of inertia is often attributed to a higher deformation of a rotational structure. However, it does not reveal the deformation in a quantitative way. A more clear insight can be obtained from a measurement that involves data directly related to the transition probabilities, namely, intensities and Doppler shifts.

The transition quadrupole moments Q_t of the four most intense SD bands have been determined in this work through the Doppler Shift Attenuation Method (DSAM), which was discussed in Section 3.6.1. Here more details of its implementation are given.

The initial energy and velocity of the compound nucleus ^{178}Hf were determined from Eqn. 3.6 and Eqn. 3.7 by taking into consideration the energy loss of the ^{48}Ca ions up to the middle of the target. The initial velocity of ^{174}Hf has been determined with the assumption that the evaporation of the four neutrons from the compound nucleus happens in an instant compared to the characteristic time for slowing down. The initial recoil velocity for ^{174}Hf was calculated to be $\beta_0 = 0.0253$ for a ^{48}Ca ion with an initial energy of 200 MeV in a ^{130}Te target.

The process of slowing the recoils affects the observed shape of the emitted line. Depending on the lifetime of each particular level, the energy of the emitted γ ray will depend not only on the angle at which it is observed, but also on the moment of time it is observed. That is, there exists a velocity distribution of the recoils, $P(v, t)$. This was estimated using the code SRIM 2003 [Zie85]. The code provided the electronic and nuclear stopping powers which were used in the code FITFTAU [Moo97] to estimate the transition quadrupole moment.

The determination of $F(\tau)$ values requires Doppler shifted spectra for each band. This task is not trivial since the spectra must be produced by gating on particular energies within the band, which are already shifted in energy. This problem was solved by first performing an exhaustive search for values of two gating energies until the best enhancement of neighboring peaks was achieved (see Fig. 4.7), and then using their centroids when further gating was performed. The initial values of the search were based on the $F(\tau)$ values corresponding to the quadrupole moment in ^{168}Hf [Amr01]. Fig. 4.7, a) provides an illustration of when gates were set assuming the peaks were fully stopped. Only background is produced, which suggests that the gating transitions are Doppler shifted. In the case of short lived energy levels, transitions from them will be shifted in energy during the stopping time of the recoil nucleus. Thus the assumption of a fixed energy is correct and gating on such a transition will return the spectrum seen in Fig. 4.7 a). On the contrary, if the gating energy is chosen carefully for each angle and asumming a Doppler shifted energy, the

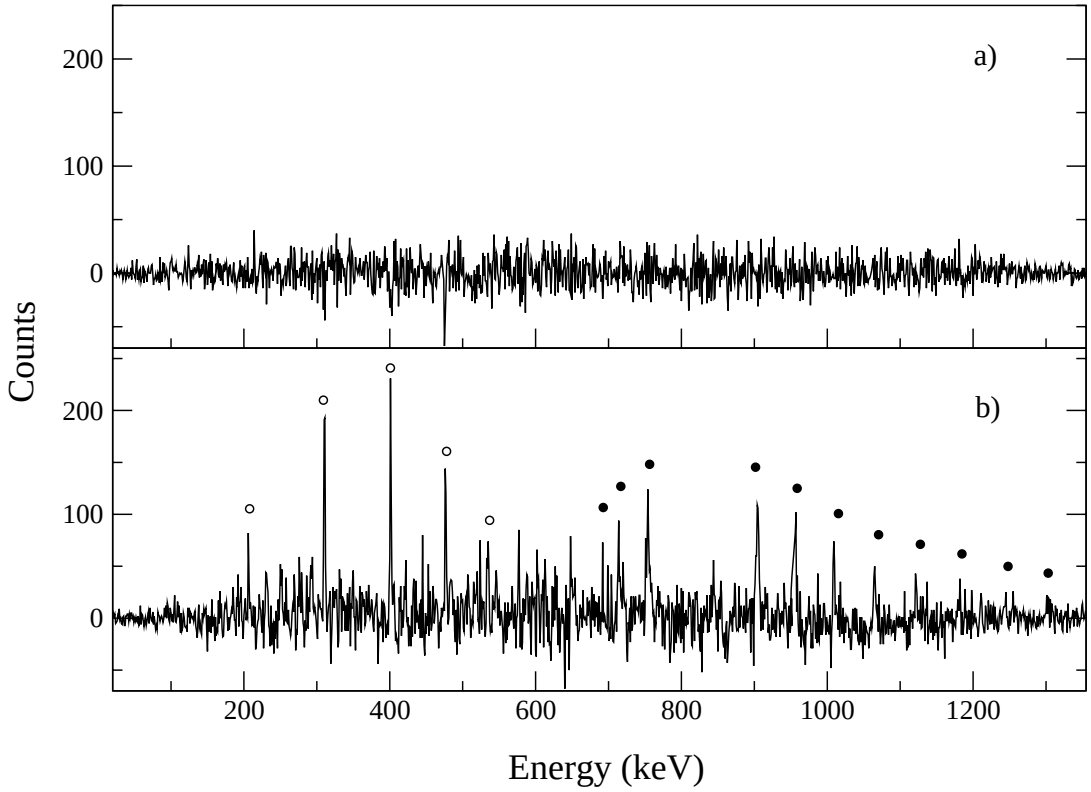


Figure 4.7: Illustration of the iterative gating procedure. Both spectra are taken at a fixed angle of the GAMMASHPERE, different from 90°. Spectrum a) has been produced by using the unshifted energies 820 keV and 867 keV from SD1 in ^{174}Hf. The energies are background only, as they do not return discrete lines. Spectrum b) shows the best enhancement of the transitions in the band when the gating energies are allowed to vary with angle. The open circles denote transitions from the ground-state band. The filled circles denote transitions that belong to SD1.

Table 4.1: Summary of DSAM analysis for SD bands in ^{174}Hf.

Band	$Q_0(eb)$	$Q_{sf}(eb)$	χ^2/dof
SD1	$13.8^{+0.3}_{-0.4}$	$8.4^{+0.3}_{-0.3}$	11.39/10
SD2	$13.5^{+0.2}_{-0.3}$	$8.0^{+0.3}_{-0.2}$	8.84/9
SD3	$13.0^{+0.8}_{-0.4}$	$10.3^{+0.6}_{-0.8}$	2.22/7
SD4	$12.6^{+0.8}_{-0.8}$	$10.2^{+1.6}_{-1.3}$	2.44/7

structure of the rotational transitions emerges (Panel (b) in Fig. 4.7). These effects were the first indication that a higher deformation should be associated with these bands. A spectrum produced by the sum af spectra obtained from gating on all possible pairs of transitions within the band ("fully gated") is shown in Fig. 4.8. In total of 15 spectra were produced for each gate corresponding to the different rings in GAMMASPHERE. The angle of the rings along which the gating was performed are 17.27°, 31.72°, 37.38°, 50.07°, 58.28°, 69.82°, 79.95°, 90°, 100.05°, 110.18°, 121.72°, 129.93°, 142.62°, 148.28°, and 162.73°, where the 79.95° and 100.05° are the result of summing two sets of rings that are only 1.5° different.

For the first four SD bands, the fully summed spectra were used to track the shift of each peak along the 15 angles. The non-relativistic Doppler shift formula was used [Kon99]

$$E(\theta) = E_0(1 + \beta_0 F(\tau)\cos(\theta)), \tag{4.1}$$

where E_0 is the stopped value for the centroid of the peak and $E(\theta)$ is its value at a given angle. A linear fit to extract both E_0 and $F(\tau)$ was performed by the use of Eqn. 4.1. The $F(\tau)$ values obtained for the first four SD bands are displayed in Fig. 4.9. FITFTAU [Moo97] was then used to determine the quadrupole moments from the $F(\tau)$ values. In the FITFTAU code both the transitional quadrupole moment Q_t and the transitional quadrupole moment of the sidefeeding structure Q_{sf}, were free parameters. Several assumptions were made in the code:

- The Q_t moment is constant within a given band; the SD bands are very collective in nature and thus no major changes of the shape are expected.
- The sidefeeding cascades have a common, constant quadrupole moment Q_{sf}. Similar arguments as above can be used.
- The number of transitions feeding levels of the main cascade is proportional to the number of transitions above the state of interest.

A summary of the results for bands SD1-4 in ^{174}Hf is presented in Table 4.1. Large

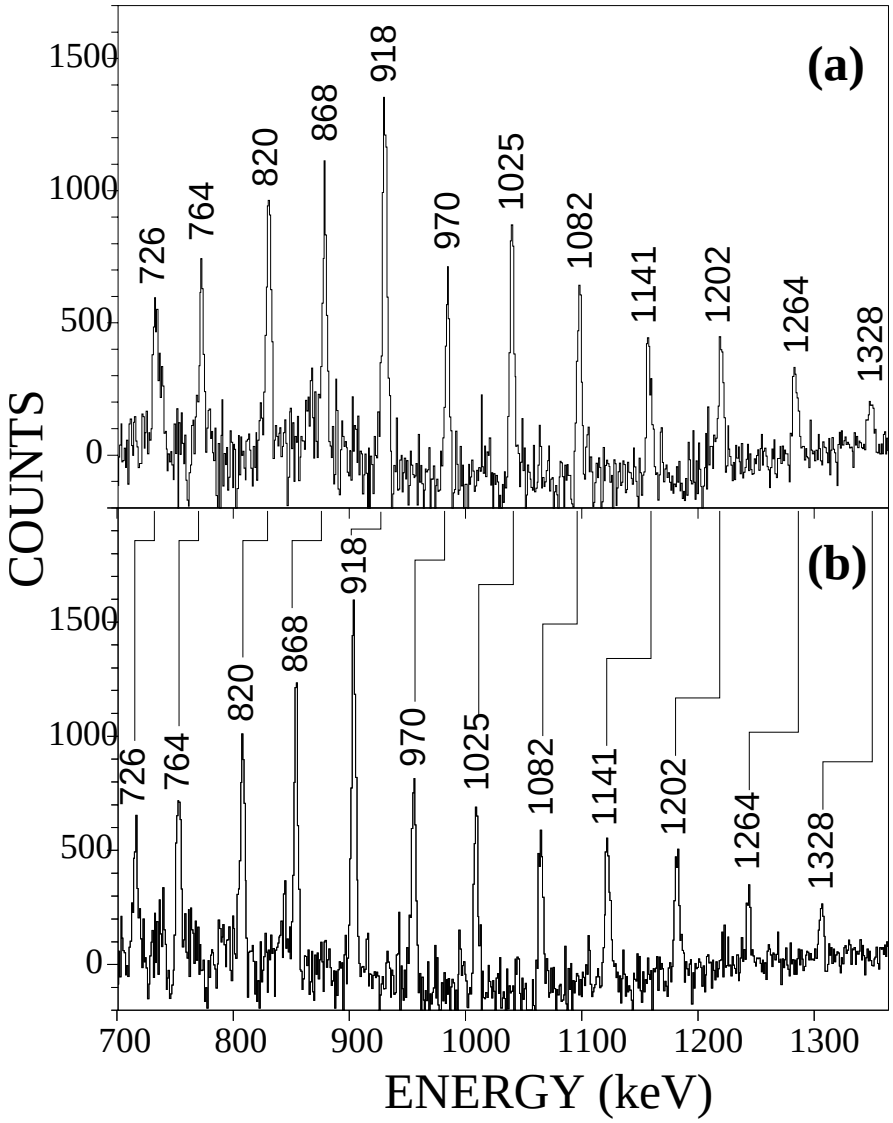


Figure 4.8: The fully summed spectrum of SD1 in ^{174}Hf. The displayed spectra are at a) 50° and b) 130°. The peaks are marked with their unshifted energies.

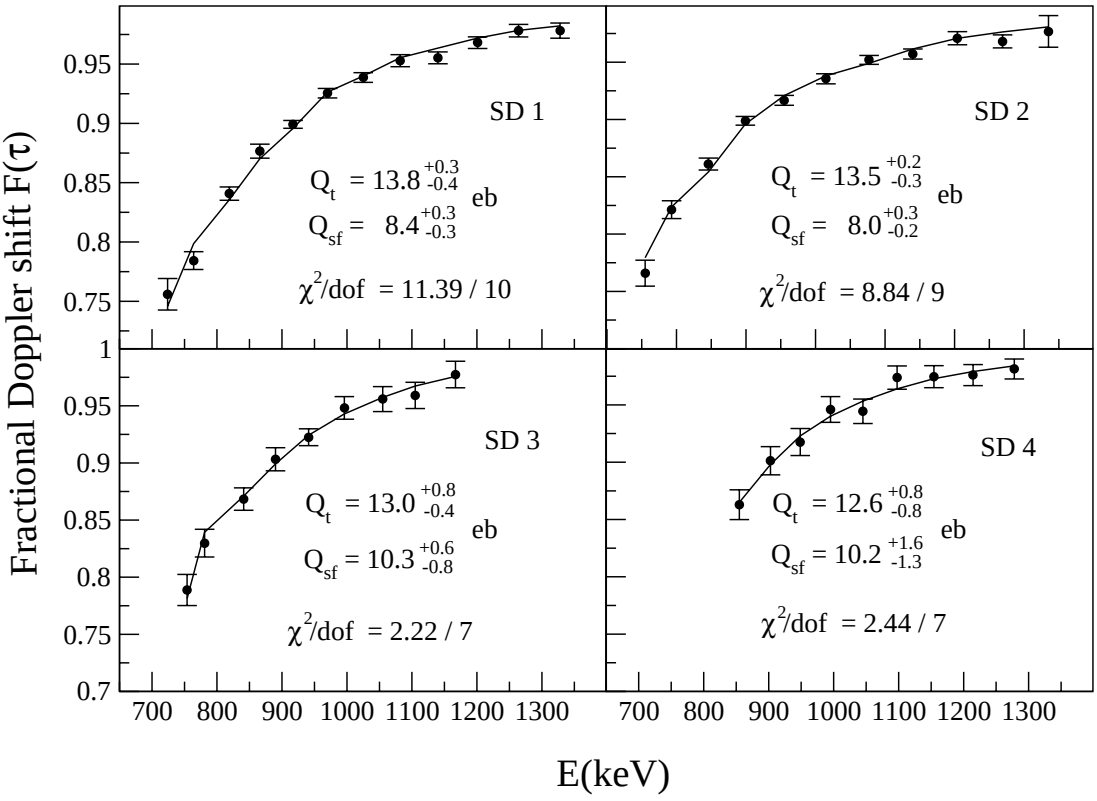


Figure 4.9: $F(\tau)$ curves for the most intense SD bands in ^{174}Hf. The uncertainties of the quadrupole moments are taken at $\chi^2_{min} + 1$.

deformation has been established as the quadrupole moments of the bands are in the range between $Q_t = 12.6 - 13.8\,\mathrm{eb}$, where normal deformation in this nucleus corresponds to $Q_t = 7\,\mathrm{eb}$ [Wal83]. The quoted uncertainties are based on the uncertainty in determining the centroid energy of the peaks only. An additional systematic uncertainty of $15 - 20\%$ should be added to account for uncertainties in the stopping powers. However, this does not affect the relative Q_t values as these bands were produced under the same experimental conditions. These moments are not as high as those seen in the well established regions of superdeformation $A = 150$ and 190, where typical quadrupole moments are in the range of $Q_t = 16 - 20\,\mathrm{eb}$. In fact the $A = 170$ region of strong deformation may well be similar to that defined by the $A = 130$ highly deformed nuclei and could possibly be viewed as "transitional" between $A = 150$ and $A = 190$ regions. The implication of the large Q_t moments for the interpretation of the nature of these bands is discussed in the next Section.

The search for linking transitions between SD bands was conducted using coincidence cubes and hypercubes from the thin target data. In total, eight rotational bands have been discovered from both experiments. All of them have similar moments of inertia (see Fig. 4.6) and were assigned to ^{174}Hf on the basis of observed coincidences with transitions in the ground-state band. Spectra of the bands are presented in Fig. 4.1 and Fig. 4.2. The SD5 band is nearly identical to SD1, as the transitions energies differ by less than 7 keV throughout most of the band. The spectrum shown in Fig. 4.2(i) shows a candidate SD band in ^{173}Hf, similar to the ^{174}Hf SD bands. Linking transitions to the low-lying states could not be observed. But clear coincidence of the band with known transitions in ^{173}Hf was found. It should also be noted that this band was populated as strongly as SD1 in ^{174}Hf and is isospectral to SD2.

Unfortunately, no linking transitions nor coincidence relationships consistent with wobbling excitations were observed between any of the eight SD bands in ^{174}Hf. In ^{163,165,167}Lu, the strength of linking transitions from wobbling excitations to the $n_w = 0$ band was found to be comparable to that of the in-band transitions: branching ratios ($I_{\mathrm{in}}/I_{\mathrm{out}}$) near the bottom of the wobbling bands were determined to be $\sim 1 - 3$ in these nuclei. As linking transitions between the bands could not be observed in ^{174}Hf only limits for these branching ratios at the bottom of the bands could be determined. These limits were obtained assuming that I_{out} was equal to the intensity of the weakest observable peak in the spectrum from which $I_{\text{in-band}}$ was measured. The limiting branching ratios were found to be $21, 13, 11, 7, 18, 15,$ and 5 for SD2-8, respectively.

4.3 Discussion

Ultimate Cranker calculations were performed in order to help interpret the nature of the SD bands. A sample calculation is found in Fig. 4.10 which shows the energy surfaces at $I = 51\,\hbar$. Large deformation wells are predicted and are found to have significant triaxial deformation. Therefore, the region of triaxial deformation appeared to extend to $N > 100$, which is larger than first thought. In addition, this was surprising as no SD bands were observed in ^{164,166}Hf [Jen00], where the TSD minimum is predicted to be most favored. Thus, we begin a search for experimental evidence of triaxiality in these bands.

Based on the present experimental facts, we will address the possibility that these sequences in ^{174}Hf are associated with triaxial deformation. It is important to first note that SD1 is nearly isospectral with one of the SD bands observed in ^{175}Hf [Cul04]. The latter structure has been linked to the known levels, and thus the excitation energy (12.682 MeV) and spin/parity ($79/2^-$) of the lowest state have been determined. A seven quasiparticle configuration including two $i_{13/2}$ protons, two $i_{13/2}$ neutrons, and two $j_{15/2}$ neutrons has been proposed for this sequence in ^{175}Hf. Identical bands, especially those with large deformation, are often associated with closely related configurations. In particular, they often contain the same high-j orbitals [Bak95]. Thus, the superdeformed deformed bands in ^{174}Hf may well be based on configurations with at least six quasiparticles and be located at high excitation energies (> 10 MeV). Assuming spins similar to those of the identical band in ^{175}Hf can also explain the lack of linking transitions to the normal deformed structures. Indeed, the lowest spin of the superdeformed bands in ^{174}Hf is $\sim 36\,\hbar$, and the highest spin that is observed to be fed in the ground-state band by the SD bands in ^{174}Hf is $24\,\hbar$ (Fig. 4.3). This leaves a spin difference of $\sim$12 $\hbar$ between the two structures. Together with the large energy separation from the ground-state band, the large spin range indicates that it is unlikely that the decay out path of the superdeformed bands follows a small number of transition steps. Instead, many weak transitions are likely involved, which make their observation impossible.

The complex configurations suggested for the Hf case are in contrast to the relatively simple quasiparticle $\pi i_{13/2}$ configuration of the lighter Lu isotopes. Evidence of this added complexity may be found in the quadrupole moments. Relatively small values of $Q_t = 6 - 10$ eb were measured for the Lu SD bands [Sch02a, Gor04], compared to those in ^{174}Hf ($Q_t = 12.6 - 13.8$ eb) and ^{168}Hf ($Q_t = 11.4^{+1.1}_{-1.2}$ eb [Amr01]). The larger deformation in ^{174}Hf can be explained by the suggested presence of the intruder $j_{15/2}$ neutrons in the configuration of SD1. The $j_{15/2}$ orbital, which originates above the $N = 126$ spherical shell gap, is known to drive nuclei to higher deformations, such as in the mass 150 and

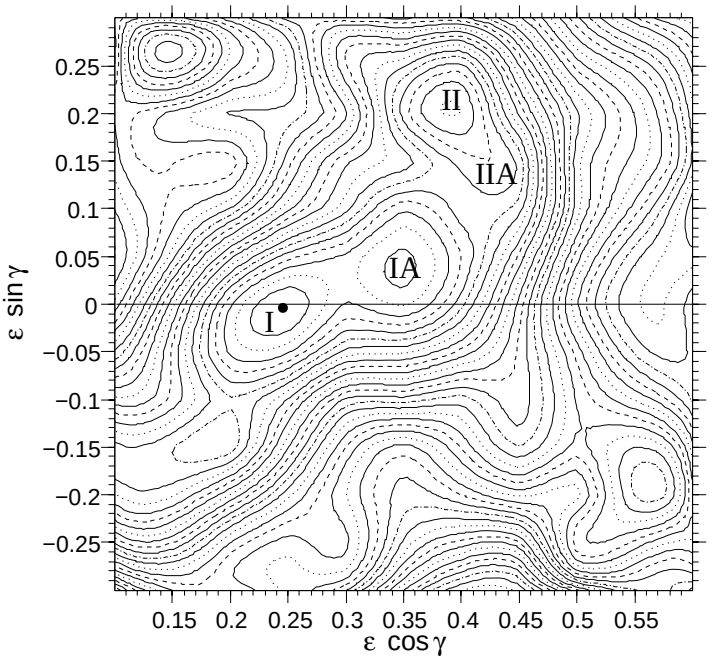


Figure 4.10: Potential energy surface for ^{174}Hf for the lowest (π, α) = (+,0) configuration at spin $I = 50\,\hbar$. The spacing between contours is 200 keV.

190 regions [Ben88]. The similarity of the quadrupole moments measured for bands 1-4 in ^{174}Hf suggests related configurations in all cases and thus the involvement of $i_{13/2}$ protons and $j_{15/2}$ neutrons in each band. Therefore, the Hf bands appear to be part of a different "class" of SD bands than the Lu SD cases [Cul04].

A side observation that suggests that some of the SD bands in ^{174}Hf are based on different configurations is the observed linking transitions between SD3 and SD6 due to accidental degeneracy. From the level scheme in Fig. 4.4, it can be inferred an energy difference of 10 keV between the levels denoted as 52. This implies an interaction matrix element of approximately 5 keV, which indicates a weak interaction strength. The presence of the linking transitions, however, indicates the same parity for SD3 and SD6 (as mentioned in Section 4.1, an $E2$ character is assigned to the in-band transitions), since a possible $M2$ transition (the most intense in the case of different parities) is suppressed compared to $E2$. Thus, the same parity can be associated with Bands SD3 and SD6 and different internal configuration for both due to the small interaction strength.

An intriguing feature of the SD bands is the observed correlation between them and transitions that belong to the band built on the $K = 14^+$ isomer in ^{174}Hf (Fig. 4.1, panel d, and Fig. 4.3). The band head of this high-K structure has a microsecond half life resulting

from ΔK selection rules, which is valid in the case of an axially symmetric shape. In this case the decay path between the SD bands (with presumably low-K orbitals involved in their configuration) and high-K states could be as a consequence of the proposed triaxiality, as K is not a good quantum number for an axially asymmetric shape. As an alternative, such decay can be consistent with the proposition of a presence of multiple levels between the SD and normal deformed structures. The latter suggestion seems to be more consistent with the current experimental data, since we have no indication of inter-band transitions and thus wobbling modes.

If the superdeformed sequences in ^{174}Hf are triaxial as suggested by the UC calculations, a family of bands with nearly identical moments of inertia is expected to be observed. Each band would be associated with a different wobbling quantum. It is indeed possible to group the bands in ^{174}Hf into two distinct families based on the behavior with frequency of their moments of inertia (Fig. 4.6(a)). Bands $1, 3, 5$, and 7 all have nearly the same moments over the observed frequency range, while bands $2, 6$, and 8 also have moments similar to each other, but approximately 10 % less in magnitude. In the context of triaxiality, this could suggest two $n_w = 0$ configurations associated with bands 1 and 2, with the weaker structures representing wobbling excitations built on each. The existence of two families in ^{174}Hf would imply two TSD minima, a possibility supported by the UC calculations. Indeed, TSD minima are predicted for all parity/signature combinations, thus SD1 and SD2 may result from two minima with different parity and/or signature. However, the presence of SD bands with similar moments of inertia is not unique to wobbling. Observing linking transitions between these bands is necessary to validate this picture. Since such transitions have not been observed, the presence of triaxiality cannot be asserted. Band 4 has a unique $\mathcal{J}^{(2)}$ profile in comparison with the other sequences, which may indicate that it is built on yet another configuration.

As seen from Fig. 4.6(a), SD 1 and 3 do have similar moments, thus SD3 may be a wobbling excitation based on SD1. The quadrupole moment of a wobbling excitation should be the same as that of $n_w = 0$ band (associated with SD1), as it is the case in ^{163}Lu [Gor04]. Although the measured moment of SD3 ($13.0^{+0.8}_{-0.4}$ eb) is somewhat smaller than that of SD1 ($13.8^{+0.3}_{-0.4}$ eb), the values do agree within the uncertainty, which supports this interpretation. However, this is once again not conclusive as many superdeformed bands have similar quadrupole moments. Unfortunately, the population weakness of bands $5 - 8$ did not allow for a reliable measurement of their quadrupole moments.

Not only do the present experimental data not prove triaxial deformation for ^{174}Hf, they also result in some inconsistencies with the theoretical predictions if triaxiality were present. For example, the measured quadrupole moments are significantly larger than

those calculated by UC. The total energy surface of the (π, α)=(+,0) configuration at spin $I = 50\,\hbar$ is shown in Fig. 4.10. Various minima were tracked over a broad range of spin $(0 - 58\,\hbar)$. Located near $\epsilon_2 = 0.25$ and $\gamma = 0°$, minimum I is representative of the normal deformed configurations. The lowest TSD minimum is labeled II, with parameters $\epsilon_2 = 0.45$ and $\gamma \approx 27°$ ($Q_t \sim 9.9\,\mathrm{eb}$). A similar minimum is found in each of the parity/signature combinations, and is also observed over a wide spin range ($> 27\,\hbar$). These deformations are lower than the experimentally determined values. Since the assertion of triaxiality is based solely on the UC results, such a large discrepancy is cause for concern.

A second TSD minimum appears to be located near minimum II and has been labeled IIA in Fig. 4.10. This minimum has deformation parameters $\epsilon_2 = 0.47$ and $\gamma \approx 18°$, corresponding to a quadrupole moment of $\sim 12.2\,\mathrm{eb}$. Perhaps some of the SD bands in ^{174}Hf can be associated with this minimum, since the predicted quadrupole moment lies near the experimental values. However, in the UC calculations, this minimum is only observed over a short spin range $(50 - 56\,\hbar)$ and is only found for the (π, α)=(+,0) combination. One may also consider minimum IA to possibly describe the observed bands. Minima similar to IA are found in all of the parity/signature combinations with $\epsilon_2 = 0.35$ and $\gamma \approx 8°$. However, its predicted quadrupole moment ($\sim 9.9\,\mathrm{eb}$) is again lower than that observed. Therefore, it appears that the UC is not able to accurately account for the superdeformed bands in ^{174}Hf. Further theoretical investigation is needed to explore the nature of the observed excitations.

It is also interesting to note that only a single SD band is found in the odd-A neighbors ^{173}Hf and ^{175}Hf [Cul04], in sharp contrast with the multiplicity of bands seen in ^{174}Hf. This observation is not a question of sensitivity: as can be seen from Fig. 4.2, the candidate SD bands in ^{173}Hf was populated with nearly the same strength as SD1 in ^{174}Hf. Since a family of bands was found with SD1, a family of rotational bands would also be expected in ^{173}Hf if the superdeformed structures were indeed triaxial, and if similar energies were associated with the wobbling phonons. If the wobbling excitations were at higher energies in ^{173}Hf, however, a lower population could account for their absence. Another possible explanation for the missing bands is that the superdeformed structure in ^{173}Hf does not lie in a TSD minimum. It seems unlikely, however, that if a triaxial minimum were present, it would not exist in both ^{173}Hf and ^{174}Hf.

The results about possible triaxial shapes in Hf nuclei described in this chapter induced a search for these structures in mass regions different from Hf and Lu. A recently performed experiment on ^{171}Ta [Har05b] investigated the possibility for presence superdeformed bands and wobbling mode in this nucleus. The presence of superdeformation was expected due to the previously identified shape-driving $\pi i_{13/2}$ orbital in ^{171}Ta. The sequence based on

this orbital was extended to spin $101/2\,\hbar$. It was noticed that the rotational structure built on this orbital exhibited the features of higher deformation like a regular spacing in the spectrum of the transitions as well as a small value of this spacing. However, no lifetime measurements were performed in this experiment thus no firm estimation of the amount of deformation in this band was made. No side bands that feed to the band built on the $\pi i_{13/2}$ orbital that could be candidates for a wobbling mode were identified. This provides a negative result for the presence of triaxiality outside the Lu region, which for now remains the only region to clearly exhibit this feature.

Chapter 5

Study of Normal Deformed Bands

In the investigation of bands that are based on zero- and two-quasiparticle configurations, data from the previously described experiment GSFMA117 (Chapter 4) were used. The extension of the rotational bands to high spin was achieved by the use of the RADWARE package with a cube and a hypercube.

The BLUE database was also used on the GS2K047 data to perform angular correlation analysis. Gates were set on known $E2$ transitions and the resulting spectra were examined at different angles. For each transition of interest, two summed spectra were used - one near 90° (summed spectra at 79°, 81°, 90°, 99°, and 101°) and one near the forward angles (122°, 130°, 143°, 148° and 163°). The ratio of the probabilities of the transitions is used to distinguish between stretched $\Delta I = 1$ and $\Delta I = 2$ transitions (that is, quadrupole and dipole transitions); $D = \frac{W(\theta_f)}{W(\theta_{90°})}$. The two angle groups contained 27 and 30 detectors, which introduced an additional correction coefficient of 0.9. The experimental values are defined as $D = 0.9\frac{I_f}{1.5\, I_{90°}}$, where I are the areas of the peaks in the summed spectra for both angle groups and 1.5 is a normalizing factor. The normalized values for D are about 0.6 for known $E1$ transitions, and 1.0 for known $E2$ transitions. Unfortunately, multipolarities of only the lowest lying transition energies could be determined directly from the BLUE database, as the Doppler broadening becomes more severe at higher energies. That effect is more prominent when the lifetime of the levels becomes comparable with the characteristic velocity of the recoil in the stopper.

Data for level energies, intensities, and transitions are shown in Table 5.1. The uncertainties for all of the transition energies are about 0.2 keV. All of the intensities of the γ rays were obtained in two complementary ways - by setting gates below each level, and setting gates above the level of interest and determining the branching ratios of other transitions that depopulate the level.

Table 5.1: Relative intensities and energies of transitions in ^{174}Hf.

I_i^π	E_{level}(keV)	E_γ(keV)[a]	I_γ	D[e]	Multipolarity[c]
Band 1 (+,0)					
2^+	90.5	90.5	N-A		E2
4^+	296.9	206.4	1058.4(5)		E2
6^+	607.6	310.7	1000.0		E2
8^+	1008.9	401.3	714.1(4)	1.05(1)	E2
10^+	1485.3	476.4	603.6(4)	1.08(1)	E2
12^+	2019.9	534.6	417.4(4)	1.09(1)	E2
14^+	2596.8	577.0	327.1(4)	1.07(1)	E2
16^+	3208.3	611.4	298.8(8)	1.05(2)	E2
18^+	3856.5	648.2	193.7(8)	1.02(2)	E2
20^+	4548.9	692.5	140.2(7)	0.82(1)	E2
22^+	5290.3	741.5	81.8(5)		E2
24^+	6099.9	809.6	36.4(3)		E2
		767.5	14.0(8)		E2
26^+	6951.3	851.4	25.7(3)		E2
28^+	7859.5	908.2	24.1(4)		E2
30^+	8818	958.5	16.3(3)		E2
32^+	9801.8	983.8	11.5(3)		E2
34^+	10754.2	952.4	6.0(2)		E2
36^+	11733.6	979.4	4.7(2)		E2
38^+	12762.3	1028.7	2.4(1)		E2
40^+	13851.1	1088.8	1.5(1)		E2
42^+	15006.1	1154.9	1.0(1)		E2
Band 2 (+,0)					
4^+	1062.5	765.8	2.7(2)		E2
6^+	1307.4	244.9	14(1)[b]		E2
		699.8	54.9(1)	0.75(3)	M1/E2
		1011.0	25(4)[b]	0.92(7)	E2

Table 5.1 – Continued

I_i^π	E_{level}(keV)	E_γ(keV)[a]	I_γ	D[e]	Multipolarity[c]
8^+	1630.5	323.1	4.4(3)		E2
		621.0	7.7(8)[b]	0.90(2)	M1/E2
10^+	2026.3	395.8	3.8(3)		E2
		540.0	4.1(4)[b]	0.98(1)	M1/E2
12^+	2488.9	462.6	17(2)	1.03(2)	E2
		468.5	15(2)[b]	1.03(1)	M1/E2
14^+	2992.5	503.6	31(2)	1.0(3)	E2
		395.0	3.8(3)[b]	1.12(2)	M1/E2
		973.0	6.5(4)[b]	1.14(3)	E2
16^+	3500.4	507.9	25(1)	0.92(3)	E2
		292.0	0.90(9)[b]	1.03(5)	M1/E2
		903.0	1.7(3)[b]	1.15(4)	E2
18^+	4048.0	547.6	21(1)	1.04(2)	E2
20^+	4656.0	608.0	21(1)		E2
22^+	5333.0	677.0	10.8(7)		E2
		784.0	3.5(2)[b]		E2
24^+	6062.0	729.0	4.6(4)		E2
		773.0	6.8(9)[b]		E2
26^+	6867.0	806.2	2.9(2)		E2
28^+	7730.0	862.3	2.2(2)		E2
30^+	8648.0	918.2	1.6(1)		E2
32^+	9619.0	971.4	1.5(1)		E2
34^+	10637.3	1018.3	0.75(5)		E2
36^+	11692.7	1055.4	0.47(5)		E2
38^+	12782.0	1089.3	0.24(6)		E2
40^+	13850.7	1068.7	0.12(3)		E2
Band 3 (-,0)					
4^-	1426.0	1129.1	>105(2)	0.93(6)	E1 $\Delta I = 0$
6^-	1634.6	208.6	>105(2)		E2
		1026.0	313.5(1)	1.08(2)	E1 $\Delta I = 0$
8^-	1928.7	293.9	105(2)	0.95(1)	E2

Table 5.1 – Continued

I_i^π	E_{level}(keV)	E_γ(keV)[a]	I_γ	D[e]	Multipolarity[c]
		918.2	44.8(1)[b]	1.08(2)	E1
10^-	2299.8	370.7	88(2)	1.01(1)	E2
		813.8	4.0(3)[b]	0.94(3)	E1
12^-	2744.5	444.4	72(2)	1.1(1)	E2
14^-	3260.5	515.8	58(2)		E2
16^-	3832.5	572.0	45(1)		E2
18^-	4458	625.5	41(1)		E2
20^-	5139.8	681.6	30(1)		E2
22^-	5877.9	738.6	11.1(5)		E2
24^-	6653.7	776.2	5.6(4)		E2
26^-	7471.2	817.7	5.9(4)		E2
28^-	8326.6	855.3	4.2(2)		E2
30^-	9222.6	896.8	4.7(4)		E2
32^-	10164.4	942.0	3.8(4)		E2
34^-	11143.6	978.3	3.2(3)		E2
Band 3 (-,1)					
7^-	1650.6	1043.0		0.48(3)	E1
9^-	1943.6	293.1	2.2(1)		E2
		934.1	11.7(1)[b]	0.65(3)	E1
		457.6	3.5(2)[b]	0.67(2)	E1
11^-	2318.9	375.3	22.1(1)		E2
		832.6	35.1(1)[b]	0.59(1)	E1
		298.5	2.8(5)[b]	0.67(3)	E1
13^-	2771.7	452.8	18.2(2)		E2
		751.4	10.4(4)[b]	0.59(1)	E1
15^-	3296	524.5	14.3(3)	1.07(1)	E2
		698.0[f]	3.0(3)	0.49(1)	E1
17^-	3885.6	588.9	11.4(2)	1.10(1)	E2
		676.0	1.5(1)[b]	0.67(1)	E1
19^-	4531.7	646.1	8.6(4)		E2
21^-	5228	696.2	5.7(3)		E2

Table 5.1 – Continued

I_i^π	E_{level}(keV)	E_γ(keV)[a]	I_γ	D[e]	Multipolarity[c]
23^-	5960.3	732.0	4.5(3)		E2
25^-	6699.3	738.8	3.9(3)		E2
27^-	7469.8	770.1	2.5(2)		E2
29^-	8297.1	827.3	1.8(2)		E2
31^-	9185.1	888.2	1.5(1)		E2
33^-	10134.1	949.0	1.0(1)		E2
35^-	11142.8	1008.3	0.7(1)		E2
37^-	12206.2	1063.8	0.6(1)		E2
39^-	13304.3	1098.9	0.31(5)		E2
41^-	14391.5	1087.1	0.12(5)		E2
43^-	15515.3	1123.1	0.08(1)		E2
45^-	16674.7	1159.4	0.03(1)		E2
47^-	17872.7	1197.8	<0.02		E2
49^-	19104.7	1232.5	<0.02		E2
Band 4 (+,0)					
4^+	1394.6	1097.0	18.13(1)	0.75(5)	M1/E2
		1303.7	>28.0(4)	1.3(1)	E2
6^+	1642.3	247.0	45.1(7)		E2
		134.0	16(3)[b]		M1/E2
		1033.0	12.2(5)[b]	0.73(3)	M1/E2
		1345.0	81(2)[b]	1.08(7)	E2
8^+	1972.2	329.9	30.0(7)		E2
		174.0	4.3(3)[b]		M1/E2
		1363.0	1.7(1)[b]		E2
10^+	2379.5	407.3	40(1)		E2
		212.0	6.5(4)[b]		M1/E2
12^+	2854.9	475.4	40(4)		E2
		245.0	4.2(3)[b]		M1/E2
14^+	3392.8	537.9	30.6(3)		E2
		274.0	4.4(3)[b]		M1/E2
16^+	4001.3	608.5	26.2(9)		E2

Table 5.1 – Continued

I_i^π	E_{level}(keV)	E_γ(keV)[a]	I_γ	D[e]	Multipolarity[c]
18^+	4639.3	638.0	18.9(7)		E2
20^+	5323.9	684.6	10.1(4)		E2
22^+	6047.5	723.6	7.9(6)		E2
24^+	6819	771.5	5.2(4)		E2
26^+	7639.7	820.7	2.6(2)		E2
28^+	8484.8	845.1	1.5(1)		E2
Band 4 (+,1)					
3^+	1303.0	1211.0	>59(4)	0.44(4)	M1/E2
5^+	1508.2	204.6	59(4)		E2
		114.0	42(3)[b]		M1/E2
		900.0	22(1)[b]	1.01(1)	M1/E2
		1211.0	48(6)[b]	0.56(1)	M1/E2
7^+	1798.0	289.8	23(4)		E2
		155.0	6(1)[b]		M1/E2
		1189.0	1.1(2)[b]	0.36(2)	M1/E2
9^+	2167.1	369.1	21(4)		E2
		195.0	3.3(8)[b]		M1/E2
11^+	2609.5	442.4	17(3)		E2
		230.0	1.7(4)[b]	0.34(2)	M1/E2
13^+	3117.4	507.9	20(4)		E2
		263.0	3.4(9)[b]		M1/E2
15^+	3680.5	563.1	11(2)		E2
17^+	4312.3	631.8	4.8(9)		E2
19^+	4975.1	662.8	5.1(9)		E2
21^+	5679.3	704.2	6(1)		E2
23^+	6427.9	748.6	4.8(9)		E2
25^+	7228.0	800.1	3.8(8)		E2
27^+	8074.8	846.8	1.5(4)		E2
29^+	8973.4	898.6	1.1(3)		E2

Table 5.1 – Continued

I_i^π	E_{level}(keV)	E_γ(keV)[a]	I_γ	D[e]	Multipolarity[c]
Band 5 (-,0)					
4^-	1562.0				E2
6^-	1723.4	161.4	0.8(1)		E2
		1114.9	1.26(1)	0.91(2)	E1
8^-	1982.8	259.4	24.9(1)		E2
		144.0	1.03(3)		M1/E2
		972.0	2.8(2)[b]	1.19(5)	E1
10^-	2333.6	350.8	18.0(2)		E2
		199.0	0.21(1)[b]		M1/E2
12^-	2770.2	436.6	15.8(2)		E2
14^-	3283.1	512.9	13.8(2)		E2
16^-	3875.8	592.7	11(1)		E2
18^-	4541.8	666.0	5.1(7)		E2
20^-	5270.7	728.9	5.0(5)		E2
22^-	6036.7	766.0	1.6(2)		E2
24^-	6876.7	840.0	1.7(2)		E2
Band 5 (-,1)					
5^-	1627.7	1020.0	14.86(4)	0.65(4)	E1
		1331.0	11.2(8)		E1
7^-	1838.4	210.7	14.1(8)		E2
		115.0	15.0(2)[b]		M1/E2
		829.0	15.0(1)	0.81(3)	E1
		1230.0	19(1)	0.62(3)	E1
9^-	2135.6	297.2	26(9)		E2
		153.0	85(1)[b]		M1/E2
		1126.0	35(6)	0.65(2)	E1
11^-	2516.0	380.4	7.7(2)		E2
		181.0	5.2(2)[b]		M1/E2
		1030.0	2.0(2)	0.82(4)	E1
13^-	2973.4	457.4	6.0(1)		E2
15^-	3501.5	528.1	3.70(1)		E2

Table 5.1 – Continued

I_i^π	E_{level}(keV)	E_γ(keV)[a]	I_γ	D[e]	Multipolarity[c]
17^-	4093.6	592.1	3.69(1)		E2
19^-	4742.1	648.5	2.81(5)		E2
21^-	5427.8	685.7	1.67(3)		E2
23^-	6164.8	737.0	1.45(3)		E2
25^-	6958.2	793.4	0.76(2)		E2
27^-	7802.7	844.5	0.81(3)		E2
29^-	8692.7	890.0	0.530(2)		E2
31^-	9593.7	901.0	0.256(3)		E2
33^-	10560.7	967.0	0.241(1)		E2
35^-	11592.7	1032.0	0.170(1)		E2
Band 6 (-,0)					
6^-	1909.0	1302.0	5.53(1)	1.4(1)	E1
		261	4.2(1)[b]		M1/E2
8^-	2123.7	214.7	$<9.7(1)$[d]		E2
		119.0	3.4(8)[b]		M1/E2
		1115.0	0.74(3)	1.52(9)	E1
10^-	2428.9	305.2	7.94(6)		E2
		165.4	2.21(4)[b]		M1/E2
12^-	2822.8	393.9	6.23(5)		E2
14^-	3299.9	477.1	4.93(3)		E2
16^-	3854.6	554.7	3.92(3)		E2
18^-	4481.3	626.7	3.01(4)		E2
20^-	5174.8	693.5	2.56(4)		E2
22^-	5930.9	756.1	1.87(4)		E2
24^-	6740.7	809.8	1.36(5)		E2
26^-	7611.6	870.9	0.69(1)*		E2
28^-	8482.5	870.9			E2
30^-	9364.5	882.0	0.42(2)		E2
32^-	10285.5	921.0	0.41(3)		E2
34^-	11259.5	974.0	0.25(2)		E2
36^-	12285.5	1026.0	0.20(2)		E2

Table 5.1 – Continued

I_i^π	E_{level}(keV)	E_γ(keV)[a]	I_γ	D[e]	Multipolarity[c]
38^-	13361.5	1076.0	<0.20(2)		E2
Band 6 (-,1)					
5^-	1646.5.0	1041.0	>0.54(8)	0.46(3)	E1
		1352.0	>0.36(5)	0.74(7)	M1/E2
7^-	2002.5	356.0	10.7(6)[b]		E2
		995.0	9.07(1)	0.62(2)	E1
		95.0	2.8(3)		M1/E2
9^-	2261.9	259.4	2.03(7)[b]		E2
		140.0	1.82(5)[b]		M1/E2
11^-	2612.7	350.8	4.2(6)[b]		E2
		184.9	0.66(1)[b]		M1/E2
13^-	3049.3	436.6	2.9(6)		E2
		227.2	0.5(1)[b]		M1/E2
15^-	3565.7	516.4	2.8(5)		E2
17^-	4157.3	591.6	2.7(6)		E2
19^-	4818.0	660.7	1.9(4)		E2
21^-	5543.5	725.5	1.5(3)		E2
23^-	6328.3	784.8	1.2(2)		E2
25^-	7169.6	841.3	0.9(2)		E2
27^-	8055.1	885.5	0.5(1)		E2
29^-	8933.6	878.5	0.16(4)		E2
31^-	9835.6	902.0	0.17(5)		E2
33^-	10776.7	941.1	0.16(4)		E2
35^-	11774.1	997.4	0.07(2)		E2
37^-	12818.1	1044.0	<0.07(2)		E2
Band 7 (-,0)					
6^-	1713.5	1105.0	21.40(1)	1.32(7)	E1
8^-	1963.4	249.9	$<21.40(1)$[d]		E2
		136.0	32(2)[d]		M1/E2
10^-	2295.7	332.3	<53(3)[d]		E2

Table 5.1 – Continued

I_i^π	E_{level}(keV)	E_γ(keV)[a]	I_γ	D[e]	Multipolarity[c]
		177.0	108(11)[b]		M1/E2
12^-	2700.8	405.1	<161(25)[d]		E2
		213.0	202(31)[b]		M1/E2
14^-	3180.7	479.9	136(21)		E2
		247.0	84(13)		M1/E2
16^-	3726.3	545.6	96(15)		E2
		275.0	46(10)		M1/E2
18^-	4329.8	603.5	80(12)		E2
20^-	4985.3	655.5	35(5)		E2
22^-	5689.5	704.2	35(5)		E2
24^-	6443.0	753.5	20(4)		E2
26^-	7248.7	805.7	12(2)		E2
28^-	8109.0	860.3	11(2)		E2
30^-	9025.0	916.0	7(1)		E2
32^-	10006.0	981.0	2.8(5)		E2
34^-	11022.0	1016.0	2.2(4)		E2
36^-	12068.0	1046.0	1.7(3)		E2
Band 7 (-,1)					
7^-	1827.4	115.0	<40.8(4)		M1/E2
		(1221.0)			E1
9^-	2119.3	291.9	92(4)[b]		E2
		156.0	45(2)		M1/E2
11^-	2488.7	369.4	211(33)		E2
		192.0	312(48)		M1/E2
13^-	2934	445.3	98(15)		E2
		232.0	132(20)		M1/E2
15^-	3451.3	517.3	89(14)		E2
		269.0	70(11)		M1/E2
17^-	4037.5	586.2	46(1)		E2
19^-	4688.4	650.9	32(1)		E2
21^-	5380.4	692.0	14(1)		E2

Table 5.1 – Continued

I_i^π	E_{level}(keV)	E_γ(keV)[a]	I_γ	D[e]	Multipolarity[c]
23^-	6062.9	682.5	12.2(5)		E2
25^-	6827.9	765.0	6.8(4)		E2
27^-	7673.6	845.7	6.3(4)		E2
29^-	8573.1	899.5	2.3(1)		E2
31^-	9505.1	932.0	1.22(7)		E2
33^-	10475.1	970.0	0.71(5)		E2
Band 8 (+,1)					
15^+	3728.5	613.0	2.2(5)	1.67(9)	E2
17^+	4217.5	489.0	1.0(3)		E2
		539.0	1.4(3)	1.10(4)	E2
19^+	4806.5	589.2	1.0(3)		E2
21^+	5479.5	672.2	0.6(2)		E2
23^+	6229.5	750.5	0.4(1)		E2
25^+	7047.5	818.0	0.29(1)		E2
27^+	7923.5	876.0	0.19(1)		E2
29^+	8851.5	928.0	0.14(1)		E2
31^+	9822.5	971.0	0.11(1)		E2

[a] All energy uncertainties are within 0.6 keV.

[b] Intensity of the transition is obtained from branching ratio.

[c] Multipolarity is determined via both the intensity ratio and spin and signature arguments.

[d] Estimation of the intensity of the transition is done by summing the intensities that de-excite the level. All other band intensities are determined with respect to that value.

[e] The intensity ratio was possible to measure for only particular linking energy transitions.

* Intensity for the whole doublet is shown.

[f] Doublet.

5.1 The Level Scheme of ^{174}Hf

Prior to this work, high-spin states in ^{174}Hf have been studied extensively by Gjørup [Grp94] and earlier by Walker *et al.* [Wal83].

The ground-state band (Band 1, Fig. 5.1) has been studied previously [Wal83, Grp94], reaching a spin of $32\,\hbar$. In our work the ground band has been further extended to spin $42\,\hbar$ (Fig. 5.2). The intensity ratios for transitions within the band (Table 5.1) confirm the $E2$ nature of the radiation up to 20^+. The assignment of spins higher than this level is based on the assumption that the rotational behavior persists throughout the band. As can be seen from Fig. 5.3, the ground-state band becomes non-yrast, as the rotational band built on the β-vibration ([Eji71, Wal83]), Band 2, becomes lower in energy at spin $24\,\hbar$. The two 24^+ levels become nearly degenerate (with an energy difference of 18 keV), and linking transitions (767, 773, and 783 keV) can be observed between the two bands. At spin $30\,\hbar$ and $32\,\hbar$ two new side levels are observed to feed the ground-state band, through the 1096 and 1128 keV transitions.

Band 2 (Fig. 5.1, Fig. 5.2) was identified previously [Eji71, Wal83] and it was interpreted as a rotational structure associated with the β-vibrational mode. The band was previously known to $34\,\hbar$ [Grp94]. In this work Band 2 has been observed up to spin $40\,\hbar$, but the levels below 4^+ could not be observed due to insufficient population of the states far from the yrast line. More linking transitions to the ground-state band were added (700, 973, 292, and 1011 keV). The obtained angular correlation ratios for the linking transitions (Fig. 5.1) suggest $\alpha = 0$ signature for the band. In particular, the 700 keV transition to the ground-state band favors an $M1/E2$ character of the radiation, as its angular correlation ratio is 0.75. This suggests a spin of either 6^+ or 7^+ of the de-exciting level. However, if spin 7^+ is assigned, the 1011 keV transition to the 4^+ level in the ground-state band would require a change of three units of angular momentum. The latter case would require a much longer lifetime than that observed. Therefore, a spin/parity of 6^+ is assigned to this state. The band exhibits a cross transition at spin $24\,\hbar$ to the ground-state band, as discussed above.

Band 3 (Fig. 5.1) has been assigned as an octupole vibration, and was established [Wal83, Grp94] up to spin $39\,\hbar$. More transitions were observed feeding to the ground-state band (676, 298, and 458 keV). The transitions from levels 9^- and 11^- are observed with both $I \to I \pm 1$. All linking transitions are identified as stretched dipole type as they have an intermediate values between 0.5 and 1 (Table 5.1), and assignments of the spin values in the bands are based on these data, consistent with the previous measurements. Energy transitions below spin $I = 6\,\hbar$ could not be observed due to the states being far above the

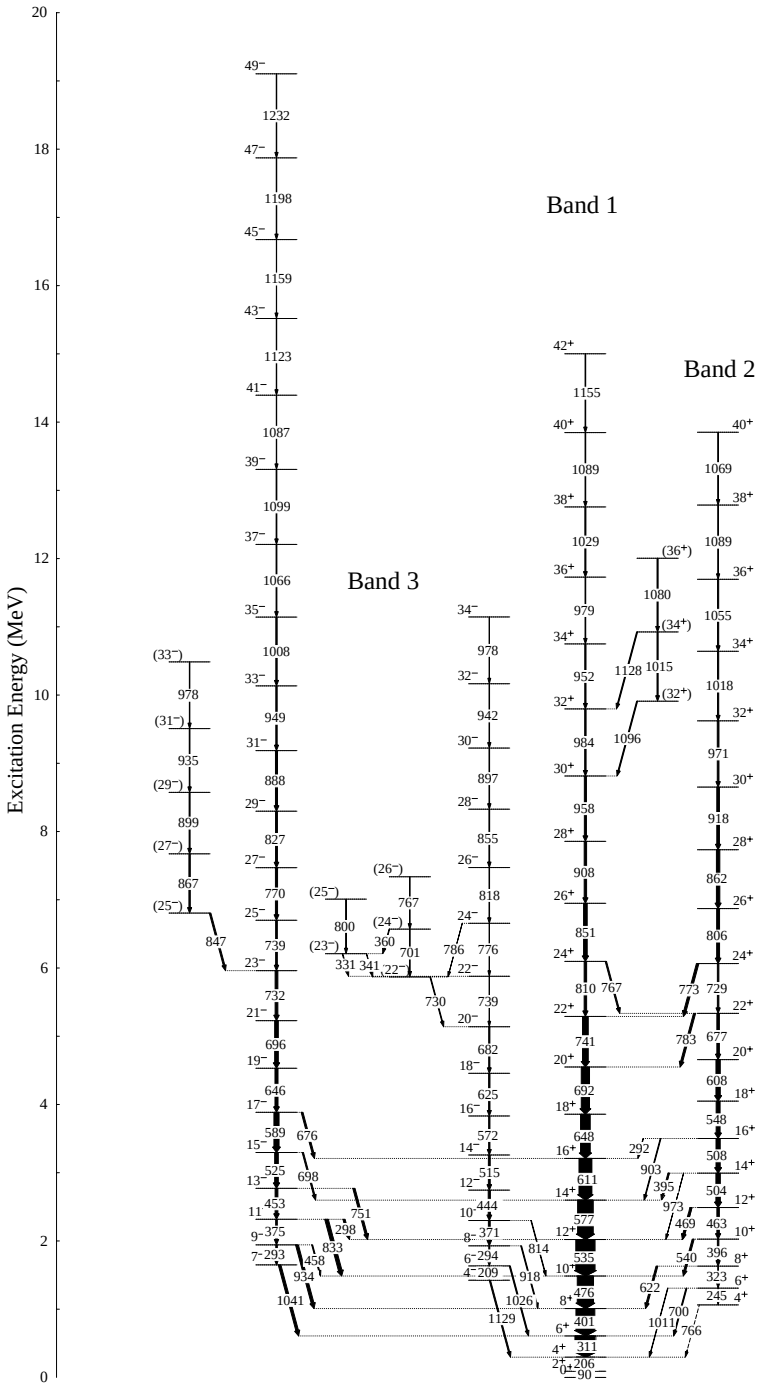


Figure 5.1: Partial level scheme of ^{174}Hf. Bands 1, 2, and 3 denote the ground-state band, the β-vibrational band, and a rotational band based on octupole vibration [Wal83], respectively.

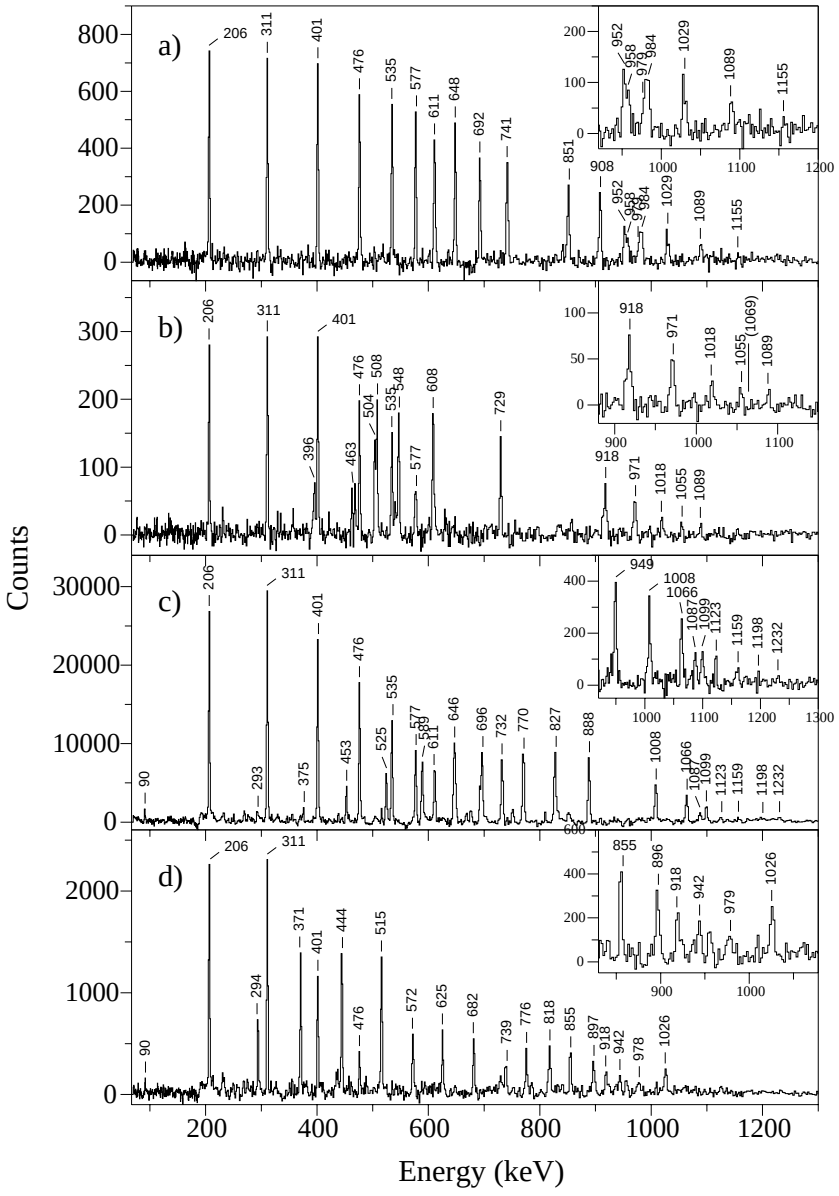


Figure 5.2: Spectra of Bands 1 and 2 and 3 obtained from GSFMA117 experiment. Spectrum a) (Band 1) is obtained by summing of triple gates, using 810 keV in all of them as a clean reference. Spectrum b) (Band 2) is obtained by single triple gating on 806 keV, 677 keV, and 862 keV. Spectrum c) (Band 3) is obtained by single double gating on 739 keV and 949 keV, using triple gating to obtain the highest spin states. Spectrum d) (Band 3) is obtained by summing triple gates within the band above 515 keV.

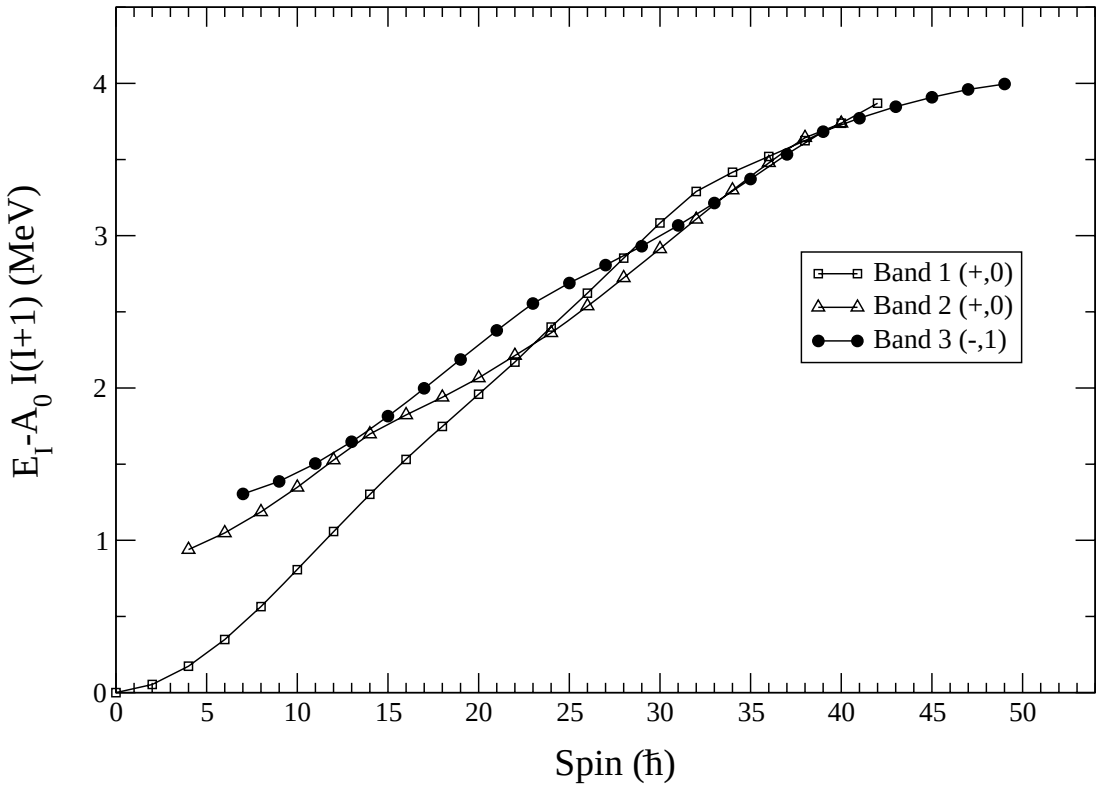


Figure 5.3: Plot of the energy of the levels as a function of spin for Band 1, Band 2, and the (-,1) partner of Band 3, subtracted by the rigid rotor value for ^{174}Hf. Band 2 becomes yrast at spin $24\,\hbar$ while Band 3 becomes lowest in energy at spin $35\,\hbar$. The constant that corresponds to a spherical rigid rotor with mass 174, $A_0 = 0.00617\,\mathrm{MeV}$, was used.

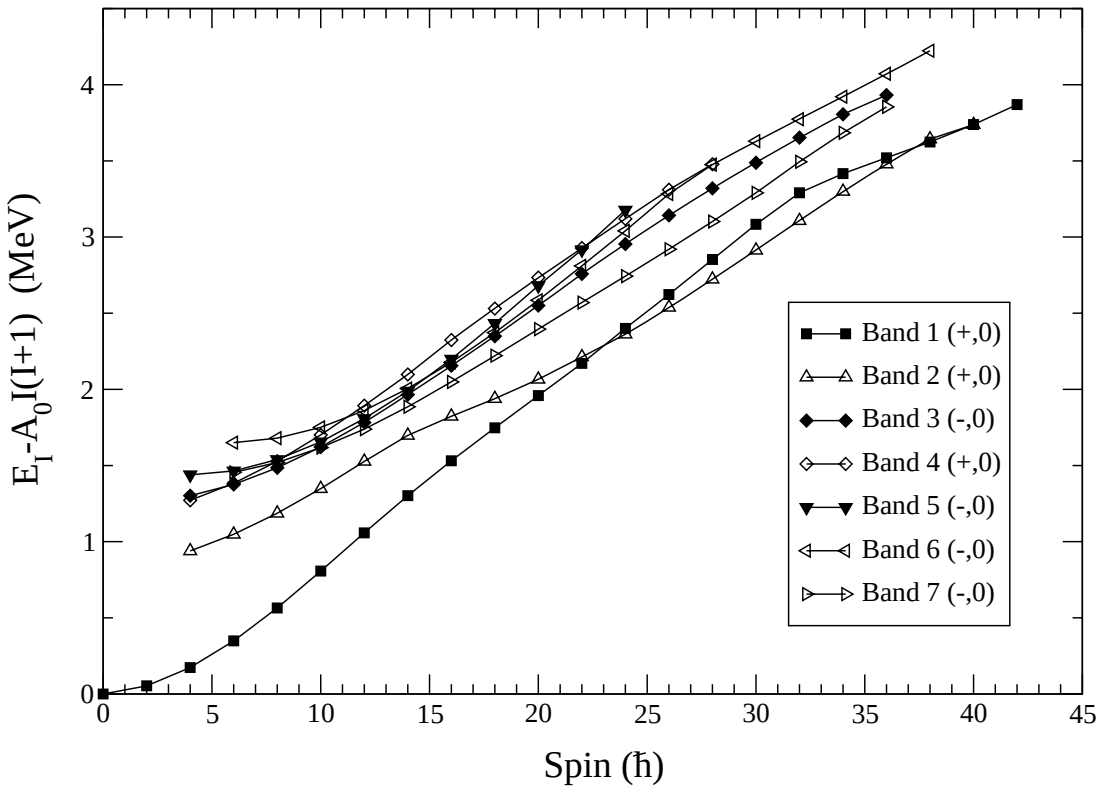


Figure 5.4: Plot of the energy of the levels as a function of spin for the zero signatures of all rotational bands. Same constant $A_0 = 0.00617\,\mathrm{MeV}$ was used.

yrast line. The (-,1) sequence becomes yrast at spin $27\,\hbar$, thus allowing it to be extended up to higher spin observed $49\,\hbar$, Fig. 5.2. A level with tentatively assigned spin and parity of 25^- is identified to feed to level 23^- in the $(-,1)$ partner of the Band 3. Four transitions were found above this level, reaching spin $33\,\hbar$. The (-,0) band was extended up to spin $34\,\hbar$. This $\alpha = 0$ signature lies higher in energy than the $\alpha = 1$ signature of Band 3, which is why it could not be extended to higher spin (Fig. 5.4). A side band is found to feed the 20^- level of the band, which exhibits characteristics of a $\Delta I = 1$ band. The spin assignments of this new structure are tentative, based on an assumption of similarity of spins and parities of the interacting levels. It should be noted that cross linking transitions in Bands 1, 2, and 3 occur around a narrow spin region of $22 - 25\,\hbar$.

The two signatures of Band 4 (Fig. 5.5, Fig. 5.6) have been previously studied [Wal83, Grp94] up to spin 24 and $25\,\hbar$. In this work an additional two transitions have been added to each sequence, extending the spin up to 28 and $29\,\hbar$, respectively. The angular correlation ratio for the 1304 keV (Table 5.1) transition is consistent with a stretched $E2$ transition, thus the assignment of a positive parity and spin $4\,\hbar$. A new linking transition (1363 keV) from

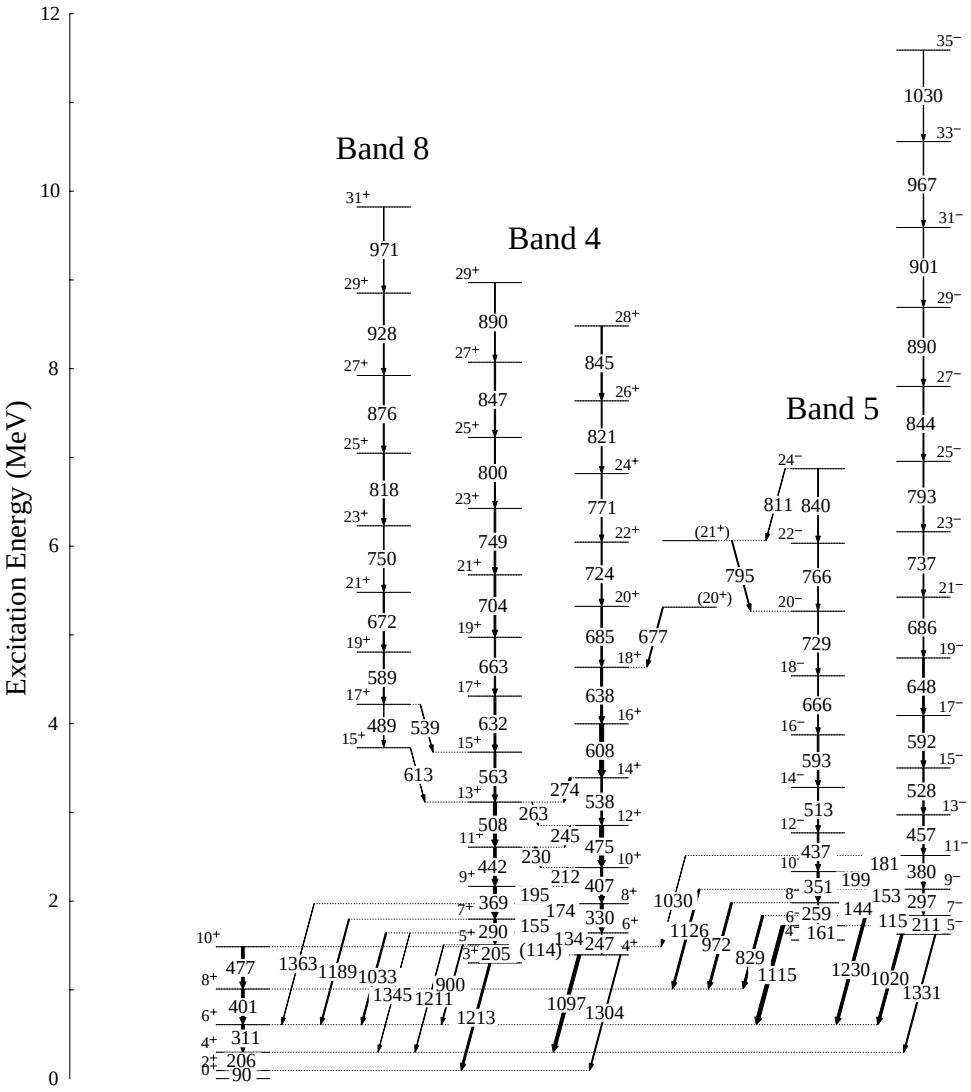


Figure 5.5: Band 4, Band 5, and Band 8 in ^{174}Hf. Shown is only a partial level scheme of the ground-state band, up to the highest level that is populated by these three bands.

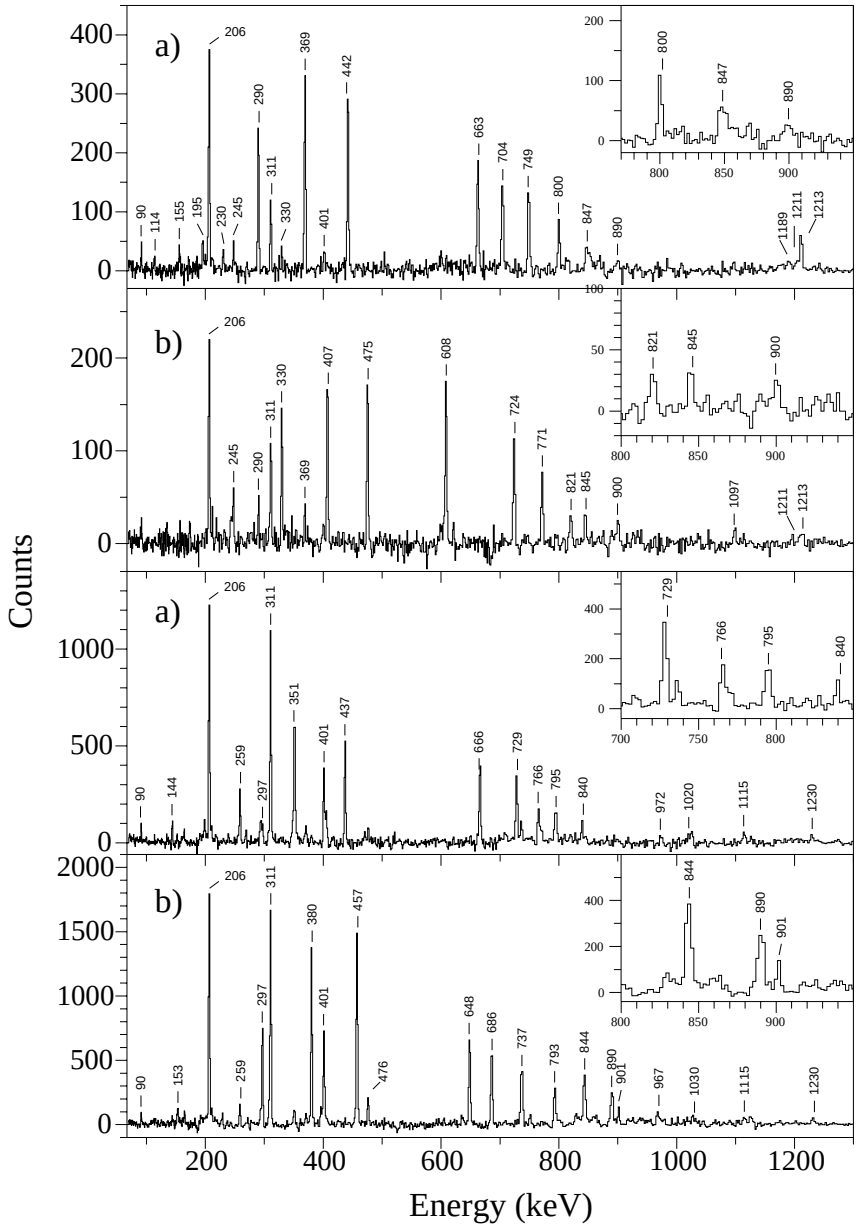


Figure 5.6: Spectra of Band 4 and Band 5 in ^{174}Hf obtained from the GSFMA117 experiment. Spectrum a) (Band 4) is produced by single triple gating on 508 keV, 563 keV and 632 keV. Spectrum b) is produced by triple gating on 538 keV, 638 keV and 685 keV. Spectrum c) (Band 5) is produced by gating on 513 keV and 593 keV, and the spectrum in panel d) is obtained by gating on 528 keV and 592 keV.

the 8^+ level to the ground-state band was added, as well as one additional $\Delta I = 1$ intraband transition (274 keV). A previously identified transition (1005 keV), $3^+ \rightarrow 4^+$, [Grp94] was not found. A side band is observed to decay to the 15^+ and 13^+ levels of the $\alpha = 1$ signature via the 613 keV and 539 keV lines. Angular correlation measurements for these transitions were not possible and thus the spin assignments of the side band are based on assumptions of mixing of the two close-lying levels (15^+) and similarity of the wave functions leading to a tentative value for the lowest level of the band of 15^+. A single level is observed to feed to the 18^+ level via the 677 keV transition, however, no rotational structure was identified above this state.

Band 5 (Fig. 5.5, Fig. 5.6) was found in previous studies [Grp94]. In the present work the $\alpha = 0$ and $\alpha = 1$ signatures were observed up to spin 24 and 35 $\hbar$, from previous spin values of 24 and 25 $\hbar$, respectively. The band has a negative parity assignment, based on the intensity ratios for the $E1$ linking transitions (Table 5.1). A single level with tentative spin assignment 22 is found to feed to level 20^- via 795 keV. Level 24^- is also found to feed to the level with spin 22. The $\alpha = 0$ signature partner could not be extended beyond spin 24 as it is highly non-yrast. As can be seen from Fig. 5.4, this signature is the highest one in energy at spin 24 $\hbar$.

Band 8 (Fig. 5.5) is observed for the first time in this work. The lowest states of this band are observed to feed the 15^+ and 13^+ levels of Band 4, via the 539 keV and 613 keV transitions, respectively. The 613 keV transition is 50 keV different from the 563 keV transition between the 15^+ and 13^+ levels in Band 4. This indicates a small interaction strength of $\sim$25 keV between the 15^+ and the corresponding level of Band 8. The observed linking transitions between both bands seem to result from accidental degeneracy of the two levels. The angular correlation ratio for the 613 keV transition is consistent with $E2$ type (Table. 5.1), as well as the 539 keV transition, which allows us to assign spin and parity of 17^+ and 15^+ for the lowest levels in Band 8. Consequently, assuming $E2$ transitions, this band extends up to spin 31 $\hbar$.

Band 6 (Fig. 5.7, Fig. 5.8) was observed in the previous studies of ^{174}Hf [Grp94], where only the $\alpha = 0$ signature was seen up to spin 26 $\hbar$. A tentative band head spin assignment was derived from the decay pattern and was estimated as $K^\pi = 6^-$. In this work the signature partners were observed up to spins 37 $\hbar$ and 38 $\hbar$. The angular correlation ratio for the newly added 995 keV transition suggests it is a transition of $E1$ type. This suggests a spin and parity of the level of 7^-, which is consistent with the previous assignment [Grp94]. Further confirmation of the parity of the band comes indirectly from the behavior of the alignment (see next Section). New transitions feeding to the ground-state band were added (1352 keV, 1041 keV, 995 keV, 261 keV, and 356 keV) as well as five $M1$ intraband transitions

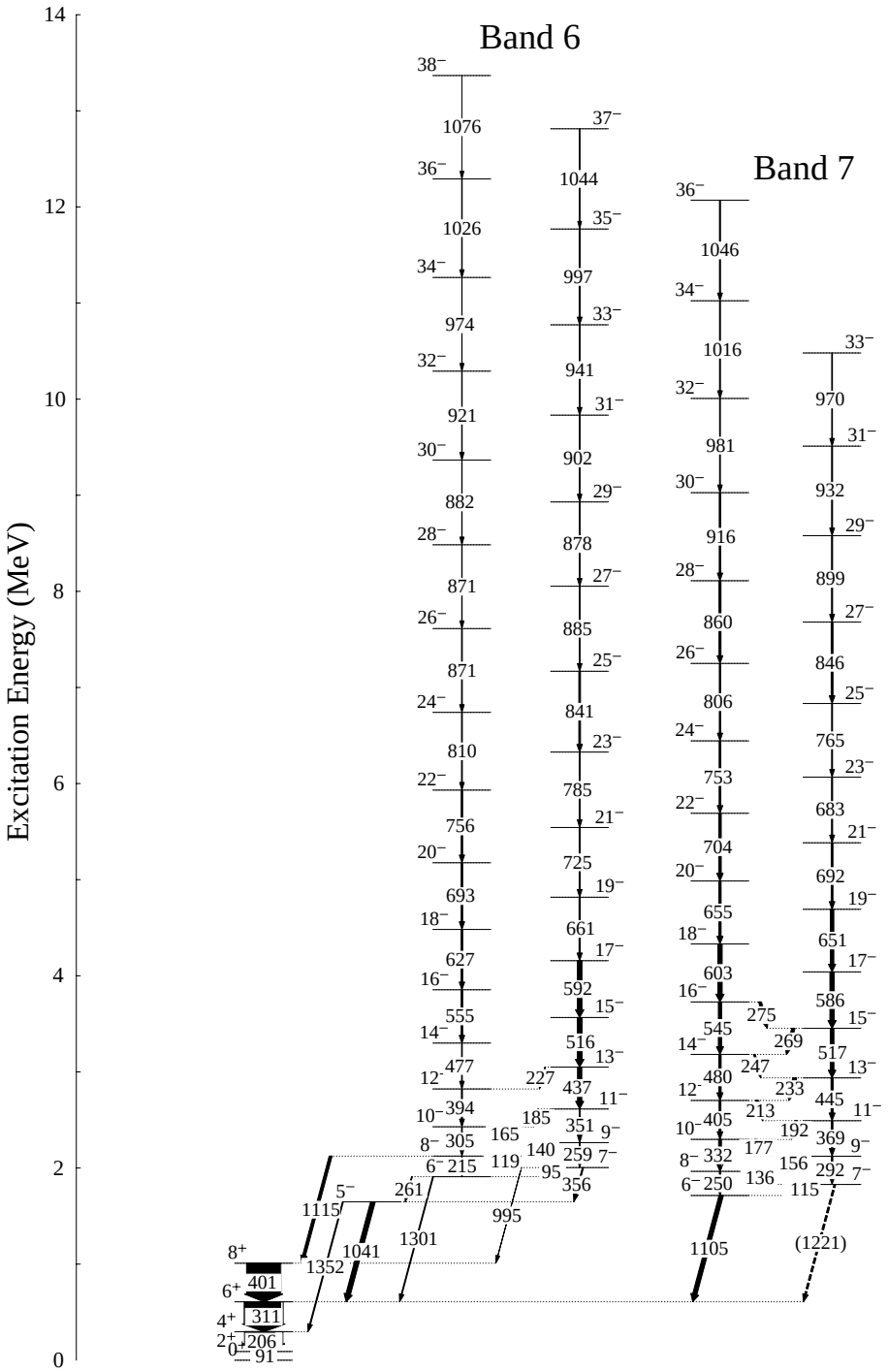


Figure 5.7: Band 6 and Band 7 in ^{174}Hf.

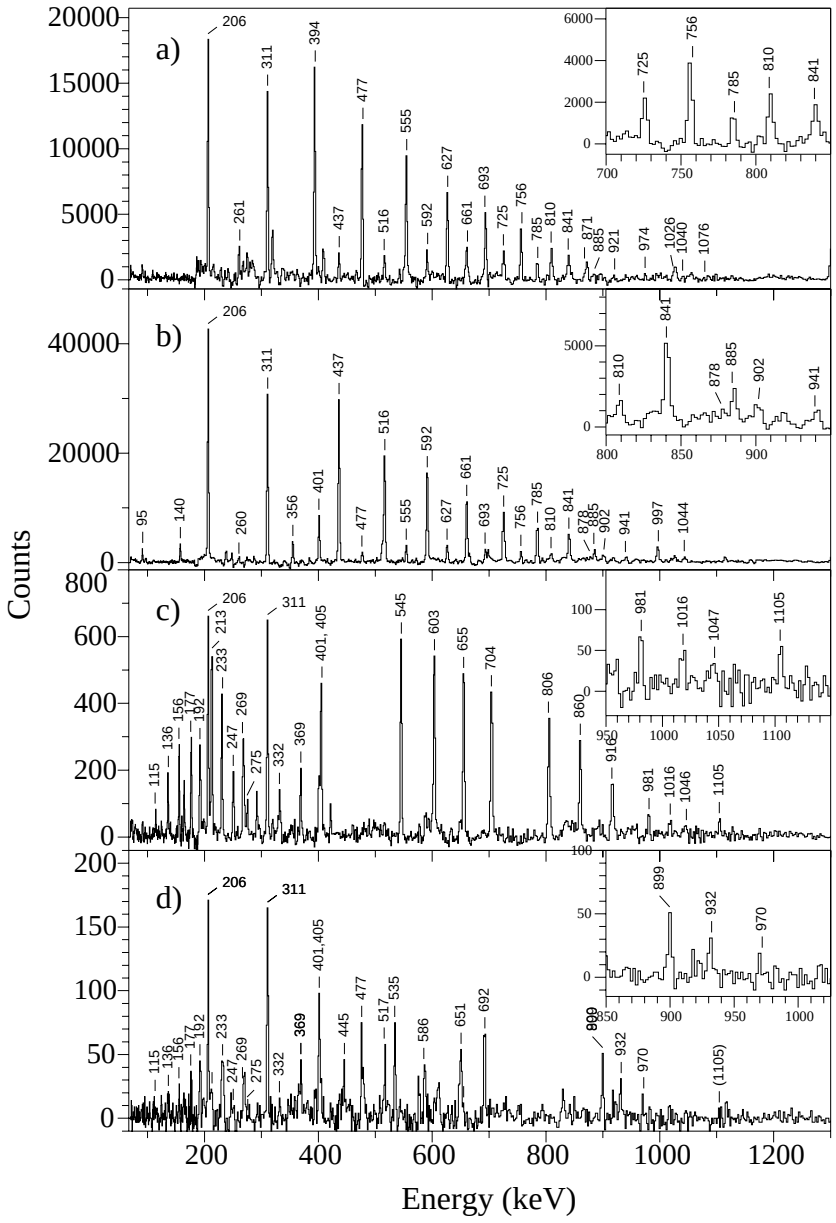


Figure 5.8: GSFMA117 data showing spectra of Band 6 and Band 7 in ^{174}Hf. The spectra a) and b) are produced by adding many gates throughout Band 6. Both signature partners are visible. Spectra c) and d) show Band 7.

(119 keV, 140 keV, 165 keV, 185 keV, and 227 keV). The linking transitions to the ground-state band are realized through the feeding of an intermediate level, with a spin/parity assignment of 5^-. This level could belong to the band, however, the 356 keV transition does not follow characteristic systematics of an in-band $E2$ transitions. The level, however, was previously identified [Wal83, Car75] in ^{174}Hf. Thus it seems to be a preferred way in the decay path of Band 6.

An additional test was performed to learn whether the 5^- level belongs to Band 6. The $B(E1)/B(E2)$ ratio (Eqn. 2.56) was extracted for the 8^- and 7^- levels for in-band $E2$ transitions and $E1$ transitions to the ground-state band. Comparable values would favor the suggestion of placing the 5^- level as a member of Band 6. The obtained values are $0.189(8) \times 10^{-10}$ fm^{-2} and $37(1) \times 10^{-10}$ fm^{-2} for levels 8^- and 7^-, respectively. Assuming comparable $E1$ strengths, we conclude that the much larger $B(E1)/B(E2)$ value for the 7^- level compared to 8^- indicates a much reduced $B(E2; 7^- \rightarrow 5^-)$ transition strength. This suggests that the 5^- level is not a member of Band 6.

Band 7 (Fig. 5.7,Fig. 5.8) has been studied before [Wal83, Grp94] up to spin 29 $\hbar$ and 30 $\hbar$, with an assigned negative parity. The band has been extended up to spin 33 and 36 in this work. The band de-excites to the ground-state band through the 1105 keV and, tentatively, 1221 keV transitions. The angular correlation ratio of the 1105 keV transition favors an unstretched $E1$ character, suggesting a spin of 6 $\hbar$ for the lowest level of the band. The intraband $M1$ transitions were identified up to level 16^-, but the previously observed $M1$ transitions could not be confirmed from the 17^- and 18^- levels. The two $\Delta I = 1$ transitions are doublets with 294 keV and 311 keV, thus obscuring their clear identification.

5.2 Discussion

In this Section the rotational alignments and Routhians of the low-K rotational bands in ^{174}Hf will be discussed. Summaries of alignment plots and Routhians are presented in Fig. 5.9 and Fig. 5.10.

5.2.1 The ground-state, β-, and octupole vibrational bands

• Band 1

The alignment of the ground-state band (Band 1) is displayed in Fig. 5.11, where it is compared with the ground-state bands in neighboring even-A Hf isotopes. It can be seen that the alignments of the ground-state bands exhibit similar behavior, namely, the first crossing is in the vicinity of 0.3 MeV. As seen from Cranked Shell Model calculations (Fig. 2.5, see also Table 2.1), the first crossing in ^{174}Hf is due to the alignment of the lowest

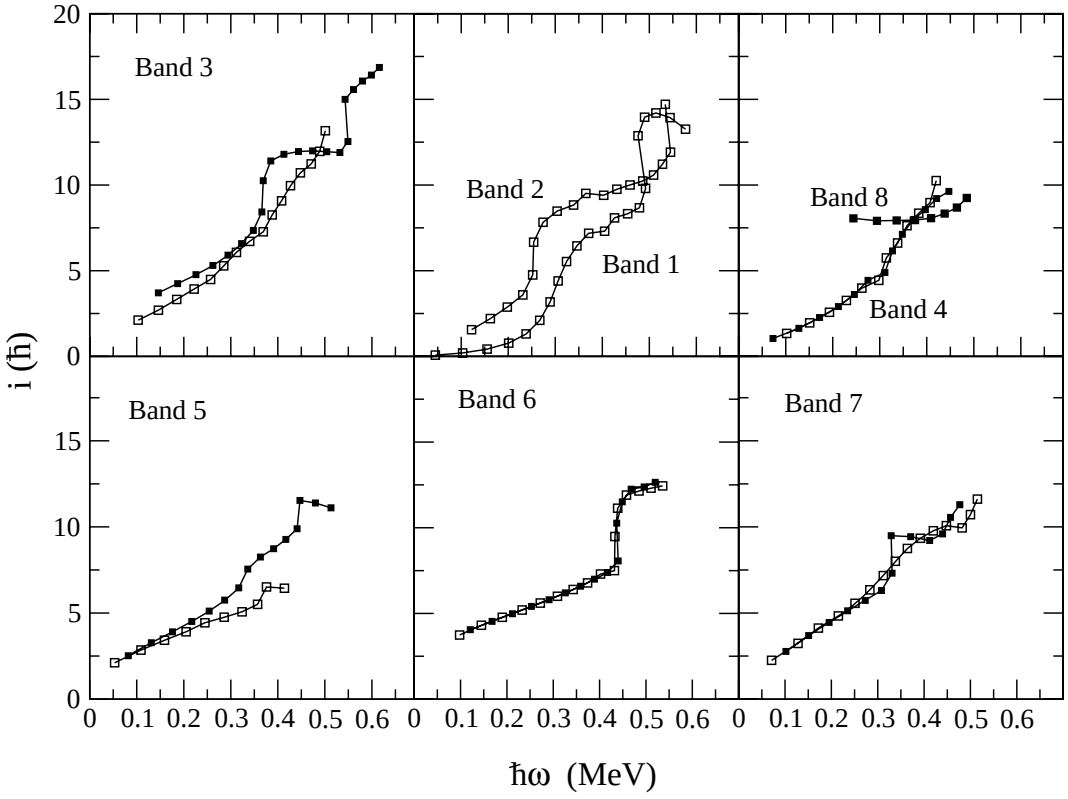


Figure 5.9: Alignments for the low lying two-quasiparticle bands in ^{174}Hf. The used Harris parameters are $\Im_0 = 31.4\ \hbar^2\,\mathrm{MeV}^{-1}$ and $\Im_1 = 52.5\ \hbar^4\,\mathrm{MeV}^{-3}$ for all bands to represent the two-quasiparticle core after the AB crossing in Band 1. The open squares denote the band partners that have signature $\alpha = 0$. The filled squares correspond to $\alpha = 1$.

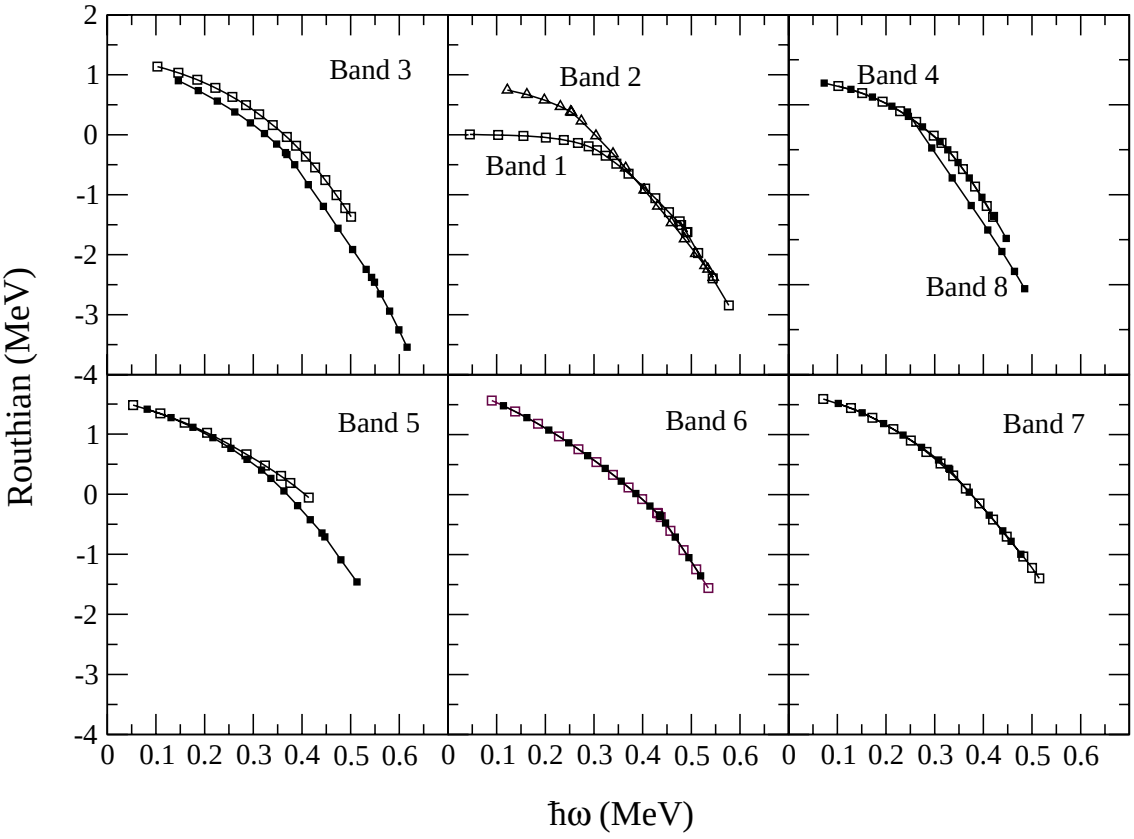


Figure 5.10: Routhians for the low lying two-quasiparticle bands in ^{174}Hf. The same Harris parameters $\Im_0 = 31.4 \ \ \hbar^2\,\mathrm{MeV}^{-1}$ and $\Im_1 = 52.5 \ \ \hbar^4\,\mathrm{MeV}^{-3}$ are used. The open squares denote the band partners that has signature $\alpha = 0$. The filled squares correspond to $\alpha = 1$.

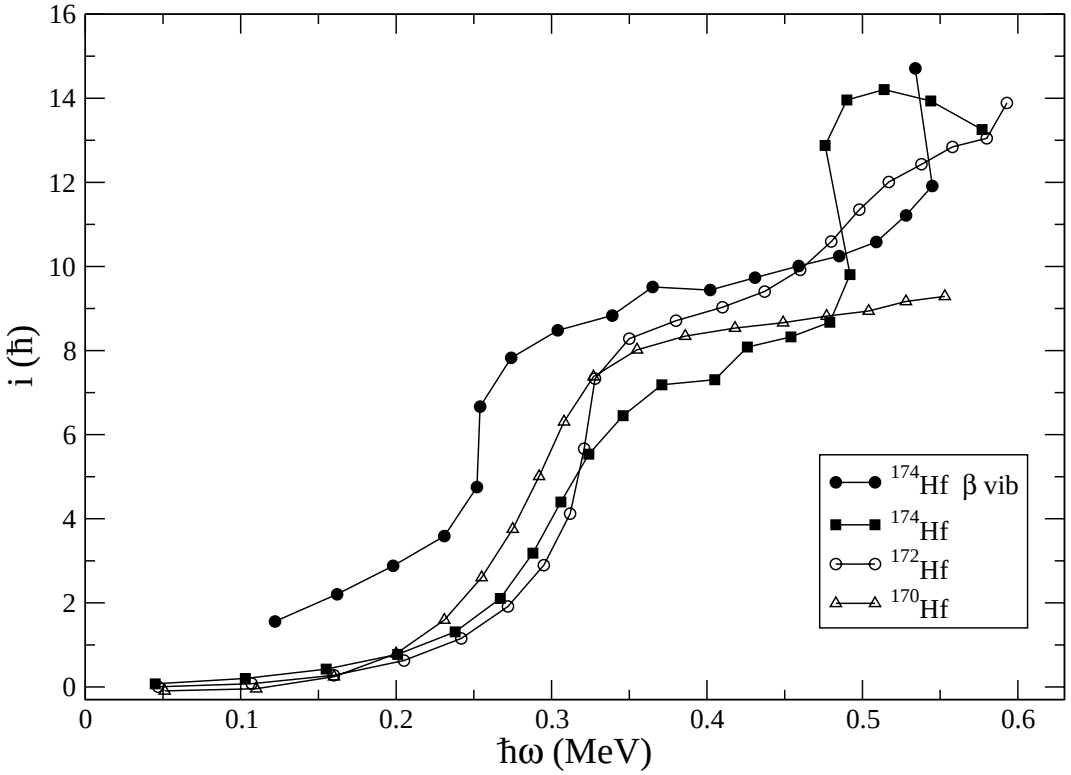


Figure 5.11: Alignment plot of ground-state bands in ^{170}Hf [Lis81], ^{172}Hf [Cul98], ^{174}Hf, and the β band in ^{174}Hf. The same Harris parameters of $\Im_0 = 31.4\,\hbar^2\,\mathrm{MeV}^{-1}$ and $\Im_1 = 52.5\ \ \hbar^4\,\mathrm{MeV}^{-3}$ were used. A reduction of the interaction strength of the first proton crossing with increase of neutron number is visible at $\hbar\omega \sim 0.5\,\mathrm{MeV}$.

quasineutron orbitals, A and B ($\nu i_{13/2}$). Thus, the first crossing for Band 1 is identified as an AB crossing. The total alignment gain of the crossing is $\sim 5.9\,\hbar$, which is in good agreement with the calculated value of $\sim 6.4\,\hbar$ (Fig. 2.5 and Table on p.105). A second crossing is observed at 0.48 MeV with an alignment gain of $5.3\,\hbar$. The calculated frequency for this crossing is 0.5 MeV, which favors an interpretation of this crossing as a proton ef ($\pi h_{9/2}$) (Fig. 2.6, Table 5.2). The crossing frequency for an alternative second neutron alignment, which would be CD in this case, lies much higher in frequency ($\hbar\omega \sim 0.6$ MeV). Thus, a crossing that comes from an alignment of quasiprotons at lower rotational frequency is favored. The ef crossing exhibits a larger alignment gain of $5.3\,\hbar$, compared to the calculated $3.3\,\hbar$. A difference between the predicted and observed alignment gains might be due to the deformation change and mixture of the quasiparticle levels at higher rotational frequencies. The deformation change should be expected since the CSM calculations are always performed at a fixed deformation. However, as the rotational frequency increases, the deformation of the core is expected to change continuously. To overcome this problem, calculations are usually done with the use of deformation parameters at a rotational frequency that is close to the value of interest.

- Band 2

Band 2 (Fig. 5.11 for alignment plot) is interpreted as a β-vibration coupled to the core ([Eji71, Wal83] and references within). The first crossing is realized at $\hbar\omega = 0.25$ MeV, slightly smaller than the ground-state band. This crossing also can be interpreted as AB. At $\hbar\omega = 0.36$ MeV, Band 2 shows a disturbance in its alignment, due to an accidental degeneracy with the 24^+ state in the ground-state band. The second crossing in Band 2 occurs at 0.54 MeV, with an alignment gain of $3.4\,\hbar$. This alignment gain is close to the calculated value of $3.3\,\hbar$ for quasiprotons, which also favors an assignment of the crossing as ef. Previous study [Grp94] of this band suggested an alternative interpretation that these crossings are a result of an interaction between the ground-state band, the β-vibrational band, the s-band (an AB configuration), and a so-called t-band, which is an aligned pair of two $i_{13/2}$ neutrons coupled to high K.

- Band 3

Band 3 was previously interpreted as an octupole vibration coupled to the core. Previous experimental studies of the lower levels of this band were done by Cardoso *et al.* [Car75], and Walker [Wal83]. A characteristic of an octupole vibration is enhanced $E1$ transitions to the ground-state band as well as forming doublets of levels with one unit difference in spin. In ^{174}Hf, this can be seen in the lowest levels in the signature partners (see Fig. 5.1). An example of a similar situation can be illustrated in works by Walker *et al.* [Wal79, Wal80] on ^{172}Yb. In that nucleus the corresponding band is observed and interpreted as an octupole

Table 5.2: Calculated initial alignments and alignment gains at the first $\hbar\omega_c$ for orbitals near the Fermi surface for ^{174}Hf. The values are taken from CSM calculations at $\hbar\omega = 0.21\,\mathrm{MeV}$ for $\beta_2 = 0.287$, $\beta_4 = -0.017$, $\gamma = -0.2^\circ$. Labels A,B,... uniquely denote both parity and signature of the orbitals, and the type of crossing.

Orbital	$i\,(\hbar)$	$\Delta i_c\,(\hbar)$, type	$\hbar\omega_c\,(\mathrm{MeV})$
ν 7/2[633] (A,B)	4.6 4.6	7.1 AB	0.3
ν 5/2[512] (E,F)	0.9 0.9		0.5
ν 1/2[521] (H,G)	1.5, 0.0		
π 1/2[541] (f,e)	2.5, 1.4	3.3 ef	$\sim 0.5^a$
π 7/2[404] (a,b)	0.0, 0.0		
π 5/2[402] (c,d)	0.0, 0.0		
π 9/2[514] (h,g)	1.4, 1.0		
π 5/2[402] (c,d)	0.0, 0.0		

[a] Approximate values are due to large interaction strength in the CSM calculations.

Table 5.3: $B(E1; I \rightarrow I-1)/B(E2; I \rightarrow I-2)$ values for levels in Band 3, level 7^- in Band 5, level 8^- in Band 6, and the octupole band in ^{172}Yb [Wal80]. Eqn. 2.56 was used to calculate the values for ^{172}Yb from data in [Wal80]. The units used for the ratio is $10^{-10}\,\mathrm{fm}^{-2}$.

level	^{172}Yb	^{174}Hf
7^-		1.12(4), Band 5, $7^- \rightarrow 5^-, 8^+$
8^-	10(3)	9.4(2), Band 3, $8^- \rightarrow 6^-, 8^+$
11^-	400(200)	166(2), Band 3, $11^- \rightarrow 9^-, 10^+$
13^-	700(400)	183(2), Band 3, $13^- \rightarrow 11^-, 12^+$
8^-		0.189(8), Band 6, $8^- \rightarrow 6^-, 8^+$

vibration [Wal79]. The range of $B(E1; I \rightarrow I-1)/B(E2; I \rightarrow I-2)$ ratios for the octupole band in ^{172}Yb is $10 - 700 \times 10^{-10}\,\mathrm{fm}^{-2}$. These values can be used for a reference in the analysis of Band 3 in the isotone ^{174}Hf. Comparative values are calculated by the use of Eqn. 2.56, shown in Table 5.3. One can see in Table 5.3 that "normal" $B(E1; I \rightarrow I-1)/B(E2; I \rightarrow I-2)$ ratios in Band 5 and Band 6 are orders of magnitude smaller. The ratios are comparable within the experimental uncertainty which indicates that the two bands in ^{172}Yb and ^{174}Hf are very similar. The observed signature splitting for Band 3, (184 keV), is close to the value of 195 keV for the signature splitting in the octupole band in ^{172}Yb. Thus, it seems plausible to identify Band 3 as a rotational band built on an octupole vibration.

It was possible to extend this band up to spin $49\,\hbar$ as it becomes yrast at spin $35\,\hbar$. The $(-,1)$ band shows a first crossing at 0.37 MeV (Fig. 5.9, Band 3) with an alignment gain of $\sim 4.7\,\hbar$. This crossing frequency is close to the predicted 0.4 MeV for a BC crossing. The identified BC crossing suggests the presence of $\nu 7/2[633]$ in the configuration of the band. A comparison can be made with other bands built on the same orbital in neighboring Hf nuclei (Fig. 5.12). The overlap of their alignments at low rotational frequency indicates similarity of their intrinsic configuration. Indeed, the rotational bands in odd-A Hf isotopes are based on an occupied single A orbital. The similar alignment of Band 3 makes the identification of this orbital plausible. A second crossing is observed at 0.55 MeV which is most likely the first alignment of the proton orbital (ef). The decrease of the crossing

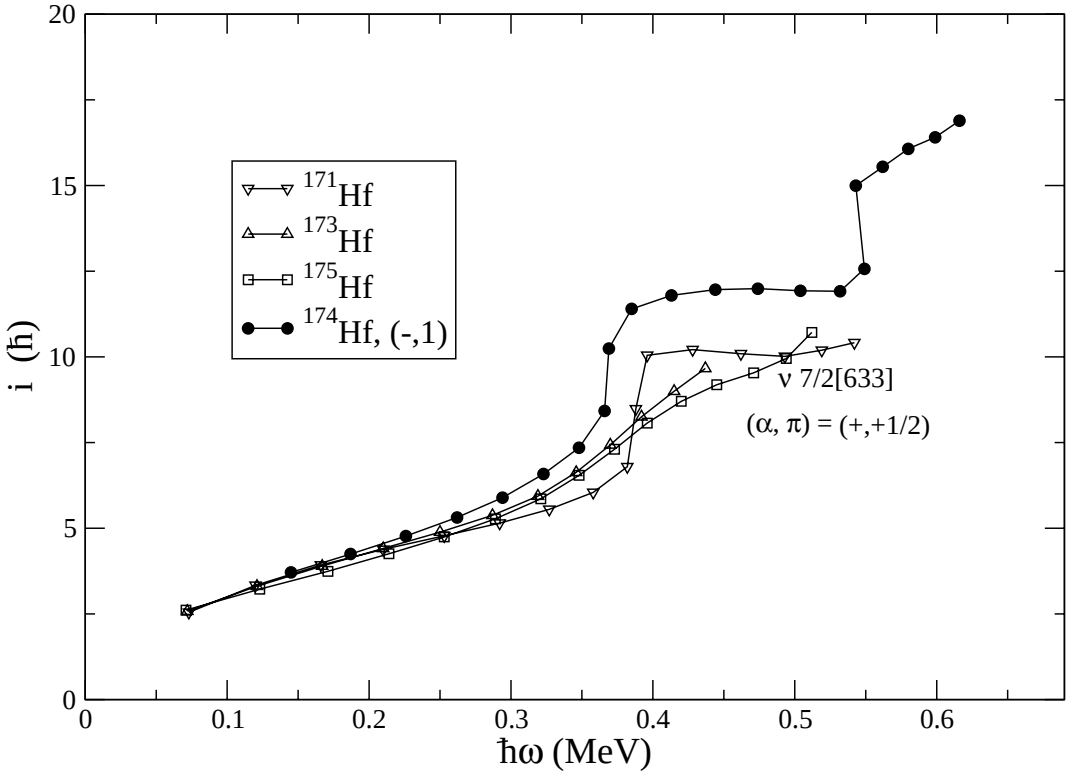


Figure 5.12: Alignment plot of (π,α)=(-,1) Band 3 in ^{174}Hf compared with alignments of the favored ($\alpha = +1/2$) signature of the $\nu 7/2[633]$ band in ^{171,173,175}Hf ([Cul00, Fab91, Cul04]). Harris parameters of $\Im_0 = 31.4\ \hbar^2\,\mathrm{MeV}^{-1}$ and $\Im_1 = 52.5\ \hbar^4\,\mathrm{MeV}^{-3}$ were used.

frequency for BC could be attributed to a reduced neutron pairing due to the occupation of a quasiparticle orbital near the Fermi level (Garrett *et al.* [Gar81]). Indeed, an occupied orbital corresponds to a broken pair of quasiparticles, which in turn reduces the available orbitals for scattering a quasiparticle pair. Even larger decreases of the BC frequencies are observed in the first crossing of Band 5 and Band 7 (Table 5.4). The $(-,0)$ signature partner was extended up to spin $34\,\hbar$. The BC crossing is also present as an upbend and there is an indication of a second crossing at $\hbar\omega \geq 0.5\,\mathrm{MeV}$ (Fig. 5.9). It can only be tentatively interpreted as an ef crossing.

Octupole bands in this mass region are described via the random phase approximation [Nee70]. In order to achieve an octupole vibration, a significant mixing among low-K orbitals is required, namely the $\nu i_{13/2}$ and $\nu f_{7/2}$ orbitals, which are near the Fermi level. This mechanism has been offered as a suitable interpretation of this band elsewhere [Grp94]. The proposed dominant configuration for the octupole band in ^{174}Hf, $\nu(7/2[633]\otimes 5/2[512])$, involves the $\nu i_{13/2}$ orbital, which gives a larger initial alignment than the ground-state band (Fig. 5.11, Fig. 5.12) and is in agreement with the comparative observation of alignments of neighboring Hf nuclei (Fig. 5.12). The BC crossing in Band 3 is explained by the presence of a dominant A orbital. The presence of signature splitting (Fig. 5.10, Band 3) can also be explained qualitatively in the similar framework of K mixing [Nee70]. The exact position of the $K = 0^-$ (odd spins only) and $K = 1^-$ (even and odd spins) octupole structures can lead to situations where large signature splitting is present. One can see in the calculations of Neergård and Vogel [Nee70] that the splitting between the lowest $\alpha = 0$ and $\alpha = 1$ states varies significantly at low spins across the rare-earth region. This suggests that situations of K coupling of orbitals to a configuration with large signature splitting are possible.

Beyond the dominant neutron configuration ($\nu i_{13/2} \otimes f_{7/2}$ [Nee70, Grp94]- AE and AF) for Band 3, it is expected that a two-proton configuration contributes to the collective nature of the octupole band. This is shown to be the case for tungsten nuclei [Nee70]. The suggestion of proton orbitals in the configuration of Band 3 is compatible with the observed ef crossing in the $\alpha = 1$ signature partner. Candidate orbitals that can be involved are $\pi h_{11/2}$ and $\pi d_{5/2}$ (ch, cg), which would not block the ef crossing ($\pi h_{9/2}$). Indeed, the $\pi 9/2[514]$ orbital lies low in energy and rotational structures built on it are observed in the neighboring ^{175}Ta [Wen96].

5.2.2 The two-quasiparticle bands

• Band 4

Band 4 experiences a crossing at 0.3 MeV for both signatures, but the second crossing is not observed completely, and a lower limit of 0.4 MeV and 0.45 MeV can be set respectively.

Table 5.4: Crossing frequencies and experimental and calculated alignment gains of low-K rotational bands in ^{174}Hf. The proposed changes in configuration are shown for each crossing. The label "ub" denotes a smooth alignment gain in the vicinity of the crossing, i.e., "upbend". The $\hbar\omega_{calc}$ and Δi_{calc} values are deduced from the CSM plot in Figs. 2.5 and 2.6.

Band	$\hbar\omega_{exp}$ (MeV)	$\hbar\omega_{calc}$ (MeV)	configuration	Δi_{exp} ($\hbar$)	Δi_{calc} ($\hbar$)
1 $\alpha = 0$	0.30	0.3	0 $\rightarrow$ AB	5.9	6.4
	0.48	0.5	AB $\rightarrow$ ABef	5.3	3.3
2 $\alpha = 0$	0.25	0.3	0 $\rightarrow$ AB	4.8	6.4
	0.54	0.5	AB $\rightarrow$ ABef	3.4	3.3
3 $\alpha = 0$	0.37	0.4	AE* $\rightarrow$ AEBC	4.7	5.7
	>0.50	(0.5)	AEBC $\rightarrow$ AEBC(ef)	>1.9	(3.3)
$\alpha = 1$	0.37	0.4	AF* $\rightarrow$ AFBC	4.4	5.7
	0.55	0.5	AFBC $\rightarrow$ AFBCef	3.5	3.3
4 $\alpha = 0$	0.30	0.3	EH $\rightarrow$ EHAB	4.6,ub	6.4
	>0.4	(0.5)	EHAB $\rightarrow$ EHAB(ef)	>1.3	(3.3)
$\alpha = 1$	0.31	0.3	FH $\rightarrow$ FHAB	4.6,ub	6.4
	>0.45	(0.5)	FHAB $\rightarrow$ FHAB(ef)	$>$ 4.7,ub	(3.3)
5 $\alpha = 0$	>0.37	(0.45)	BH $\rightarrow$ BH(AD)	>1.0	5.8
$\alpha = 1$	0.32	0.4	AH $\rightarrow$ AHBC	1.5,ub	5.7
	0.44	0.5	AHBC $\rightarrow$ AHBCef	1.7	3.3
6 $\alpha = 0$	0.43	0.3	fb $\rightarrow$ fbAB	4.6	6.4
$\alpha = 1$	0.43	0.3	fa $\rightarrow$ faAB	4.6	6.4
7 $\alpha = 0$	0.33	0.4	AE $\rightarrow$ AEBC	4.4,ub	5.7
	>0.5	(0.5)	AEBC $\rightarrow$ AEBC(ef)	>1.7	(3.3)
$\alpha = 1$	0.33	0.4	AF $\rightarrow$ AFBC	3.2	5.7
	>0.45	(0.5)	AFBC $\rightarrow$ AFBC(ef)	>2	(3.3)
8 $\alpha = 1$	>0.48	(0.5)	acAB $\rightarrow$ acAB(ef)	>1.51	3.3

* This band also has characteristics of an octupole vibration.

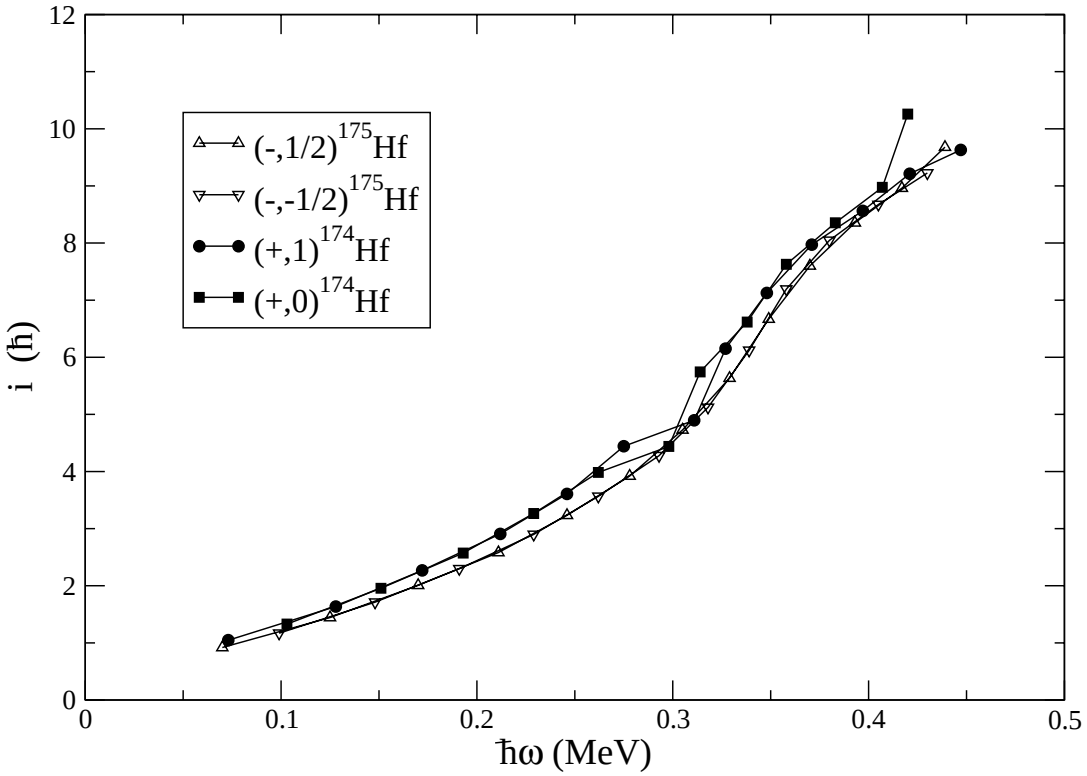


Figure 5.13: Alignment plot of both signature partners of Band 4 compared to alignment of both signatures of the $\nu 5/2[512]$ band in ^{175}Hf [Grp94].

The alignment plot of Band 4 is very similar (Fig. 5.13) to that of the $\nu 5/2[512]$ orbital in ^{175}Hf [Dra80]. This suggests the occupation of E or F neutron orbitals in the configuration. The orbital that completes the two quasiparticle configuration must be the next higher in energy above the A, B, E, and F orbitals. Calculations from the Cranked Shell Model suggest these are the signature partners of the $\nu 1/2[521]$ orbital, H and G (Fig. 2.5). Thus possible configurations for this band, observing that they form the correct signature, are EH, FH, EG, and FG. It should be noted that the $\nu 1/2[521]$ orbital experiences significant signature splitting (150 keV). However, since no signature splitting is observed in Band 4 (Fig. 5.10), it is clear that only one signature of that orbital is occupied. The lower orbital returned by CSM calculations is H. This uniquely determines the configuration of the signature partners of Band 4, EH for (+,0) and FH for (+,1), respectively.

An inspection of the data in Table. 5.5 confirms this assignment. The main argument is the comparison between the reproduced alignments as well as signature splitting. For Band 4, the expected alignment at 0.2 MeV is $2.2\,\hbar$ for both signatures, which close to the observed $1.77\,\hbar$. As the H orbital is involved in both signatures, any signature splitting

Table 5.5: Experimental alignments of the two-quasiparticle bands in ^{174}Hf at $\hbar\omega = 0.2$ MeV, compared with the sum of single-particle orbital values obtained from adjacent odd-A nuclei ^{173,175}Hf [Fab91, Cul04, Grp94] ,^{175}Ta [Wen96], and ^{173}Lu [Ven03, Fir96]. The signature splitting of the orbitals is also given. Harris parameters of $\Im_0 = 36\,\hbar^2\,\mathrm{MeV}^{-1}$ and $\Im_1 = 54\,\hbar^4\,\mathrm{MeV}^{-3}$ were used for all nuclei. Labels A, B,... uniquely denote both parity and signature of the orbitals.

Orbital	$i_{exp}\,(\hbar)$	$\Delta e'_{exp}$ (keV)[a]	
ν 7/2[633] (A,B)	3.04, 2.98	-30[b]	
ν 5/2[512] (F,E)	1.115, 1.115	0	
ν 1/2[521] (H,G)	1.085, 0.305	-150	
π 1/2[541] (f,e)	3.435, 1.770	-530	
π 7/2[404] (a,b)	0.546, 0.500	-1	
π 5/2[402] (c,d)	0.055, 0.050	1	
π 9/2[514] (h,g)	0.373 , 0.365	1	
Band	$i_{sum}\,(\hbar)$, configuration, $K^{\pi\diamond}$	$i_{exp}\,(\hbar)$	$\Delta e'_{exp}$ (keV)[c]
3 $\alpha = 0$	4.155, AE, $\underline{1}^-$, 6^-	2.64	-184
$\alpha = 1$	4.155, AF	3.50	
4 $\alpha = 0$	2.2, EH, $\underline{3}^+$, 2^+	1.77	0.7
$\alpha = 1$	2.2, FH	1.77	
5 $\alpha = 0$	4.065, BH, $\underline{4}^-$, 3^-	2.90	-27
$\alpha = 1$	4.125, AH	3.30	
6 $\alpha = 0$	3.94, fb, $\underline{3}^-$, 4^-	3.88	0
$\alpha = 1$	3.98, fa	3.89	
7 $\alpha = 0$	4.155, AE, $\underline{6}^-$, 1^-	3.65	-1
$\alpha = 1$	4.155, AF	3.60	
8 $\alpha = 1$	6.62 or 7.44, acAB or EGAB, $\underline{3}^{+e}$, 6^{+e}	6.9[d]	

[a] Denotes the signature splitting for the corresponding orbitals.

[b] All numbers in this column are obtained from the expression $e'(\alpha = +1/2) - e'(\alpha = -1/2)$.

[c] All numbers in this column are obtained from the expression $e'(\alpha = 1) - e'(\alpha = 0)$.

[◇] The possible values for K of the band heads of the bands are shown. The underlined number denotes the value for K that is consistent with observations.

[d] The initial rotational frequency for Band 8 is 0.25 MeV.

[e] The lowest value for K has been taken for the ac and EG configurations, respectively. The favored value is chosen so that the alignment plot for Band 8 is kept flat.

will be caused by the E and F orbitals. Their signature splitting, obtained as single orbital values, is 0.7 keV, which is consistent with the observed value of 1 keV.

Another confirmation for the proposed configuration of Band 4 is the lowest observed spin of the band. Given the orbitals $\nu 5/2[512]$ and $\nu 1/2[521]$, the possible couplings to a band head value K would be either 3^+ or 2^+, with the 3^+ band being lower in energy by the Gallagher-Moszkowski rule [Gal58]. The observed lowest level 3^+ is in agreement with the prediction.

A plot of the $B(M1)/B(E2)$ ratio for all two-quasiparticle bands is shown on p.115. Although such a plot can not distinguish the quasiparticle orbitals that stem from single Nilsson orbitals, it provides a confirmation on the proposed configurations at zero rotational frequency. The $|g_K - g_R|$ plot is shown on p.116. One may see the excellent agreement of the experimental ratios with that are predicted assuming the $\nu(5/2[512] \otimes 1/2[521])$ configuration.

• Band 5

The $(-,1)$ signature of Band 5 exhibits a crossing at 0.32 MeV, and a second crossing at 0.44 MeV. The first crossing could be interpreted as AB, due to the proximity of the crossing frequency to the calculated value of 0.3 MeV. However, the initial alignment of the band is similar to the alignments of the bands in neighboring Hf nuclei that have the $\nu 7/2[633]$ orbital in their configurations (Fig. 5.14). This suggests the presence of this orbital in the configuration of Band 5. Thus, the first crossing should not be understood as AB. Instead, an assignment of BC for the crossing is favored, although its expected crossing frequency is higher than the observed. It follows that the A orbital is involved in the configuration of Band 5.

The alignment of the $(-,0)$ signature partner exhibits a slight anomaly at 0.37 MeV, which can not be identified as a crossing. Instead, an examination of the level scheme (Fig. 5.5) suggests that the level with tentative spin of $22\,\hbar$ could be responsible. The interaction between the two levels pushes the 22^- level of Band 5 down, which effectively increases the alignment for one point. The case is similar to the one observed in the ground-state band and the β-vibrational band. Thus, the BC crossing for the $(-,0)$ partner is not well expressed. In addition, the $(-,0)$ partner is highly non-yrast (Fig. 5.4) and no further information could be retrieved in connection to the development of the crossing.

In this situation, it is possible to only tentatively assign a quasiparticle configuration to Band 5. The main arguments that are used are the requirements for reproducing the parity and signatures. Instead of interpreting the expected crossing as BC, an assumption of the B orbital to be involved in the configuration of the $(-,0)$ partner in Band 5 can be made. This will change the type of the expected crossing and would explain the observed delay. Using

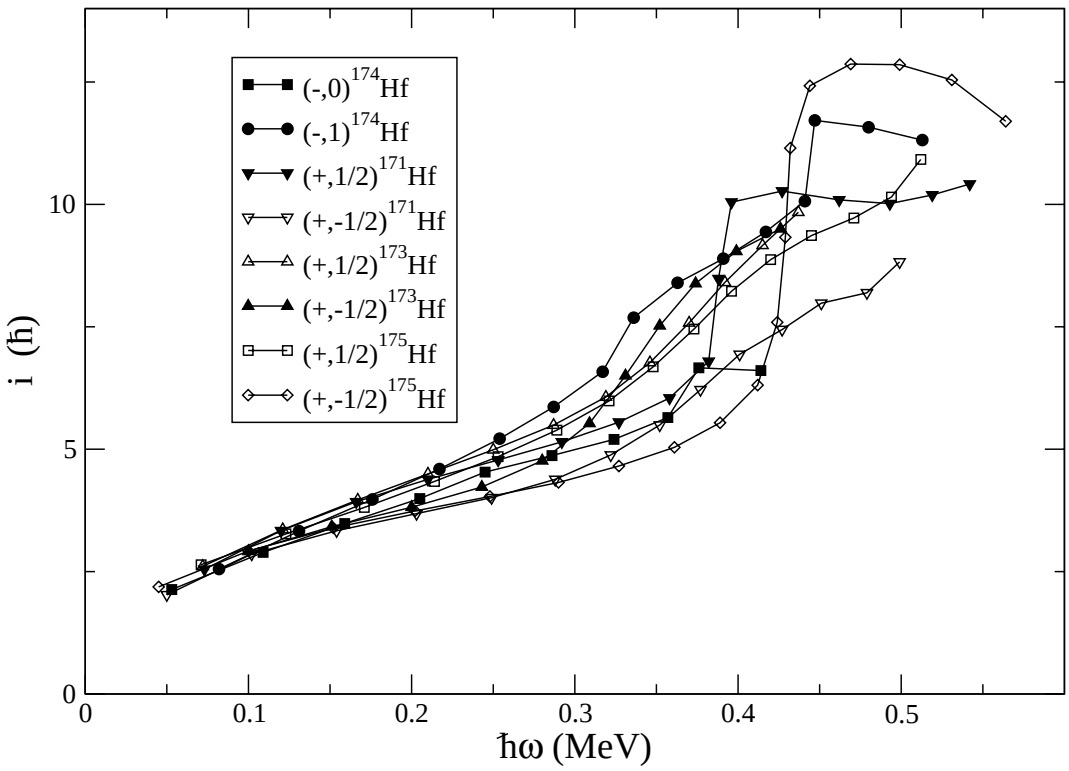


Figure 5.14: Alignment plot of both signatures of Band 5 in ^{174}Hf compared to alignment of $\nu 7/2[633]$ bands in ^{171,173,175}Hf ([Cul00, Fab91, Cul04]).

this hypothesis, and since the crossing in the $(-,0)$ partner is not observed up to 0.43 MeV, it can be interpreted as an AD crossing, which lies slightly higher in rotational frequency and is consistent with the observation of an apparent delay of the crossing. In this way we can assign the A and B orbitals to the $(-,1)$ and $(-,0)$ signature partners, respectively. The orbital $\nu 1/2[521]$ is the only one low enough in energy to reproduce the signatures for both partners. Thus, a tentative configuration of $\nu 7/2[633] \otimes \nu 1/2[521]$ is assigned, with BH for $(-,0)$ and AH for $(-,1)$ signature partners, respectively. The proposed configuration is in agreement with previously studies [Grp94].

The expected signature splitting reproduced from the single orbital values (Table 5.5) is -30 keV (defined as $e'_{+1/2} - e'_{-1/2}$), coming from the signature splitting of A and B orbitals only, as H is present in both configurations. This is consistent with the observed value of -27 keV. The configuration lower in energy is AH ($\alpha = 1$), which is in agreement with the sign of the signature splitting. The band head spin can take values 4^- or 3^-. From these, it is expected that $K = 4^-$ for Band 5, as coupling of quasiparticles with opposite spins is favored in even-even nuclei (Gallagher-Moszkowski rule, [Gal58]). The observed lowest

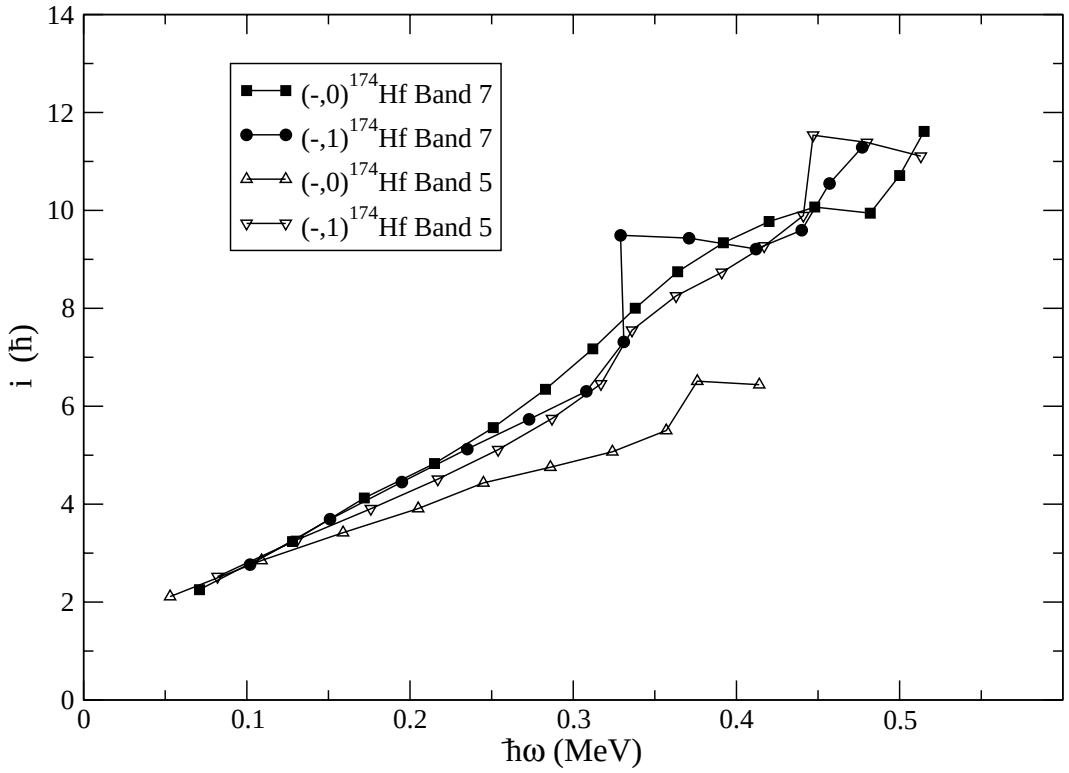


Figure 5.15: Alignment plot of both signatures of Band 7 and Band 5 in ^{174}Hf. The usual Harris parameters were used.

level 4^- is in agreement with this expectation.

- Band 7

The $(-,1)$ partner of this band has an initial alignment very similar to that of Band 5 (Fig. 5.15) and the bands built on the $\nu 7/2[633]$ orbital in neighboring Hf nuclei (Fig. 5.14). The first crossing is at 0.33 MeV, identified as BC. The second crossing for that signature partner is not fully observed but only an initial upbend, which starts at 0.45 MeV. The $(-,0)$ signature partner exhibits the BC crossing as an upbend, and a second crossing is observed to develop at 0.5 MeV. Due to the similarity of the initial alignment of both signature partners with bands that contain the $\nu 7/2[633]$ orbital, this orbital can be assigned to the configuration of Band 7. This is consistent with the observation that no AB crossing is observed at 0.3 MeV. Signature splitting is also not present in Band 7. Thus, the $\nu 5/2[512]$ orbital, which is lowest in energy above the $\nu 7/2[633]$, could be a suitable candidate for completing the configuration of Band 7.

The proposed configuration is thus AE and AF for (-,0) and (-,1) partners, respectively. The calculated alignment gain for the expected BC crossing is $5.7\hbar$, compared with the

observed 4.4 $\hbar$ for (-,0). For the $(-,1)$ partner the observed alignment gain is 3.2 $\hbar$.

The signature splitting in Band 7 is expected to arise from the single orbital values for E and F orbitals. As we saw in the case of Band 4, the experimental signature splitting for these orbitals is 0 keV (Table 5.5). The observed signature splitting for Band 7 is 1 keV, which confirms the AE, AF assignment.

The band head spin for Band 7 can take values of 1 or 6. From the proposed configuration, it is expected that coupling to $K = 6$ would be favored. This is the lowest observed level in this band.

• Band 8

Band 8 starts with a large initial alignment of 6.9 $\hbar$ (Fig. 5.9, Table 5.5). At a rotational frequency of 0.48 MeV, the band exhibits the beginning of a crossing, which can be associated with the first proton ef crossing (expected at 0.5 MeV). The large initial alignment suggests that Band 8 is not built on a two-quasiparticle configuration. Rather, a configuration of four quasiparticles would be favored as an interpretation.

Since the ef crossing is observed to start developing at 0.48 MeV, it is clear that neither the e nor f orbitals are involved in the configuration of this band. On the proton side, the lowest energy orbitals, different from e and f, are $\pi 7/2[404]$ (a,b) and $\pi 5/2[402]$ (c,d). However, they do not have the alignment needed to reproduce the observed value (Table 5.5). This suggests the presence of at least two neutron orbitals. The lowest in energy configuration would be an AB. Chosen this way, it would carry an initial alignment of 6.02 $\hbar$, which takes into account a large part of the initial alignment of Band 8. To complete the configuration, another pair of orbitals must be added, either neutrons or protons.

An inspection of Table 5.5 shows two such possible configurations, ac or EG. An ac configuration is lowest in energy and has a positive parity and $\alpha = 1$. The c orbital is assumed to be low in energy, following the work on ^{175}Ta [Wen96]. A configuration of acAB would contribute 6.62 $\hbar$ of alignment, which is comparable with the observation. An EG configuration would also reproduce the correct parity and signature, with a total alignment for EGAB configuration of 7.44 $\hbar$.

The spin of the band head K is expected to be contributed by the ac or EG configurations. The AB configuration would not contribute with angular momentum, as the quasiparticles occupy time-reversed orbitals. For ac and EG orbitals, the coupling lower in energy is the one with values for $K = 3$ or 6, respectively.

Unfortunately, the $\alpha = 0$ partner in Band 8 is not observed. This is surprising, since with its possible configuration, bcAB or FGAB, the $\alpha = 0$ signature is expected to lie near in energy to the $\alpha = 1$ component. A possible explanation is that the experimental conditions affect the population of these structures. Support for the latter is an observation

on the feeding mechanism of the $\alpha = 1$ partner to Band 4, suggesting that this highly non-yrast band is observed due to chance degeneracy of their levels.

- Band 6

Band 6 is newly discovered in the previous studies of ^{174}Hf [Grp94]. Only one signature was observed, up to spin $26\,\hbar$, which did not allow the observation of any crossing. A tentative band head spin assignment was derived from the decay pattern and was estimated as $K^\pi = 6^-$. In this work, the other signature partner has been identified and a complete crossing has been observed at 0.43 MeV, with an alignment gain of $4.6\,\hbar$. The crossing develops via an 872-keV doublet and the band extends up to spin $38\,\hbar$ (Fig. 5.7). Apart from the direct decay to the ground-state band via 1301, 995, and 1115 keV transitions, an intermediate level with tentative spin assignment of 5^- is involved in the decay path.

It is striking that the alignment plot of Band 6 is very similar to the $\pi 1/2[541]$ orbital in ^{173}Lu (Fig. 5.16). The $h_{9/2}$ orbital is an intruder for this mass region with high-j and low K, thus it will have a large alignment as seen from CSM calculations (Fig. 2.6, Table 5.2). The observed large initial alignment of Band 6 suggests the $h_{9/2}$ proton is involved in its configuration. In particular, the $\alpha = +1/2$ signature is energetically favored over its partner. Thus, the f proton is likely responsible for both sequences of Band 6. identified in the configuration of Band 6.

The parity of the band has been assigned using the angular correlation ratio method (Section 5, see also Table 5.1) employing the data obtained from the thick target experiment. The 995 keV and 1041 keV transitions linking Band 6 to the ground-state bands have ratios that suggest pure dipole character. Thus, they are likely $E1$ in nature which determines negative parity for Band 6. This is in agreement with the previous conclusions derived from the observation of the decay pattern [Grp94]. Both signature partners experience a crossing at 0.43 MeV, which is higher than the frequency of the BC crossing. The lack of signature splitting also carries information on which orbitals couple to the $h_{9/2}$ proton. The CSM calculations for protons (Fig. 2.6) provide a picture of the placement of the orbitals around the Fermi surface. The possible orbital configurations that reproduce the negative parity of the signature partners of the band are fa and fb. The orbitals next highest in energy, c and d (stemming from the $\pi 5/2[402]$ orbital), do not seem likely to contribute to the configuration. Firm proof for the latter comes from the $B(M1)/B(E2)$ ratios (Fig. 5.17) and $|g_K - g_R|$ values (Fig. 5.18). The plots in Fig. 5.17 do not provide a clear distinction between quasiparticle levels, since transitions probabilities are determined in the laboratory reference frame. However, the $B(M1)/B(E2)$ ratio allows one to distinguish between the orbitals at zero rotational frequency. It can be seen from Fig 5.17 that (fa, fb) is favored

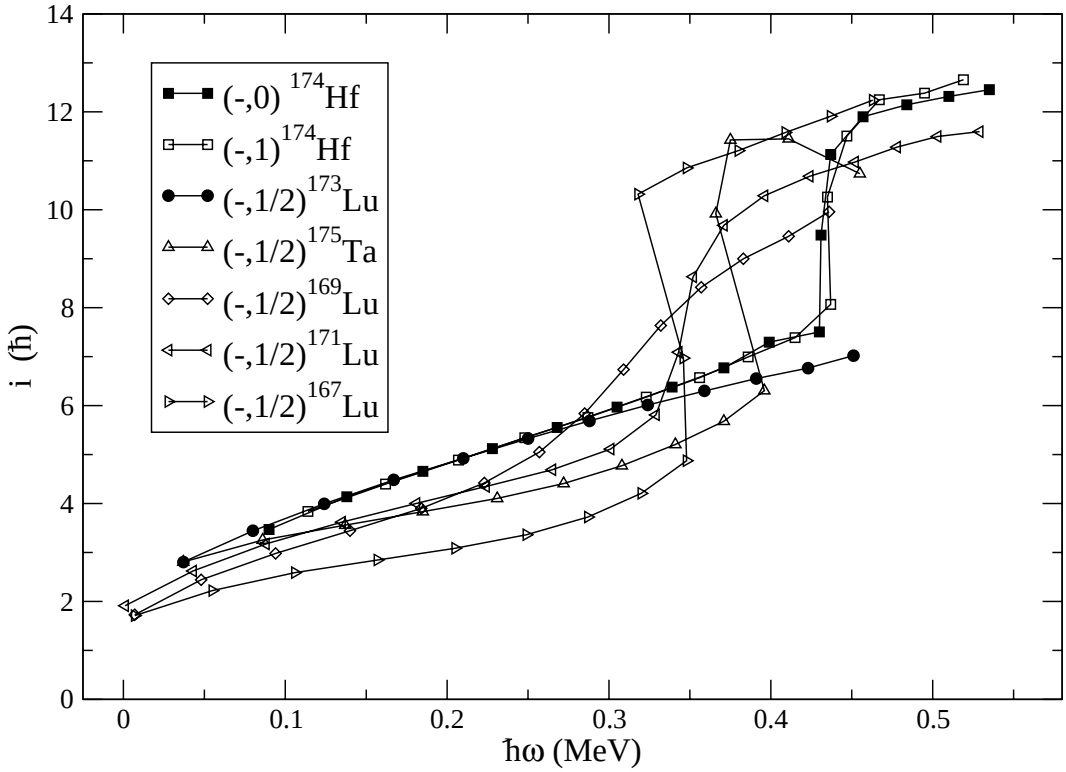


Figure 5.16: Alignment plot of the favorite signature of Band 6 compared to alignment of $\pi 1/2[541]$ in ^{173}Lu [Ven03], ^{175}Ta [Wen96], ^{169}Lu [Oga93], ^{171}Lu [Bar98], and ^{167}Lu [HYu90].

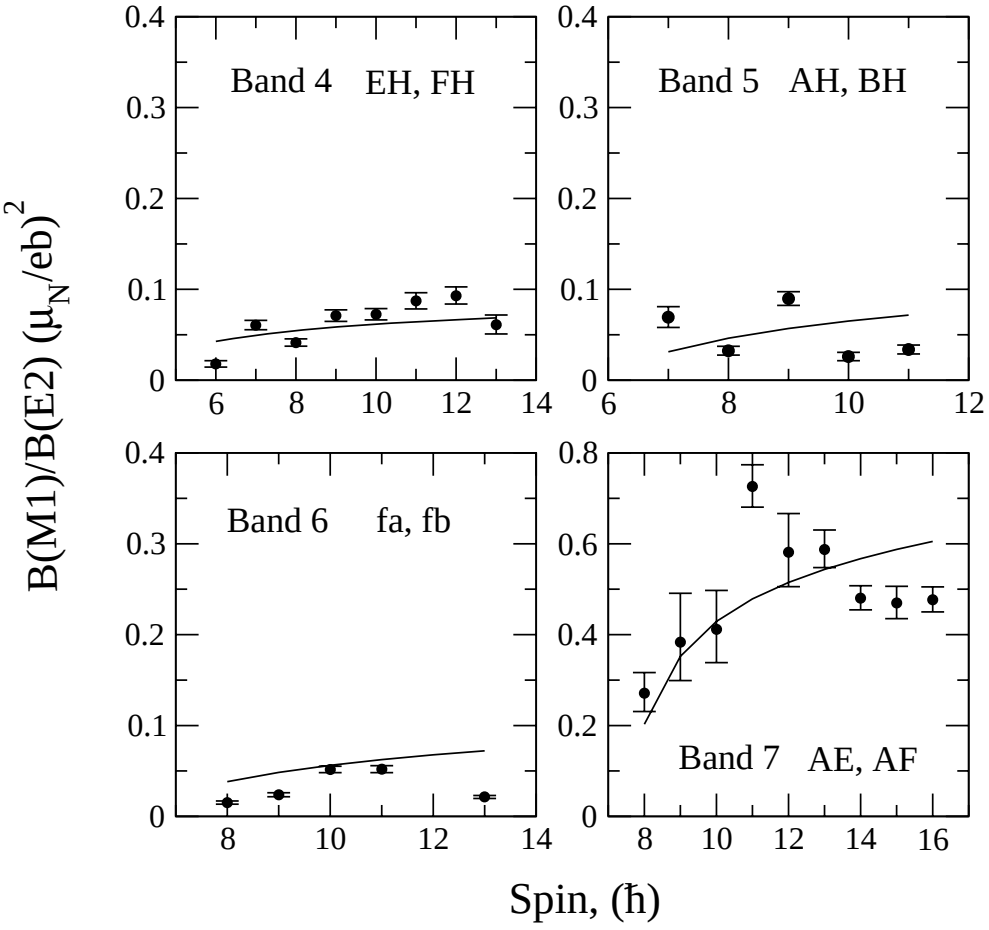


Figure 5.17: $B(M1)/B(E2)$ ratios deduced from the observed branching ratios for the two-quasiparticle bands along with the theoretical estimation based on the rotational model. Error bars are also from error propagation in the used formula.

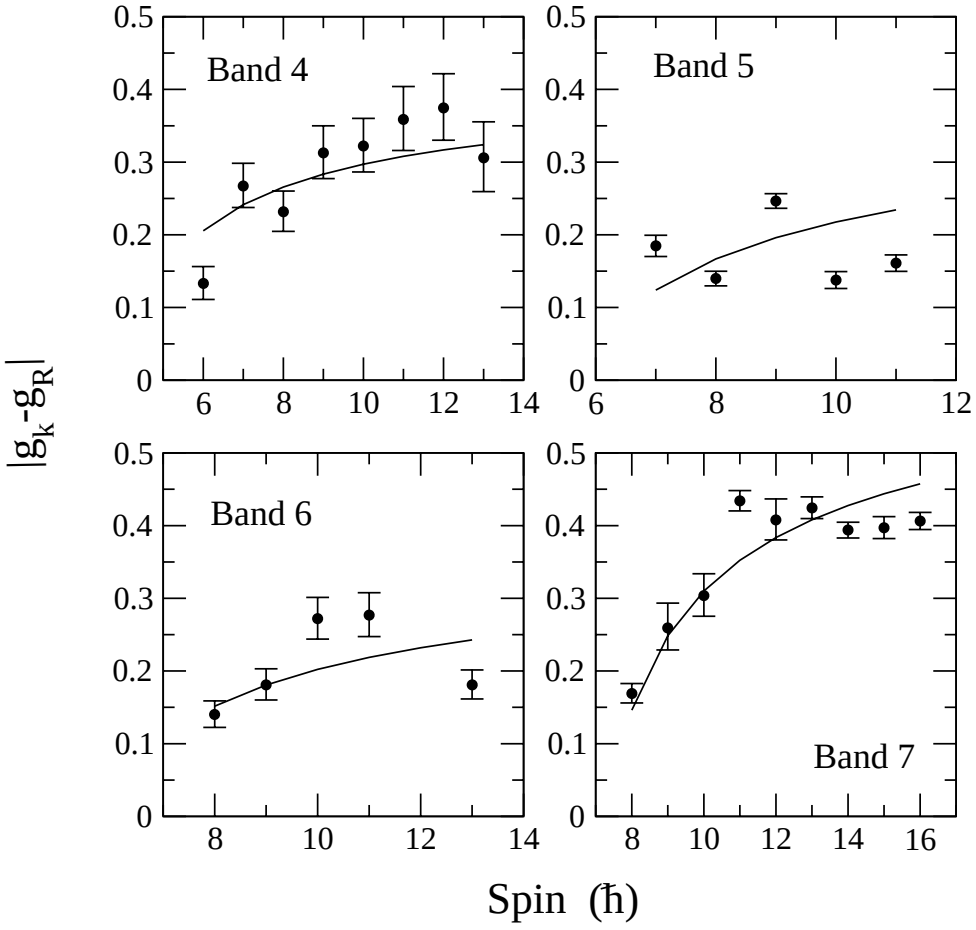


Figure 5.18: The $|g_K - g_R|$ value for the two-quasiparticle bands in ^{174}Hf along with theoretical calculations. The fits are based on the same configurations as in Fig. 5.17. The main contribution to the width of the error bars is the error propagation within the used formulas, starting from the initial uncertainties in the energies.

rather than (fc, fd). No other bands have been observed in ^{174}Hf that have similar behavior, which can indicate that Band 6 is the lowest two-quasiproton band in energy. Thus, an initial configuration of fb and fa for (-,0) and (-,1) signature partners can be assigned for Band 6, respectively. The signature splitting for this band is contributed by the a and b orbitals. The single orbital values (Table 5.5) give a signature splitting of 1 keV, and the observed one is even lower, 0 keV. This supports the proposed configuration. Using the same orbitals, the observed lowest level with spin value of 6 is consistent with the expected values for the K value of 3 or 4. In addition, the observed alignment is reproduced very well, with largest deviation from the experimental values of less than $0.06\,\hbar$.

The favorite value for K is expected to be 3. This leaves a possibility that the 5^- level could be a part of the rotational band. However, as mentioned earlier, the systematics for the $E2$ transitions in the $\alpha = 1$ partner do not favor an increase in the energy of the transition between the 7^- and 5^- levels. An additional test for the $B(E1)/B(E2)$ ratio was done for levels 8^- and 7^- (p. 97). It also disfavors the suggestion that the observed level 5^- is part of this band.

The first crossing for Band 6 is expected to be AB. However, there is a significant delay of 0.13 MeV from its predicted crossing frequency of 0.3 MeV. The same situation is observed in ^{173}Lu, where the $\pi 1/2[541]$ band does not exhibit a crossing up to 0.45 MeV [Ven03]. The delayed crossing in bands built on the $\pi 1/2[541]$ orbital is a long standing problem. The understanding of such an effect requires a thorough consideration of the evolution of the deformation of the core as well as the strength of the residual interaction between protons and neutrons [Sat93]. A residual p-n interaction means additional coupling between proton and neutron orbitals, which would then alter their relative placement. In the case of a pure neutron initial configuration (see Table 5.2), however, the variations of the crossing frequencies are not very large, considering the uncertainty of their determination due to mixing and variation of the interaction strength. In the case of the configuration of Band 6, the shift in crossing frequency is significant and thus it should be understood in different terms.

The properties of the $\pi h_{9/2} 1/2[541]$ orbital have been studied extensively ([Jen01] and references within). Different theoretical treatments, including Cranked Shell Model or Projected Shell Model [Sun94], can be used. Experimentally, the main approach is to extract the size of the interaction matrix elements between the relevant proton and neutron orbitals by comparison of Routhians of odd-odd and even-even bands with the expected Routhian obtained by summing the constituent proton and neutron orbitals ([Fra84], [Rev99]). Knowing these interaction matrix elements, one can then calculate the expected delay in the crossing frequency. This method seems to work best in odd-odd nuclei (see e.g. [Rev99]), since the

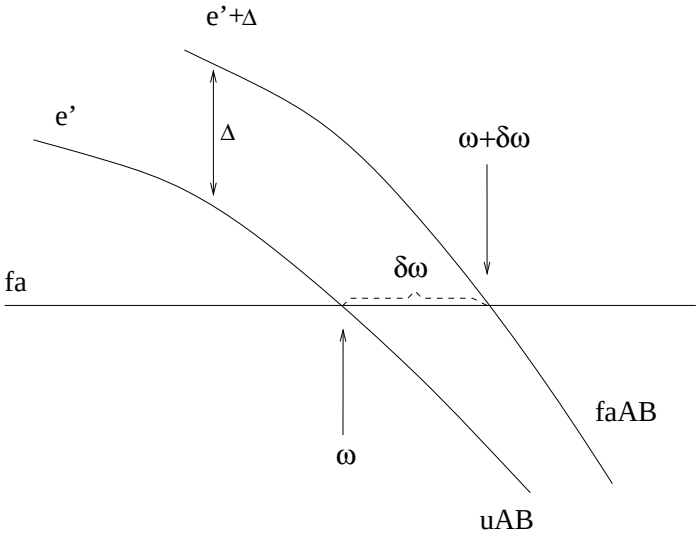


Figure 5.19: Illustration of the effect of the residual interaction on the crossing frequency.

effects of p-n interaction are observed directly from the behavior of the rotational bands.

A simple illustration of the effect is shown on Fig. 5.19. Given an unperturbed orbital uAB and an orbital fa that crosses with it, their relative placement changes, if a residual interaction Δ is assumed. This change immediately leads to a shift of the crossing frequency.

In this work a similar attempt was made to reproduce the shift in the AB crossing for Band 6, employing this method of estimation of the corresponding residual interaction matrix elements. For the proposed configuration change fa $\rightarrow$ faAB, there are four matrix elements, namely V_{fA}, V_{fB}, V_{aA}, and V_{aB}. The Routhians of single particle f, a, A, and B orbitals in $Z \pm 1$ (^{173}Lu [Ven03], ^{175}Ta [Wen96]) and $N \pm 1$ (^{173}Hf [Fab91], ^{175}Hf [Grp94]) neighboring nuclei were averaged at a crossing frequency of 0.2 MeV. The sum of the averaged values were summed with twice the estimated pairing energy in the central nucleus (^{174}Hf) and then compared with the Routhians of its two-quasiparticle bands at the same frequency. The pairing energy was derived from TRS calculations for a vacuum configuration, since the difference in pairing was found to be small for different two-quasiparticle configurations. The difference between the Routhian values is assumed to account for the residual interaction matrix elements. Then the shift of the crossing frequency is estimated to be

$$\delta\hbar\omega_c = \frac{V_{fA} + V_{fB} + V_{aA} + V_{aB}}{i_{AB}}, \tag{5.1}$$

where i_{AB} is the alignment gain in the crossing.

Unfortunately, such an approach did not bring fruitful results. The obtained shift turned out to have an unphysical negative value. The situation can be understood if one considers

the approximations that are used. In general, the residual interaction could be quite different in adjacent nuclei, thus an averaging over the experimental Routhians does not guarantee the correct value for the center nucleus. Pairing provides another source of approximation. Although it can be estimated at zero rotational frequency (static pairing), its evolution with rotational frequency is entirely model-based.

The delay in the crossing frequency can be also attributed to the change of deformation of the core. Earlier studies focused on deformation as a primary cause [Fra81a]. Examples of further studies in the rare earth region are ^{169}Lu [Oga93], ^{157}Ho [Gas90], and ^{161}Tm [War95]. The most complete survey on the $\pi h_{9/2}$ orbital is given in [Jen01]. Together with the residual interaction, it has been proposed that higher deformation could account for the delay of the AB crossing frequency in $\pi h_{9/2}$ bands (^{174}Ta, [Bar98a, Sat93]). In the case of Band 6 in ^{174}Hf, it is also of interest to estimate the extent to which deformation affects the delay in the AB crossing.

The approach to this problem was to use TRS calculations. They were performed for the quasiparticle configuration that is identified in this band, namely af and bf. In this way, the evolution of the energy surface that keeps the configuration unchanged is traced up to the region where the AB crossing occurs. The deformation parameters obtained from TRS calculations near the experimental crossing frequency (a value of 0.374 MeV was used) were then used in CSM model calculations to observe the shift of the AB crossing frequency. Results from TRS for both configurations are shown in Fig. 5.20. A primary indicator for deformation is the parameter β_2. To obtain a direct comparison with experimental quadrupole moments, the following equation was used [Ben90]:

$$Q_t \; = \; 0.0133 Z A^{2/3} \epsilon_2 (1 + \frac{\epsilon_2}{2}) \cos(\gamma + 30^\circ) \quad (eb), \tag{5.2}$$

where ϵ_2 is related to β_2 via Eqn. 2.4.

Using the β_2 parameter in Fig. 5.20 for the af configuration, we get $Q_t \sim 8.7$ eb for the deformation of Band 6. This value is higher than the value for the ground-state band ($Q_t = 7$ eb). However, the resulting CSM plot for this deformation does not show a shift in the AB crossing frequency (Fig. 5.21). Similar results emerge when the bf configuration is considered. The corresponding quadrupole moment is $Q_t \sim 7.4$ eb, which is expected to not to have any influence on the shift of the AB crossing. It is clear that TRS calculations do not yield the amount of deformation needed to account for the observed shift in the AB crossing frequency in Band 6.

However, we can take a different approach and calculate how much deformation is needed to explain the shift of crossing frequency in Band 6. The CSM plot of Fig. 5.22 shows that an enhanced $\beta_2 = 0.35$ gives a large enough shift in the AB crossing frequency. In this case

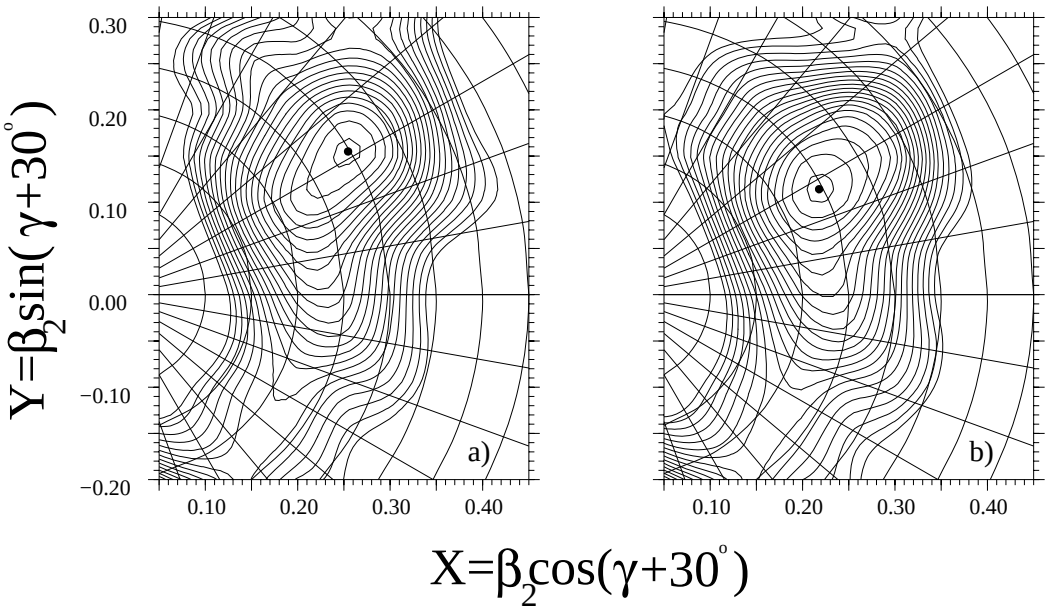


Figure 5.20: TRS calculations for ^{174}Hf for a) af and b) bf configurations at $\hbar\omega = 0.347\,\mathrm{MeV}$. The corresponding deformation parameters are $\beta_2 = 0.298$, $\beta_4 = -0.018$, $\gamma = 1.3^\circ$ for af, and $\beta_2 = 0.257$, $\beta_4 = -0.030$, $\gamma = 1.3^\circ$, for bf, respectively.

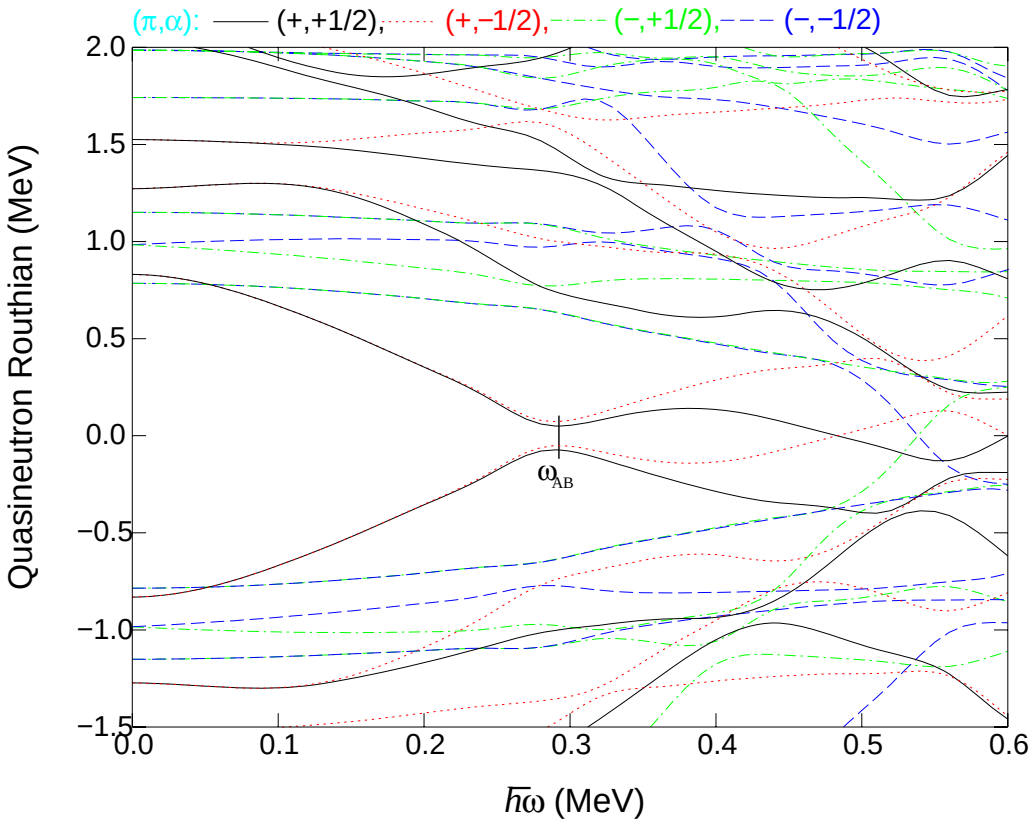


Figure 5.21: CSM calculations for the af configuration, using the deformation parameters $\beta_2 = 0.298$, $\beta_4 = -0.018$, $\gamma = 1.3°$.

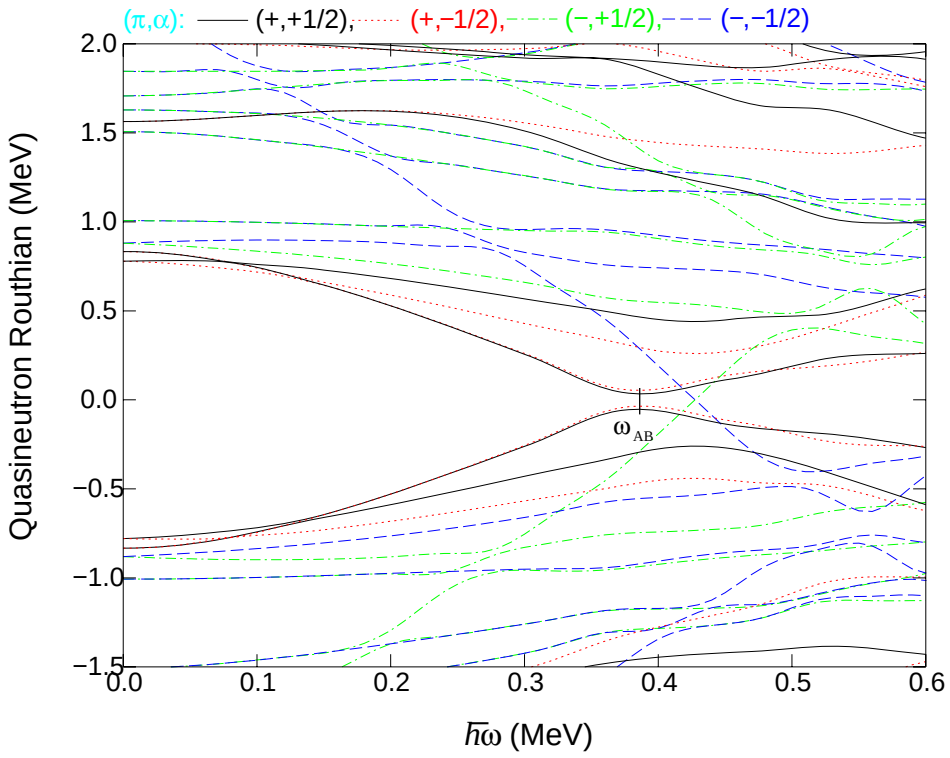


Figure 5.22: CSM calculation using adjusted deformation parameters $\beta_2 = 0.35$, $\beta_4 = 0.03$, $\gamma = 0°$.

the AB crossing is seen to shift towards higher frequency, becoming closer to the observed value of 0.43 MeV. The β_2 parameter yields a quadrupole moment of $Q_t = 10.6$ eb, which is higher than the value for the ground-state band (∼7 eb). However, it is smaller than the measured quadrupole moments of the SD family of bands (∼13.5 eb). Such an observation suggests that Band 6 might be built on a shape with intermediate deformation. Support for this comes from observation of spectra of Band 6. Fig. 5.23 shows a spectrum of the $\alpha = 0$ partner of Band 6, with transitions between 555 keV and 809 keV. One can see the characteristic Doppler broadening in the transitions above 555 keV at forward and backward angles and at 90°. It is important to note that this change is different compared with the Doppler shift pattern for the SD bands (recall Fig. 4.8). In the case of Band 6, the peaks have both a stopped and moving component. Such a line shape pattern is common for transitions that emerge from rotational bands with intermediate deformation (see for example [Gor04], ^{163}Lu). By analogy, such an observation in ^{174}Hf supports the suggestion for an intermediate deformation of Band 6, perhaps large enough to explain the delay of the AB crossing frequency.

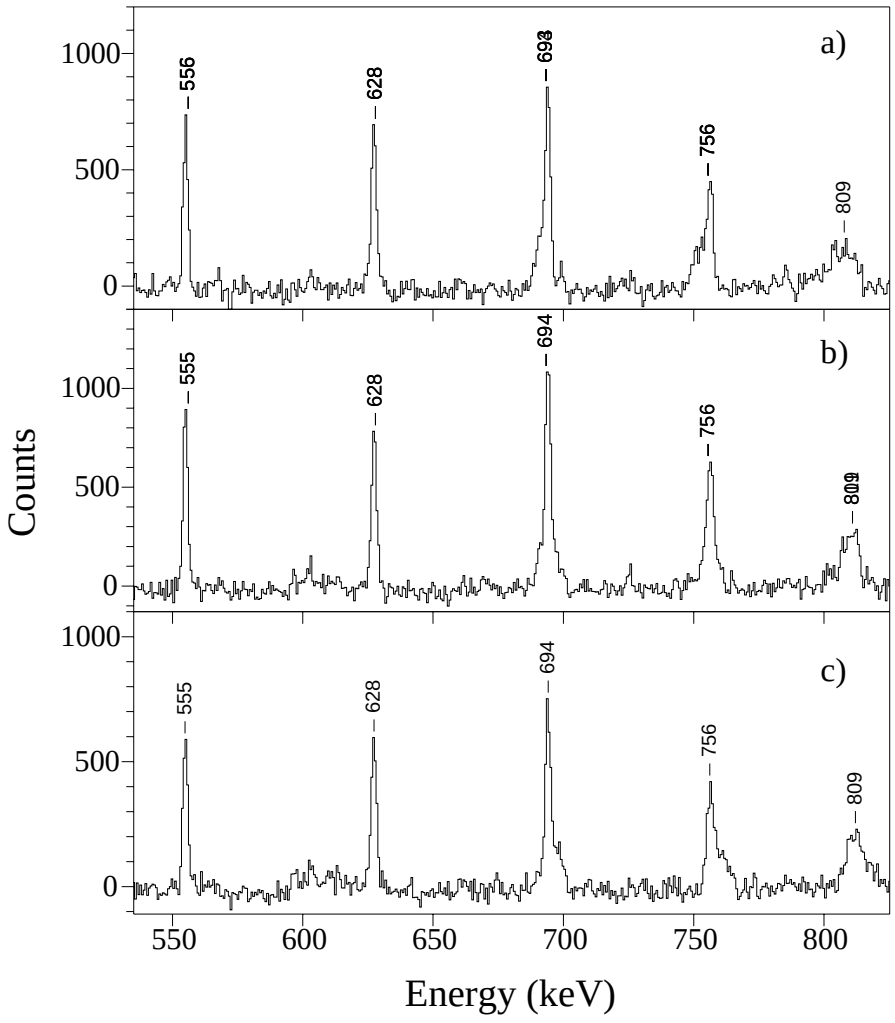


Figure 5.23: Partial summed spectra of the $\alpha = 0$ signature partner in Band 6, obtained from the BLUE database by gating on all transitions between 555 keV and 809 keV. Panel a) denotes summed spectrum at backward angles 121.7° and 129.9°. Panel b) presents summed spectra at 79.9°, 90°, and 100.0°. Panel c) shows summed spectra at forward angles 50.1° and 58.3°. The lineshape change due to the Doppler broadening is clearly visible above the 628-keV transition.

Chapter 6

Conclusions

This dissertation concentrated on the study of the well-deformed nucleus ^{174}Hf. Various high angular momentum modes were studied from the γ-ray data obtained from the GAMMASPHERE spectrometer. Surprisingly, superdeformed bands were found in the first experiment, which then led to two further experiments for the investigation of these structures. The rich data were also used to study rotational bands based on normal deformation and extend some of the sequences near 50 $\hbar$.

Beams produced from the Argonne National Laboratory Atlas accelerator as well as the 88" Cyclotron at Lawrence Berkeley National Laboratory, utilized the fusion-evaporation reaction ^{130}Te(^{48}Ca,4n) to study the high-spin states in ^{174}Hf. In each experiment, 700 million to 3.5 billion γ-ray coincidence events were collected. The GSFMA90 thin-target experiment revealed the first four candidate superdeformed rotational bands. The GS2K047 experiment used a self-supporting, gold-backed target to measure the average lifetime of the superdeformed states via the Doppler Shift Attenuation method (DSAM). This enabled us to determine the deformation of these bands. Finally, the focus for the GSFMA117 experiment was to search for linking transitions between the superdeformed bands as such transitions may suggest the presence of triaxial deformation.

Although the first experiment was not optimized to find superdeformed sequences, four weak bands were observed with large moments of inertia in ^{174}Hf. Unfortunately, these structures could not be directly connected with known states in ^{174}Hf, but they show clear coincidence with the ground-state sequence in this even-even nucleus. Subsequent calculations using the Ultimate Cranker model strongly suggested that superdeformed structures in ^{174}Hf will have significant triaxial deformation ($\sim$20°). Thus, it appeared that the recently observed region of triaxial superdeformation (TSD) near $N = 94$ nuclei may be larger than once thought and extend into $N > 100$ nuclei. However, further investigation of these

bands was required to prove that they are indeed TSD structures. First, an experiment that would determine the deformation of these bands was necessary to prove that they are actually superdeformed. In order to confirm the large deformation, the DSAM experiment was performed at LBNL. The large data set was sorted into a BLUE database [Cro01] such that relatively quick angle-dependent, double gates could be extracted with ease. In addition, a semi-automatic background subtraction method [Sta03] was utilized to produce the best possible spectra. Since the lifetimes of superdeformed states are so short, all of the transitions in the bands were found to be Doppler shifted. Thus, moving gates were required to observe the bands such that the fractional Doppler shifts of the transitions could be measured. These shifts were then modeled by the code FITFTAU [Moo97] to extract the quadrupole moments. These measurements confirmed the large deformation of the new bands as Q_t values ranging from 12.6 to 13.5 eb were determined. Since normal deformation has been predicted to have a quadrupole moment of 7 eb [Wal83], these values clearly indicate the four new bands are superdeformed. Therefore, the SD part of TSD was verified, but a dedicated thin-target experiment was necessary to search for linking transitions between the superdeformed bands.

In light Lu ($N \approx 92$) nuclei, sequences are found exclusively linking into the $\pi i_{13/2}$ bands [Ode01]. These excitations have characteristics that are remarkably similar to the $i_{13/2}$ band. That is, the dynamic moment of inertia and alignment values are nearly identical to the $i_{13/2}$ band over the observed frequency range. Ødegård *et al.* [Ode01] provided convincing arguments that these sequences cannot be the signature partner of the $i_{13/2}$ band, but instead were likely wobbling excitations based on this quasiproton state. A wobbling sequence can only occur when a nucleus with a triaxial deformation is rotating. Thus, identification of wobbling is proof of triaxiality, and is perhaps the best evidence of the asymmetric shape. Since the wobbling excitation can be regarded as a wobbling phonon coupled to the $i_{13/2}$ band, one would indeed expect identical characteristics with this band. But more importantly, Ødegård *et al.* determined that the $\Delta I = 1$ transitions between the wobbling sequence and the $i_{13/2}$ band were dominated by an $E2$ component, which is quite unusual. However, particle-rotor calculations [Ode01, Ham02, Ham03] showed that this feature is expected from the decay of the wobbling excitation. Therefore, with four SD bands known in ^{174}Hf, it seemed very possible that at least one of them could be a wobbling sequence and that a search for linking transitions clearly needed to be performed. In this light, we were granted a week of beam time with GAMMASPHERE to obtain enough statistics that these linking transitions may be observed. The increased data allowed for the identification of four more possible SD bands (thus bringing the total of SD bands in ^{174}Hf to eight) and one SD band in ^{173}Hf. However, no linking transitions were found that were

consistent with wobbling. In addition, even the strongest SD bands could not be linked with the normal deformed states. These results do not necessarily rule out the possibility of wobbling being observed. In fact, as shown previously, there appears to be two groups or families of bands with similar moments of inertia. The fact that the four strongest bands also have similar quadrupole moments is also consistent with the possibility of wobbling. However, these two observations are not unique to wobbling, thus, it is not possible to confirm triaxiality in ^{174}Hf at this time.

Not only do we have no evidence for triaxiality in ^{174}Hf, but there is also evidence which is contradictory to this interpretation. First, the measured quadrupole moments of 12.6 to 13.8 eb are much larger than the predictions of $\sim$10 eb by the Ultimate Cranker. Positive γ deformation reduces the quadrupole moment value, which is why a relatively small value (for superdeformation) is produced by the Ultimate Cranker. The fact that the measured values are so large may suggest that these bands have γ closer to 0°. Note also that the measured values are much larger than those for the TSD bands in Lu [Gor04]. Secondly, the neighboring odd-A Hf nuclei appear to only have one SD band in each. If the region of TSD structures does extend into $N \approx 100$ nuclei, then one would expect candidate wobbling bands also in the ^{173,175}Hf nuclei as well. This is not a matter of intensity for ^{173}Hf as its SD band was observed with approximately the same population strength at the strongest SD band in ^{174}Hf. If one assumes that the wobbling excitation energy is similar in both nuclei, and that wobbling exists in ^{174}Hf, then at least one other SD band in ^{173}Hf would be observed.

Another important point that was addressed is that these bands in Hf nuclei appear to be a different class of SD band than those seen in the Lu nuclei. Recently, the SD band in ^{175}Hf was linked to the known states, and thus the spin and parity of the band could be determined [Cul04]. It was determined that the SD band is based on a seven-quasiparticle configuration which included two $i_{13/2}$ protons and two $j_{15/2}$ neutrons [Cul04]. Since this band is isospectral with the strongest SD band in ^{174}Hf, it is likely that the SD bands in ^{174}Hf have a similar configuration. The larger quadrupole moment for the Hf bands with respect to the Lu bands seems to confirm this interpretation, as the $j_{15/2}$ neutrons likely contribute to a larger deformation. Since the Hf bands are likely based on at least six quasiparticles, there is clearly a large structural difference as compared with the Lu bands.

It may be tempting to state that these bands are simply superdeformed and that there is no triaxiality involved in their shapes. However, if a superdeformed minimum exists in ^{174}Hf that is robust enough to support eight different configurations, why are there only single SD bands in ^{173,175}Hf? Naively, one would expect multiple SD bands in these nuclei as well. Clearly, there is still much to be learned in order to resolve this puzzle. More

examples of wobbling bands must be discovered to understand the critical factors which supports these exotic features. In addition, perhaps exploring for SD structures in nearby tungsten nuclei would aid in our understanding of superdeformation in even-Z nuclei of the mass 170 region.

The rich data taken to study the superdeformed bands provided new information on the normal deformed structures. Eight rotational bands built on two-quasiparticle excitations are observed and a total of 205 levels and 284 transitions were placed. No high-K isomers were studied here due to the specific experimental setup with thin and self-supporting targets. Experiments that used a pulsed beam to study high-K structures were performed in a separate project.

The ground-state band and the β-vibrational band were extended to spin of $42\,\hbar$ and $40\,\hbar$, respectively. In both bands, the neutron $i_{13/2}$ AB crossing and the proton $h_{9/2}$ ef crossing were identified at 0.3 MeV and around 0.5 MeV.

Band 3 is extended to spin of $49\,\hbar$. Specific properties of this band were observed. Enhanced $E1$ transitions were observed to decay out to the ground-state band, with $B(E1; I \rightarrow I-1)/B(E2; I \rightarrow I-2)$ ($8^- \rightarrow 6^-$, 8^+) being $\sim$50 times larger than that in Band 6, but close to the ratio deduced for the octupole band in ^{172}Yb. The observations favor an octupole vibrational nature of Band 3. This mode is strong at low spin due to the presence of neutron $i_{13/2}$ and $f_{7/2}$ and proton $h_{11/2}$ and $d_{5/2}$ orbitals near the Fermi surface. The large signature splitting (150 keV) in this band is explained by the mixture between orbitals with $K^\pi = 1^-$ (odd and even spins) and $K^\pi = 0^-$ (odd spins only). A coupling to a configuration that exhibits a large signature splitting is well understood theoretically, and it seems plausible to assume this to be the cause for the observed splitting in Band 3.

The expected neutron $i_{13/2}$ AB crossing is absent in Band 3, and the second neutron $i_{13/2}$ BC crossing is observed. This identifies the largest component in the configuration of this band to be $\nu i_{13/2} \otimes \nu f_{7/2}$ (AE, AF). The observed proton ef crossing is allowed by this configuration and by the additional component - two proton $h_{11/2} \otimes d_{5/2}$ [Nee70]. The seemingly contradictory property of Band 3, namely, the absence of the AB crossing in the octupole-vibrational band is understood in terms of interplay of collective and single-particle degrees of freedom. By comparison, the AB crossing is observed in the β-vibrational band in ^{174}Hf.

Bands 4, 5, and 7 are identified as built on two-neutron configurations. Bands 5 and 7 involve the $\nu i_{13/2}$ orbital and thus the BC crossing is observed. However, this crossing occurs at a significantly lower rotational frequency than expected. It is suggested that this effect is due to decreased pairing correlations by the blocking of neutron orbitals near the Fermi level. This effect has been discussed by Garrett *et al.* [Gar81] and an average decrease

of 17% has been suggested for rare-earth nuclei. In the case of ^{174}Hf, the decrease found in Band 5 and 7 are similar, 20% and 18%, respectively.

Band 6 has a proposed two-proton configuration $h_{9/2} \otimes g_{7/2}$ (fa, fb). The first observed crossing is expected to be AB, however, it is found to be delayed to a frequency of 0.43 MeV (43%). Such a large delay of crossings in rotational bands that involve the $\pi h_{9/2}$ orbital has been observed in a broad region of odd-proton nuclei. It is commonly attributed to two mechanisms: a) residual interaction between this proton orbital and the $i_{13/2}$ neutrons that are involved in the crossing, and b) an increase of deformation by the shape-driving $h_{9/2}$ proton orbital.

Attention was given to both possibilities to determine to what extent they affect the delay of the AB crossing in Band 6. For the case a), the sizes of the interaction matrix elements between proton and neutron orbitals were derived by comparing the Routhians of odd-even orbitals and the expected Routhian obtained by the sum of constituent proton and neutron orbitals. This method works best in odd-odd nuclei, but its direct application to the even-even nucleus ^{174}Hf did not produce fruitful results, as the obtained value for the amount of delay in the crossing frequency had a negative value. A possible cause for this discrepancy is the lack of knowledge about the exact value of the pairing strength at non-zero rotational frequency.

An investigation of the influence of deformation on the delay of the AB crossing in Band 6 have been performed as well. Total Routhian Surface calculations for the af and bf configurations in ^{174}Hf were performed and the deformation parameters β_2, β_4, and γ at a rotational frequency close to the crossing frequency were used in CSM calculations. It is shown that the TRS does not produce the amount of deformation to account for the delay, as the deformation parameters affect negligibly the shift of the crossing frequency. However, it was of interest to verify what values for the deformation parameters would reproduce the observed AB crossing at 0.43 MeV. The deduced values yield a higher deformation than the one for the ground-state band ($Q_t \sim 7\,$eb). The corresponding quadrupole moment for this band inferred in this manner has a value of $Q_t \sim 10\,$eb, which is lower compared to the deformation of the superdeformed bands ($Q_t \sim$12.5 eb). An intermediate deformation for Band 6 was also suggested by the observed γ-ray spectra for this band. Due to an enhanced Doppler shift for transitions in this band, a lineshape change for these transitions in the band indicated higher deformation. Similar lineshapes are observed in DSAM experiments on Lu isotopes.

The results shown here demonstrate the very nice result that can be obtained in nuclear physics at higher angular momentum with the current forefront spectrometer - GAMMASPHERE. Exploring features at high angular momentum or farther from the yrast line will require a

substantial increase in resolving power for a γ-ray spectrometer. The field is moving in that direction with the early development of γ-ray tracking counters. The U.S. project GRETA and the European AGATA are developing detectors that can track the Compton scattered γ rays in a Ge crystal and recover the total energy deposited. An array of such tracking detectors should result in resolving power several orders of magnitude beyond GAMMASPHERE.

With this enhanced resolving power, one could in the future pursue some of the puzzles remaining after this dissertation. For example, it is important to measure precisely the lifetimes in Band 6 in ^{174}Hf to pin down the size of the intermediate deformation suggested by the work here (this measurement can possibly be performed with the current generation of spectrometers). This will help resolve the question of the deformation increase caused by the $\pi h_{9/2}$ orbital in the rare-earth region.

Finding the predicted triaxial shape and wobbling mode in the Hf region will certainly require the next generation of spectrometers. This mode is predicted for ^{174}Hf but unseen in the measurements described here. To settle this issue, future researchers will need to look for the superdeformed bands associated with the wobbling mode at higher excitation energies (and at much weaker population intensities). Also, future experiments need to search for families of superdeformed bands in ^{173,175}Hf similar to the set of eight seen in ^{174}Hf. Only one SD band was observed in the odd-A Hf nuclei, which is difficult to understand from the standpoint of a) available quasiparticle configurations or b) strongly deformed triaxial minima. Clearly, there are challenges for the future, both in experiment and in theory. In experiment, the challenge is to build and utilize the next generation spectrometers for observing the wobbling modes now too weak to study. In theory, the task is to understand why triaxial superdeformed bands are not observed in ^{174}Hf, contrary to predictions within the framework of the Ultimate Cranker.

Bibliography

Bibliography

[Ale78] T. K. Alexander and J. S. Forster, *Advances in Nuclear Physics*, Plenum, New York, 1978, vol. 10, p.197.

[Amr01] H. Amro, P. G. Varmette, W. C. Ma, B. Herskind, G. B. Hagemann, G. Sletten, R. V. F. Janssens, M. Bergström, A. Bracco, M. Carpenter, J. Domscheit, S. Frattini, D. J. Hartley, H. Hübel, T. L. Khoo, F. Kondev, T. Lauritsen, C. J. Lister, B. Million, S. W. Ødegård, R. B. Piercey, L. L. Riedinger, K. A. Schmidt, S. Siem, I. Wiedenhöver, J. N. Wilson, and J. A. Winger, Phys. Lett. **506B**, 39 (2001).

[Amr03] H. Amro, W. C. Ma, G. B. Hagemann, R. M. Diamond, J. Domscheit, P. Fallon, A. Görgen, B. Herskind, H. Hübel, D. R. Jensen, Y. Li, A. O. Macchiavelli, D. Roux, G. Sletten, J. Thompson, D. Ward, I. Wiedenhöver, J. N. Wilson, and J. A. Winger, Phys. Lett. **553B**, 197 (2003).

[Bak95] C. Baktash, B. Haas, and W. Nazarewicz, Ann. Rev. Nucl. Part. Sci. 45 (1995) 485

[Bar98] R. A. Bark, H. Carlsson, S. J. Freeman, G. B. Hagemann, E. Ingebretsen, H. J. Jensen, T. Lönnroth, S. Mitarai, M. J. Piiparinen, H. Ryde, H. Schnack-Petersen, and P. O. Tjøm, Nucl. Phys. **A644**, 29 (1998).

[Bar98a] R. A. Bark, H. Carlsson, S. J. Freeman, G. B. Hagemann, F. Ingebretsen, H. J. Jensen, T. Lönnroth, M. J. Piiparinen, I. Ragnarsson, H. Ryde, H. Schnack-Petersen, R. B. Semmes, P. O. Tjøm, Nucl. Phys. **A630**, 603 (1998).

[Bea95] C. W. Beausang, D. Prevost, M. H. Bergstrom, G. deFrance, B. Haas, J. C. Lisle, Ch. Theisen, J. Timár, P. J. Twin, and J. N. Wilson, Nucl. Inst. Meth. Phys. Res. A **364**, 560 (1995).

[Ben75] R. Bengtsson, S. E. Larsson, G. Leander, P. Möller, S. G. Nilsson, S. Åberg, and Z. Szymanski, Phys. Lett. **57B**, 301 (1975).

[Ben79] T. Bengtsson and S. Frauendorf, Nucl. Phys. **A314**, 27 (1979).

[Ben79a] T. Bengtsson and S. Frauendorf, Nucl. Phys. **A327**, 139 (1979).

[Ben88] T. Bengtsson, I. Ragnarsson, and S. Åberg, Phys. Lett. **208B**, 39 (1988).

[Ben89] T. Bengtsson, Nucl. Phys. **A496**, 56 (1989).

[Ben90] T. Bengtsson, Nucl. Phys. **A512**, 124 (1990).

[Ben04] R. Bengtsson and H. Ryde, Eur. Phys. J. **A22**, 355 (2004).

[Bet36] H. A. Bethe, and R. F. Bacher, Rev. Mod. Phys. **8**, 82 (1936), C. F. Weizsäker, Z. Phys. **96**, 431 (1935).

[Bla66] A. E. Blaugrund, Nucl. Phys. **88**, 501 (1966).

[Boh58] A. Bohr, B. R. Mottelson, and D. Pines, Phys.Rev. **110**, 936, (1958).

[BoM98] A. Bohr and B. R. Mottelson, *Nuclear Structure*, Second edition, World Scientific Publishing Co. Pte. Ltd., River Edge, NJ, 1998.

[Bri05] P. Bringel, in preparation.

[Car75] M. H. Cardoso, L. Klieb, P. F. Goudsmit, and J. Konijn, Z. Physik A **272**, 13 (1975).

[Cro01] M. Cromaz, T. J. M. Symons, G. J. Lane, I. Y. Lee, and R. W. MacLeod, Nucl. Inst. Meth. Phys. Res. A **462**, 519 (2001).

[Crw95] B. Crowell, M. P. Carpenter, R. G. Henry, R. V. F. Janssens, T. L. Khoo, T. Lauritsen, and D. Nisius, Nucl. Inst. Meth. Phys. Res. A **355**, 575 (1995).

[Cul98] D. M. Cullen, A. T. Reed, D. E. Appelbe, A. N. Wilson, E. S. Paul, R. M. Clark, P. Fallon, I. Y. Lee, and A. O. Macchiavelli, R. W. MacLeod, Nucl. Phys. **A638**, 662 (1998).

[Cul00] D. M. Cullen, A. T. Reed, D. E. Appelbe, A. N. Wilson, E. S. Paul, M. H. Bergström, J. F. Sharpey-Schafer, C. Baktash, I. Frosch, I. Y. Lee, A. O. Macchiavelli, R. W. MacLeod, D. Prevost, Ch. Theisen, and D. Curiend, Nucl. Phys. **A673**, 3 (2000).

[Cul04] D. T. Scholes, D. M. Cullen, F. G. Kondev, R. V. F. Janssens, M. P. Carpenter, D. J. Hartley, M. K. Djongolov, G. Sletten, G. Hagemann, C. Wheldon, P. M. Walker, K. Abu Saleem, I. Ahmad, D. L. Balabanski, P. Chowdhury, M. Danchev, G. D. Dracoulis,

H. M. El-Masri, J. Goon, A. Heinz, R. A. Kaye, T. L. Khoo, T. Lauritsen, C. J. Lister, E. F. Moore, L. L. Riedinger, M. A. Riley, D. Seweryniak, I. Shestakova, I. Wiedenhöver, O. Zeidan, and Jing-ye Zhang, Phys. Rev. C **70**, 054314 (2004).

[Del99] M. A. Deleplanque, I. Y. Lee, K. Vetter, G. J. Schmid1, F. S. Stephens, R. M. Clark, R. M. Diamond, P. Fallon, and A. O. Macchiavelli, Nucl. Inst. Meth. Phys. Res. A **430**, 292 (1999).

[Djo03] M. K. Djongolov, D. J. Hartley, L. L. Riedinger, F. G. Kondev, R. V. F. Janssens, K. Abu Saleem, I. Ahmadc, D. L. Balabanski, M. P. Carpenter, P. Chowdhury, D. M. Cullen, M. Danchev, G. D. Dracoulis, H. El-Masri, J. Goon, A. Heinz, R. A. Kaye, T. L. Khoo, T. Lauritsen, C. J. Lister, E. F. Moore, M. A. Riley, D. Seweryniak, I. Shestakova, G. Sletten, P. M. Walker, C. Wheldon, I. Wiedenhöver, O. Zeidan, and Jing-Ye Zhang, Phys. Lett. **560B**, 24 (2003).

[Don87] F. Dönau, Nucl. Phys. **A471**, 469 (1987).

[Dra80] G. D. Dracoulis, and P. M. Walker, Nucl. Phys. **A342**, 335 (1980).

[Eji71] H. Ejiri and G. B. Hagemann, Nucl. Phys. **A161**, 449 (1971).

[Fab91] B. Fabricius, G. D. Dracoulis, T. Kibedi, A. E. Stuchbery, and A. M. Baxter, Nucl. Phys. **A523**, 426 (1991).

[Fir96] R. B. Firestone (Ed.), *Table of Isotopes* 8th ed. **2**, (1996).

[Fir97] R. B. Firestone and B. Singh, *Table of Superdeformed Nuclear Bands and Fission Isomers.*, (1997).

[Fra81] S. Frauendorf, Phys. Lett. **100B**, 219 (1981).

[Fra81a] S. Frauendorf, Phys. Scr. **24**, 349 (1981).

[Fra84] S. Frauendorf, L. L. Riedinger, J. D. Garrett, J. J. Gaardhøje, G. B. Hagemann, and B. Herskind, Nucl. Phys. **A431**, 511 (1984).

[Gal58] C. J. Gallagher and S. A. Moszkowski, Phys. Rev. **111**, 1282 (1958).

[Gar81] J. D. Garrett, O. Andersen, J. J. Gaardhøje, G. B. Hagemann, B. Herskind, J. Kownacki, J. C. Lisle, L. L. Riedinger, W. Walús, N. Roy, S. Jönsson, H. Ryde, M. Guttormsen, and P. O. Tjøm, Phys. Rev. Lett. **47**, 75 (1981).

[Gas90] J. Gascon, C.-H. Yu, G. B. Hagemann, M. C. Carpenter, J. M. Espino , Y. Iwata, T. Komatsubara, J. Nyberg, S. Ogaza, G. Sletten, P. O. Tjøm, D. C. Radford, J. Simpson, A. Alderson, M. A. Bentley, P. Fallon, P. D. Forsyth, J. W. Roberts, and J. F. Sharpey-Schafer, Nucl. Phys. **A513**, 344 (1990).

[Gor04] A. Görgen, R. M. Clark, M. Cromaz, P. Fallon, G. B. Hagemann, H. Hübel, I. Y. Lee, A. O. Macchiavelli, G. Sletten, D. Ward, and R. Bengtsson, Phys. Rev. C **69**, 031301 (2004).

[Grp94] N. L. Gjørup, *An experimental investigation of the competition between different alignment schemes in the hafnium isotopes* ^{174}*Hf and* ^{175}*Hf with special emphasis on angular momentum selection rules*, Dissertation, Københavns Universitet, Denmark, 1994

[Ham02] I. Hamamoto, Phys. Rev. C **65**, 044305 (2002).

[Ham03] I. Hamamoto and G. Hagemann, Phys. Rev. C **67**, 014319 (2003).

[Har05] D. J. Hartley, M. K. Djongolov, L. L. Riedinger, G. B. Hagemann, R. V. F. Janssens, F. G. Kondev, E. F. Moore, M. A. Riley, A. Aguilar, C. R. Bingham, D. B. Campbell, M. P. Carpenter, P. Chowdhury, M. Cromazh, D. M. Cullen, M. Danchev, G. D. Dracoulis, P. Fallon, J. Goon, R. A. Kaye, T. L. Khoo, R. W. Laird, T. Lauritsen, A. O. Macchiavelli, B. McClain, G. Mukherjee, E. Ngijoi-Yogo, H. I. Park, G. Sletten, S. K. Tandel, P. M. Walker, and Jing-Ye Zhang, Phys. Lett. **608B**, 31, (2005).

[Har05a] D. J. Hartley, private communication.

[Har05b] D. J. Hartley, W. H. Mohr, J. R. Vanhoy, M. A. Riley, A. Aguilar, C. Teal, R. V. F. Janssens, M. P. Carpenter, A. A. Hecht, T. Lauritsen, E. F. Moore, S. Zhu, F. G. Kondev, M. K. Djongolov, M. Danchev, L. L. Riedinger, G. B. Hagemann, G. Sletten, P. Chowdhury, S. K. Tandel, W. C. Ma, S. W. Ødegård, Phys. Rev. C **72**, 064325 (2005)

[Har65] S. M. Harris, Phys. Rev. **138**, 509B (1965).

[Hax49] O. Haxel, J. H. D. Jensen, and H. E. Seuss, Phys. Rev. **75**, 1766 (1949).

[Hil53] D. L. Hill and J. A. Wheeler, Phys. Rev. **89**, 1102 (1953).

[HYu90] C.-H. Yu, G. B. Hagemann, J. M. Espino, K. Furuno, J. D. Garrett, R. Chapman, D. Clarke, F. Khazaie, J. C. Lisle, J. N. Mo, M. Bergström, L. Carlen, P. Ekström, J. Lyttkens, and H. Ryde, Nucl. Phys. **A511**, 157 (1990).

[Ing54] D. R. Inglis, Phys. Rev. **69**, 1059, 1954.

[Jen00] D. R. Jensen, J. Domscheit, G. B. Hagemann, M. Bergström, B. Herskind, B. S. Nielsen, G. Sletten, P. G. Varmette, S. Törmänen, H. Hübel, W. Ma, A. Bracco, F. Camera, F. Demaria, S. Frattini, B. Million, D. Napoli, A. Maj, B. M. Nyakó, D. T. Joss, and M. Aiche, Eur. Phys. J. **A8**, 165 (2000).

[Jen01] H. J. Jensen, R. A. Bark, P. O. Tjøm, G. B. Hagemann, I. G. Bearden, H. Carlsson, S. Leoni, T. Lönnroth, W. Reviol, L. L. Riedinger, H. Schnack-Petersen, T. Shizuma, X. Z. Wang, and J. Wrzesinski, Nucl. Phys. **A695**, 3 (2001).

[Jen02] D. R. Jensen, G. B. Hagemann, I. Hamamoto, S.W. Ødegård, B. Herskind, G. Sletten, J. N.Wilson, K. Spohr, H. Hübel, P. Bringel, A. Neußer, G. Schönwaßer, A. K. Singh, W. C. Ma, H. Amro, A. Bracco, S. Leoni, G. Benzoni, A. Maj, C. M. Petrache, G. Lo Bianco, P. Bednarczyk, and D. Curien, Phys. Rev. Lett. **89**, 142503 (2002).

[Jen02a] D. R. Jensen, G. B. Hagemann, I. Hamamoto, S. W. Ødegård, M. Bergström, B. Herskind, G. Sletten, S. Törmänen, J. N. Wilson, P. O. Tjøm, K. Spohr, H. Hübel, A. Görgen, G. Schönwaßer, A. Bracco, S. Leoni, A. Maj, C. M. Petrache, P. Bednarczyk, and D. Curien, Nucl. Phys. **A703**, 3 (2002).

[Kon99] F. G. Kondev, M. A. Riley, D. J. Hartley, T. B. Brown, R. W. Laird, M. Lively, J. Pfohl, R. K. Sheline, E. S. Paul, D. T. Joss, P. J. Nolan, S. L. Shepherd, R. M. Clark P. Fallon, D. G. Sarantites, M. Devlin, D. R. LaFosse, F. Lerma, R. Wadsworth, I. M. Hibbert, N. J. O'Brien, J. Simpson, and D. E Archer, Phys. Rev. C **60**, 011303 (1999).

[Lai00] R. W. Laird, *Global lifetime measurements of highly-deformed and other rotational structures in the A$\sim$ 135 light rare-earth region*, Dissertation, Florida State University, 2000.

[Lee90] I-Yang Lee, Nucl. Phys. **A520**, 641 (1990).

[Lie01] R. M. Lieder, Nucl. Phys. **A682**, 279c (2001).

[Lin63] J. Lindhard, M. Shariff, and H. E. Schiott, Mat. Fys. Medd. Dan. Vid. Selsk. **33**, No. 14 (1963).

[Lis81] J. C. Lisle, J. D. Garrett, G. B. Hagemann, B. Herskind, and S. Ogaza, Nucl. Phys. **A366**, 281 (1981).

[May49] M. G. Mayer, Phys. Rev. **75**, 1969 (1949).

[Moa71] C. Moazed, T. Becker, P. A. Assimakopolous, and D. M. Van Patter, Nucl. Phys. **A169**, 651 (1971).

[Mol95] P. Möller, J. R. Nix, W. D. Myers, and W. J. Swiatecki, At. Data Nucl. Data Tables **59**, (1995) 185.

[Moo97] E. F. Moore, T. Lauritsen, R. V. F. Janssens, T. L. Khoo, D. Ackermann, I. Ahmad, H. Amro, D. Blumenthal, M. P. Carpenter, S. M. Fischer, G. Hackman, D. Nisius, F. Hannachi, A. Lopez-Martens, A. Korichi, S. Asztalos, R. M. Clark, M. A. Deleplanque, R. M. Diamond, P. Fallon, I. Y. Lee, A. O. Macchiavelli, F. S. Stephens, J. A. Becker, L. Bernstein, L. P. Farris, and E. A. Henry, Phys. Rev. C **55**, R2150 (1997).

[Naz85] W. Nazarewicz, J. Dudek, R. Bengtsson, T. Bengtsson, and I. Ragnarsson, Nucl. Phys. **A435**, 397 (1985).

[Nee70] K. Neergård and P. Vogel, Nucl. Phys. **A145**, 33 (1970).

[Nee75] K. Neergård and V. V. Pashkevich, Phys. Lett **59B**, 218, (1975).

[Nee76] K. Neergård, V. V. Pashkevich, and S. Frauendorf, Nucl. Phys. **A262**, 61 (1976).

[Neu02] A. Neußer, H. Hübel, G. B. Hagemann, S. Bhattacharya, P. Bringel, D. Curien, O. Dorvaux, J. Domscheit, F. Hannachi, D. R. Jensen, A. Lopez-Martens, E. Mergel, N. Nenoff, and A. K. Singh, Eur. Phys. J. **A15**, 439 (2002).

[Nil69] S. G. Nilsson, C. F. Tsang, A. Sobiczewski, Z. Szymański, S. Wycech, C. Gustafson, I. Lamm, P. Möller, and B. Nilsson, Nucl. Phys. **A131**, 1 (1969).

[Nil95] S. G. Nilsson, I. Ragnarsson, *Shapes and Shells in Nuclear Structure*, First edition, Cambridge University Press, 1995.

[Ode01] S. W. Ødegård, G. B. Hagemann, D. R. Jensen, M. Bergström, B. Herskind, G. Sletten, S. Törmänen, J. N. Wilson, P. O. Tjøm, I. Hamamoto, K. Spohr, H. Hübel, A. Görgen, G. Schönwaßer, A. Bracco, S. Leoni, A. Maj, C. M. Petrache, P. Bednarczyk, and D. Curien, Phys. Rev. Lett. **86**, 5866 (2001).

[Oga93] S. Ogaza, J. Kownacki, M. P. Carpenter, J. Gascon, G. B. Hagemann, Y. Iwata, H. J. Jensen, T. Komatsubara, J. Nyberg, G. Sletten, P. O. Tjøm, and W. Waluś, Nucl. Phys. **A559**, 100 (1993).

[Pal85] G. Palameta and J. C. Waddington, Nucl. Inst. Meth. Phys. Res. A **234**, 476 (1985).

[Rad95] D. C. Radford, Nucl. Inst. Meth. Phys. Res. A **361**, 297 (1995).

[Rad95a] D. C. Radford, Nucl. Inst. Meth. Phys. Res. A **361**, 306 (1995).

[Rev99] W. Reviol, L. L. Riedinger, X. Z. Wang, J.-Y. Zhang, H. J. Jensen, G. B. Hagemann, R. A. Bark, P. O. Tjøm, S. Leoni, T. Lönnroth, H. Schnack-Petersen, T. Shizuma, J. Wrzesinski, and P. B. Semmes, Phys. Rev. C **59**, 1351 (1999).

[Rin00] P. Ring and P. Shuck, *The Nuclear Many Body Problem*, Second edition, Springer-Verlag, Berlin New York, 2000.

[Sat93] W. Satuła, R. Wyss, and F. Dönau, Phys. **A565**, 573 (1993).

[Sch02a] G. Schönwaßer, H. Hübel, G. B. Hagemann, H. Amro, R. M. Clark, M. Cromaz, R. M. Diamond, P. Fallon, B. Herskind, G. Lane, W. C. Ma, A. O. Macchiavelli, S. W. Ødegård, G. Sletten, D. Ward, and J. N. Wilson, Eur. Phys. J. **A15**, 435 (2002).

[Sch03] G. Schönwaßer, H. Hübel, G. B. Hagemann, P. Bednarczyk, G. Benzoni, A. Bracco, P. Bringel, R. Chapman, D. Curienc, J. Domscheit, B. Herskind, D. R. Jensen, S. Leoni, G. Lo Biancog, W. C. Ma, A. Maj, A. Neußer, S. W. Ødegård, C. M. Petrache, D. Roßbach, H. Ryde, K. H. Spohr, and A. K. Singh, Phys. Lett. **552B**, 9 (2003).

[ScP95] H. Schnack-Petersen, R. Bengtsson, R. A. Bark, P. Bosetti, A. Brockstedt, H. Carlsson, L. P. Ekström, G. B. Hagemann, B. Herskind, F. Ingebretsen, H. J. Jensen, S. Leoni, A. Nordlund, H. Ryde, P. O. Tjøm, and C. X. Yang, Nucl. Phys. **A594**, 175 (1995).

[Sta03] K. Starosta, D. B. Fossan, T. Koike, C. Vaman, D. C. Radford, and C. J. Chiara, Nucl. Inst. Meth. Phys. Res. A **515**, 771 (2003).

[Str67] V. M. Strutinski, Nucl. Phys. **A95**, 420 (1967).

[Str68] V. M. Strutinski, Nucl. Phys. **A122**, 1 (1968).

[Sun94] Yang Sun, Shuxian Wen, and Da Hsuan Feng, Phys. Rev. Lett. **72**, 3483 (1994).

[Twi86] P. J. Twin, B. M. Myakó, A. H. Nelson, J. Simpson, M. A. Bentley, H. W. Cramner-Gordon, P. D. Forsyth, D. Howe, A. R. Mokhtar, J. D. Morrison, J. F. Sharpey-Schafer, and G. Sletten, Phys. Rev. Lett. **57**, 811 (1986).

[Ven03] Ts. Venkova, R. M. Lieder, W. Gast, D. Bazzacco, G. de Angelis, E. Podsvirova, H. M. Jäger, L. Mihailescu, R. Menegazzo, S. Lunardi, C. Rossi Alvarez, C. Ur, T.

Martinez, M. Axiotis, D. Napoli, W. Urban, and T. Rząca-Urban, Eur. Phys. J. **A 18**, 577, (2003).

[Voi83] M. J. A. de Voigt, J. Dudek, and Z. Szymanski, Rev. Mod. Phys. **55**, 949, (1983).

[Wal79] P. M. Walker, S. R. Faber, W. H. Bentley, R. M. Ronningen, and R. B. Firestone, Phys. Lett. **87B**, 339 (1979).

[Wal80] P. M. Walker, S. R. Faber, W. H. Bentley, R. M. Ronningen, and R. B. Firestone, Nucl. Phys. **A343**, 45 (1980).

[Wal83] P. M. Walker, Phys. Scripta **T5**, 29 (1983).

[War95] S. J. Warburton, R. Chapman, J. Copnell, F. Lidén, A. G. Smith, J. P. Sweeney, D. M. Thompson, S. J. Freeman, G. B. Hagemann, and M. Piiparinen, Nucl. Phys. **A591**, 323 (1995).

[Wds54] R. D. Woods and D. S. Saxon, Phys. Rev. **95**, 577 (1954).

[Wen96] Shu-Xian Wen, H. Zheng, Sheng-Gang Li, Guang-Sheng Li, Guan-Jun Yuan, Peng-Fei Hua, Pei-Kun Weng, Lan-Kuan Zhang, Pan-Shui Yu, Chun-Xiang Yang, Hui-Bin Sun, Ya-Bo Liu, Yun-Zuo Liu, Yang Sun, and Da Hsuan Feng, Phys. Rev. C **54**, 1015 (1996).

[WMa05] W. C. Ma, in preparation.

[Wys88] R. Wyss, J. Nyberg, A. Johnson, R. Bengtsson, and W. Nazarewicz, Phys. Lett. **215B**, 2 (1988).

[w3AG] http://www.e12.physik.tu-muenchen.de/AGATA/

[w3GR] http://greta.lbl.gov/

[w3GS] http://www.phy.anl.gov/gammasphere/index.html

[w3SR] http://www.srim.org

[Zie85] J. F. Ziegler, J. P. Biersack, and U. Littmark, *The Stopping and Range of Ions in Solids*, Pergamon, New York, 1985.

Vita

Martin K. Djongolov was born on February 17, 1976, Sofia, Bulgaria. He graduated with honors from the Sofia Mathematical High School "Paisii Hilendarski" in the spring of 1994. He attended the Sofia University "St. Kliment Ohridski" and graduated with masters degree in nuclear and particle physics in the fall of 1999. His interest in physics sciences persisted and he joined the University of Tennessee, Knoxville, and accepted a research assistantship to study experimental high-spin nuclear physics under the supervision of Prof. Lee Riedinger. At the completion of this dissertation, Martin K. Djongolov considers to continue his activity in the research and academia field.